Order Number 9106925

Modeling the effects of refrigerant charging on air conditioner performance characteristics for three expansion devices

Farzad, Mohsen, Ph.D.

Texas A&M University, 1990

U·M·I
300 N. Zeeb Rd.
Ann Arbor, MI 48106

MODELING THE EFFECTS OF REFRIGERANT CHARGING ON AIR CONDITIONER PERFORMANCE CHARACTERISTICS FOR THREE EXPANSION DEVICES

A Dissertation

by

MOHSEN FARZAD

Submitted to the Office of the Graduate Studies of
Texas A&M University
in partial fulfillment of the requirement for the degree of

DOCTOR OF PHILOSOPHY

August 1990

Major Subject: Mechanical Engineering

MODELING THE EFFECTS OF REFRIGERANT CHARGING ON AIR CONDITIONER PERFORMANCE CHARACTERISTICS FOR THREE EXPANSION DEVICES

A Dissertation

by

MOHSEN FARZAD

Approved as to Style and Content by:

D.L. O'Neal
(Chair of Committee)

W.D. Turner
(Member)

W.M. Heffington
(member)

L.O. Degelman
(Member)

W.L. Bradley
(Head of Department)

August 1990

ABSTRACT

Modeling the Effects of Refrigerant Charging on
Air Conditioner Performance Characteristics
For Three Expansion Devices. (August 1990)
Mohsen Farzad, B.S., Texas A&M University
M.S., Texas A&M University
Chair of Advisory Committee: Dr. D.L. O'Neal

An experimental and analytical study concerned with the off-design refrigerant charging of air conditioners is presented. A series of experiments were conducted to characterize the effects of refrigerant charge and type of expansion device on the system performance (capacity, EER, SEER, etc.) of an air conditioner. All experiments were performed according to the ASHRAE Standard [1983]. The effects of off-design refrigerant charge in the system, type of expansion device (capillary tube, TXV, and short-tube orifice), and outdoor dry-bulb temperature (82° to 100°F) on the wet and dry steady state and cyclic tests are addressed in this study. The fully charged condition was established as a base case for all the expansion device systems. A full charge was obtained by charging the unit to the superheat or subcooled condition specified by the manufacturer charging chart. Once the full charge was determined, refrigerant was then added in 5% increments from -20% of full charge to +20% of full charge to cover the full range of charging conditions for a particular expansion device being tested. The investigation of off-design charging indicated that the system performance variables (total capacity, EER, and SEER) of the unit with capillary tube were more sensitive to off-design charging than the systems with TXV and short-tube orifice. From -20% to

+20% charging, the capacity and EER showed a strong dependence on the outdoor temperature, but varied little with charge for the TXV and short-tube orifice expansion systems. A -20% charging resulted in a 21% reduction in SEER while a +20% charging produced a 11% reduction in SEER for the unit with capillary tube. For the TXV , SEER dropped 2% and 8% for -20% and +20% refrigerant charging, respectively. The SEER was constant at 9.4 for all the charging condition except for -5% charging where it peaked to 9.9 for the short-tube orifice expansion system. This trend would suggest that the range of sensitivity of an short-tube orifice system is confined within a small refrigerant charge.

A new heat exchanger model based on tube-by-tube simulation was developed and integrated into the ORNL heat pump model. The model was capable of simulating the steady state response of a vapor compression air-to-air heat pump and air conditioner commonly used in residential applications. The simulated results were compared with laboratory tests at two outdoor temperatures. It was found that the ORNL model estimates were within an average of 3% of the experimental results from - 10% to +10% charging conditions. The model predicted the system performance up to 8% higher than measured results at +/-20% and +/-15% charging conditions. Among the eight void fraction models studied, the Hughmark model showed the best agreement between superheat and subcooled temperatures, refrigerant flow rate and capacity and the measured results.

ACKNOWLEDGMENT

I wish to express my appreciation to Dr. Dennis O'Neal for his outstanding guidance and invaluable help during the course of this study.

I thank Dr. W.D. Turner and Dr. W.M. Heffington for their helpful suggestions. I also want to thank Dr. L.O. Degelman for serving on my committee and Dr. D.H. O'Brien for being my graduate council representative. I would like to acknowledge the partial financial support provided by the Energy System Laboratory Research Consortium.

I would like to thank Ray, Frank and Chris for their help at the Energy Systems Laboratory, in the Department of Mechanical Engineering. I also like to express my appreciation to Nancy for her support and patience throughout this study.

Finally, I would like to express my gratitude to my parents, brothers and sisters that in one way or another helped me throughout my academic life.

DEDICATION

To the Brother I Lost Forever

Mohammed R. Jahfarzadeh

TABLE OF CONTENTS

TABLE OF CONTENTS (Continued)

TABLE OF CONTENTS (Continued)

LIST OF TABLES

LIST OF FIGURES

LIST OF FIGURES (Continued)

LIST OF FIGURES (Continued)

LIST OF FIGURES (Continued)

LIST OF FIGURES (Continued)

LIST OF FIGURES (Continued)

LIST OF FIGURES (Continued)

NOMENCLATURE

A	area, ft^2
C_p	specific heat at constant pressure, Btu/lb-F
D	diameter,
f	friction factor
h	heat transfer coefficient, air enthalpy
i	enthalpy Btu/lbm
g	gravity acceleration
L	length of the tube
k	thermal conductivity, Btu/hr-F-ft
J	the mechanical equivalent of heat
m	mass flow rate, lbm/hr
Nu	Nusselt number
Pr	Prandtl number
R'	condensation rate per unit with of a fin
Re	Reynolds number
S	slip ratio
T	temperature, F or R
x	quality of refrigerant
U	overall tube heat transfer coefficient
v	specific volume, ft^3/lbm
We	Weber number

Greek Symbols

α	void fraction
ΔP	pressure drop
Δx	refrigerant vapor quality change
η	fin efficiency
ρ	refrigerant density, lbm/ft^3
δ	condensate thickness
μ	kinematic viscosity, ft^2/sec
Θ	two-phase correction factor
ω	humidity ratio

Subscripts

a	air
evp	evaporator
con	condenser
f	fluid, fin
fg	latent heat of evaporation
g	gas
i	inside, inlet
l	liquid
n	nozzle
r	refrigerant
o	outlet
ss	steady state
t	thickness
tp	two-phase
v	vapor
w	water

GLOSSARY OF TERMS

AMAC	Air Movement and Control Association
ARI	Air Conditioning and Refrigeration Institute
ASHRAE	American Society of Heating, Refrigerating and Air Conditioning Engineers
ASME	American Society of Mechanical Engineers
Btu	British thermal unit
C_D	Coefficient of Degradation
cfm	Cubic feet per minute
CLF	Cooling Load Factor
COP	Coefficient of performance
DB	Dry Bulb
DOE	Department of Energy
DP	Dew Point
EER	Energy Efficiency Ratio
EER_C	Dry Coil Energy Efficiency Ratio
EER_D	Dry Coil Cyclic Energy Efficiency Ratio
FC	Full Charge
fpm	Feet per minute
lbma	Pounds mass of dry air
NIST	National Institute of Standards and Technology
OC	Overcharge
OD	Outdoor Room Temperature
ORNL	Oak Ridge National Laboratory
SEER	Seasonal Energy Efficiency Ratio
TC	Thermocouple

TXV	Thermal Expansion Valve
UC	Undercharge
WB	Wet Bulb

CHAPTER I

INTRODUCTION

Central air conditioning is one of the major electrical energy consuming appliances in residences. One variable influencing the energy use of an air conditioner is the amount of refrigerant in the system. To obtain the best performance (capacity and efficiency) for an air conditioner over its lifetime, it must be charged with the optimum amount of refrigerant.

The most important component in the air conditioner from the standpoint of system control is the expansion device. The purpose of the expansion device is to regulate the flow of refrigerant to the evaporator. Three expansion devices are used commonly in refrigerating systems: (1) capillary tubes, (2) thermostatic expansion valves (TXV), and (3) fixed orifices. TXVs and orifices are being used increasingly in residential heat pumps and air conditioners. Each expansion device may regulate the flow of refrigerant differently under the conditions of improper or proper charging.

Central air conditioner ratings now include cycling tests as a mean of simulating actual on/off characteristics in the field. Thus, steady state measurements may not yield the same magnitude of degradation as seasonal performance measurements. The impact of off-design charging on Seasonal Energy Efficiency Ratio (*SEER*) would be more useful in evaluating actual effects on seasonal energy consumption.

An experimental and analytical investigation has been initiated to quantify the effects of refrigerant charge on the performance of an air conditioner for these different expansion devices. The primary performance variables to be considered include: capacity, power, refrigerant charge, and Energy Efficiency Ratio (*EER*). The effects of

---

The format of this dissertation conforms to that of the Transactions of the American Society of Heating, Refrigeration and Air Conditioning Engineers.

outdoor temperature on the steady state performance of an air conditioner is also addressed in this study.

This study includes a review of the relevant literature, discussion of the experimental test results, model development and analysis. Chapter II summarizes the literature reviewed for the research. The review was done to determine the current state of knowledge of off-design charging performance and to justify the need for additional research. Since it is not practical to examine a large number of air conditioners for off-design charge conditions, a simulation model is needed to predict the off-design performance. The Oak Ridge National Laboratory (ORNL) Heat Pump model was modified and used to predict the off-design performance. The modifications made to the model are described in Chapter III. Chapter IV provides details of the experimental test facility and procedure. The experimental procedure was developed by ARI, DOE, and ASHRAE for studying the air conditioner steady state and cyclic performances. Chapter V discusses the base case steady-state and cyclic tests for fully charged conditions. The experimental test results are discussed in Chapter VI for off-design tests. Chapter VII compares the system performance for different void fraction models and the simulated results with the experimental results. Conclusions and recommendations for the future research are provided in Chapter VIII.

CHAPTER II

LITERATURE REVIEW

To obtain the best performance (capacity and efficiency) for an air conditioner over its lifetime, it must be charged with the optimum amount of refrigerant. A recent study [Neal and Conlin, 1988] concluded that many residential air conditioners are not charged according to manufacturers guidelines. The Trane Company found that a ten percent drop in refrigerant charge caused an efficiency drop of twenty percent on an eight year old residential air conditioner [Trane, 1976]. A few researchers have reported the effect of the off-design charging conditions on the performance of an air conditioner[Trane Co., 1976; Domingorena, 1980; Houcek and Thedford, 1984].

The available relevant literature was divided into three categories: (1) Laboratory Measurement; (2) Influence of Expansion Device; (3) Modeling of Charge Inventory; (4) Heat Exchanger Models (ORNL and NIST). Each is discussed below.

LABORATORY MEASUREMENTS OF CHARGING ON SYSTEM PERFORMANCE

Houcek and Thedford [1984] conducted a limited laboratory steady state test of a 1.5 ton split system. Three charging conditions were evaluated: 23% below (by mass), nominal (according to the manufacturer recommendation), and 23% above nominal chargings. Their data indicated a reduction in capacity of 23% and 38% at 82°F and 95°F, respectively for a change 23% below nominal charging. The steady state Energy Efficiency Ratio (EER) was reduced by 34% at 95°F for the same charge (Figure 2.1).

While Houcek and Thedford's data may provide some qualitative trends for off-design charging, it had several important shortcomings. First, the study was not conducted in psychrometric facilities where temperature and humidity variations could be precisely controlled. Second, all the tests were steady state. Central air conditioner

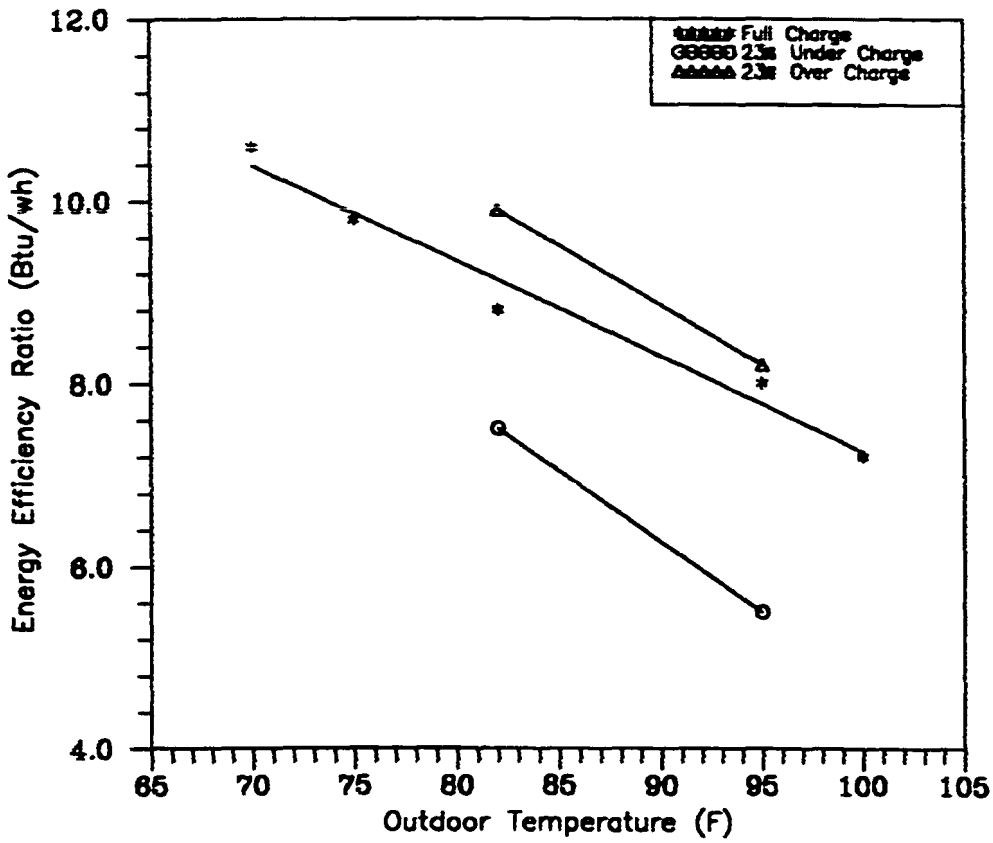

Figure 2.1 - The Effects of Off-Design Refrigerant Charging on the Energy Efficiency Ratio
(Source: Houcek and Thedford, [1984])

ratings now include cycling tests as a means of simulating actual on/off characteristics in the field. Thus, steady state measurements may not yield the same magnitude of degradation as seasonal performance measurements. Third, their tests were limited to extreme off-design charging conditions.

Other measurements by Domingorena [1980] have demonstrated that reducing the charge by 20% and 47% below that recommended by the manufacturer can produce a 28% and 67% reduction in heating capacity and 18% and 32% in COP for air-to-air heat pumps, respectively.

INFLUENCE OF THE EXPANSION DEVICE ON COP

A study by Stoecker [1981] compared the performance of an air conditioner with capillary tube and a TXV when the systems were charged according to manufacturer's guidlines. In this study, the Building Loads Analysis and System Thermodynamics (BLAST) was used simulating two identical residences. The results showed that the seasonal COP of the system with the TXV was 2% higher than of the capillary tube system.

Stoecker set the refrigerant charge for the systems to provide the most efficient design performance. The study did not address the effect of off-design charging on the system performance with different expansion devices.

MODELING OF CHARGE INVENTORY

It would be beneficial to be able to predict the refrigerant charge that would produce optimum system performance. Estimating the refrigerant charge requires knowledge of the state (quality, temperature, pressure, etc.) of the refrigerant and geometric variables (tube length, diameter, etc.) throughout the system. During normal operation, much of the refrigerant in the system is located in the evaporator and condenser. Estimating the amount of refrigerant in these heat exchangers requires

knowledge of the two-phase behavior of the refrigerant. The variation of refrigerant quality in the condenser and evaporator is a function of geometric variables, refrigerant conditions entering the heat exchangers, and the air-side heat transfer. Many investigators have attempted to develop models of the two-phase behavior in condensers and evaporators. The prediction of the refrigerant charge inventory in the two-phase region was studied by a number of researchers [Lockhart and Martinelli, 1949; Stoecker et. al, 1981; Daniels and Davies, 1975; Dhar and Soedel, 1979; and Rice, 1987]. To estimate the refrigerant charge in heat exchangers, the void fraction is needed. It is the ratio of tube cross-sectional area occupied by vapor to total cross-sectional area occupied by vapor and liquid. Rice studied 10 void fraction correlations and four heat flux assumptions. The void fraction was represented as a function of quality, x, slip ratio, S (the ratio of vapor velocity to liquid velocity in the refrigerant tubes), and refrigerant properties. The void fraction was divided into four categories: (i) Homogeneous, (ii) Slip-Ratio-Correlated, (iii) X_{tt}-Correlated, and (iv) Mass-Flux-Dependent [Rice 1987].

Homogeneous Model

The homogeneous model considered the two phases to flow as a homogeneous phase possessing mean fluid properties and traveling at the same velocity (S=1). In this model, the relationship between void fraction, α, and mass quality, x, was simply derived as:

$$\alpha = \frac{1}{S \ \frac{(1-x)}{x} \ [\rho_g / \rho_f]} \tag{2.1}$$

Equation (2.1) was used by Daniels [1975], Dhar [1979], and Stoecker [1981].

Slip-Ratio-Correlated

The liquid and vapor phases were assumed to have separated streams which both

flow with different velocities. It was further assumed that thermodynamic equilibrium exists at all points in the flow. Several investigators estimated the slip ratio, S, in Equation (2.1) differently.

Zivi [1964] developed a void fraction similar to Equation (2.1) where the slip ratio was defined as function of density ratio of the refrigerant liquid to vapor.

$$S = [\, \rho_g / \rho_f \,]^{-1/3} \tag{2.2}$$

The void fraction developed by Zivi was for the annular flow and under conditions of zero wall friction.

Thom [1964], like Martinelli used steam/water systems under boiling conditions. He found that the slip ratio, S, was dependent on the refrigerant pressure only and was independent of quality. The Thom method represented the slip ratio in terms of viscosity and density ratios and was given by:

$$S = [\, \rho_g / \rho_f \,]\, [\, \mu_f / \mu_g \,]^{0.2} \tag{2.3}$$

X_{tt}-Correlated

A more involved approach was introduced to avoid a form of the homogeneous equation (i.e., Eq. 2.1). Lockhart-Martinelli [1949] presented the void fraction data as a function of X_{tt}:

$$X_{tt} = [(1 - x) / x \,]^{0.9} [\, \rho_g / \rho_f]^{0.5} [\, \mu_f / \mu_g \,]^{0.1} \tag{2.4}$$

Wallis [1969] approximated the Lockhart-Martinelli void fraction data in the following form:

$$\alpha = (1 + X_{tt})^{-0.378} \qquad \text{for } X_{tt} < 10 \qquad (2.5)$$

Barcozy [1965] used X_{tt} correlation with a strong dependence on the viscosity and density ratios beyond that already included in Equation (2.4). He noted that there was also an apparent mass flux effect that was not accounted for in his correlation.

Mass-Flux-Dependent

This method included one physically based model for annular flow and two empirically based correlations. Several researchers correlated the void fraction a direct functional dependence on the physical property ratios and dimensionless parameters.

The void fraction model developed by Tandon [1985] included the effect of wall friction. His model was an improvement for annular flow over the Zivi method. The correlation was of the form

$$\alpha = f(\mathrm{Re}_L, X_{tt})$$

where Re_L is the liquid Reynolds number.

The model developed by Premoli [1971] was the modified homogeneous model (Eq. 2.1) where the slip ratio, S, is represented by

$$S = f(x, \mathrm{Re}_L, We, \rho_g/\rho_f)$$

where We is the Weber number defined as the ratio of inertia to surface tension forces.

Hughmark developed the void fraction model for vertical upward flow with air-liquid systems at atmospheric pressure. He assumed a bubble flow regime with a radial

gradient of bubbles across the channel. In his correlation, the void fraction was given by a correction factor K_H to the homogeneous model (Eq. 2.1).

$$\alpha = \frac{K_H}{\frac{(1-x)}{x}\left[\rho_g / \rho_f\right]} \tag{2.6}$$

where K_H is function of Reynolds number, Froude number, viscosity, density, and refrigerant mass flux.

Rice found that the choice of the void fraction model had a major effect on the estimated refrigerant inventory. He showed that the more involved models (i.e. Slip-Ratio-Correlated and Mass-Flux-Dependent) generally predict a larger liquid fraction presence in a two-phase mixture than the homogeneous model. Rice concluded that the more involved models generally predict a larger amount of refrigerant than the simple models for a specified condition.

Rice incorporated the void fraction models in the Oak Ridge National Laboratory (ORNL) heat pump system simulation model. This model was developed to predict the steady state performance of conventional, vapor compression, electrically driven, air-to-air heat pumps in both the heating and cooling modes. Although designed specifically to model heat pumps, it has also been adopted for use in room and central air conditioners [Fisher and Rice, 1983; Boecker and O'Neal, 1986; Penson, 1988].

Eight choices of void fraction models ranging from simple to more complex models were incorporated in the ORNL model. These models were categorized into mass-flow independent and mass-flow dependent methods by Rice [1987]. The mass-flow independent method (Homogeneous, Slip-Ratio-Correlated, and X_{tt}-Correlated) consisted of the Homogeneous, Zivi, Lockhart-Martinelli, Thom, and Baroczy models.

The mass-flow dependent method consisted of the Hughmark, Premoli, and Tandon models. Rice provided no data suggesting which charge inventory model provides the best estimate of charge in a system.

To test the variability in refrigerant charge estimated by the void fraction models, a 1.5 ton heat pump was simulated using the eight void fraction models. The design superheat and subcooling temperatures for the unit was set at 18.5°F and 11°F, respectively. The refrigerant charge (lbm), refrigerant flow rate, and COP of the system were calculated using the ORNL heat pump design model for each void fraction model. The models show a wide range in predicted refrigerant charge from 5.1 to 7.8 lbs. However, there was no variation in predicted COP and refrigerant flow rate. The ORNL model calculated the system performance based on the specified refrigerant superheat temperature not the refrigerant charge in the system.

Literature comparisons with experimental data for steady state design charge were done by Domanski and Didion [1983] and Thom and Tandon [1986]. Domanski and Didion used the Lockhart-Martinelli model to compare total charge and condenser charge with experimental results for one cooling mode condition. The model underestimated the charge in the system and the condenser by 26.5% and 15%, respectively. However, for estimating steady state performance under different refrigerant charges, different outdoor operating conditions, and various types of expansion devices, there are not sufficient data and independent comparisons to confidently recommend any one method.

ORNL AND NIST HEAT PUMP MODELS

The ORNL model is a detailed refrigeration cycle model based on underlying physical principles and generalized correlations. It evolved from models written at the Massachusetts Institute of Technology [Hiller and Glicksman, 1976] with the addition of selected routines by Kartsounes and Erth [1971], Flower [1978], Kusuda [1976], and

McQuiston [1978]. The model currently features a choice of charge inventory models.

The ORNL model provides two choices of compressor models. One model uses a manufacturer's compressor map to estimate refrigerant flow rates and power consumption as functions of condensing and evaporating temperatures. The other ORNL compressor model does an energy balance on the compressor, and requires the motor efficiency, mechanical efficiency, and isentropic compression efficiency, etc., as input.

The ORNL model is capable of modeling plate-fin evaporator and condenser heat exchangers. The calculational methods which have been used assume that the heat exchangers consist of equivalent, parallel refrigerant circuits with unmixed flow on both the air and refrigerant sides. The coil performance calculations in the model are based on the effectiveness-NTU method for a cross-flow heat exchanger with both fluids unmixed.

The model provides four methods of modeling the expansion device in the unit. The user can specify a thermal expansion valve (TXV), a capillary tube, a fixed orifice, or fixed condenser subcooling.

The National Institute of Standards and Technology (NIST) heat pump model also simulates the performance of a heat pump in both the cooling and heating modes. The major differences between the ORNL and NIST model are the compressor and heat exchangers designs. The NIST compressor model requires a cumbersome input and is a function of the energy balance on the compressor, motor efficiency, mechanical efficiency, and isentropic compression efficiency. These values are not usually measured during the compressor efficiency test. For the ORNL compressor model, the map based model which is a function of refrigerant flow rate and power consumption would be more accurate in generating operating conditions.

The NIST heat exchanger models are more realistic and accurate than those in the

ORNL model. A heat exchanger consists of a set of finned tubes connected in a specifically designed circuit in a "branch" configuration (Figure 2.2). The NIST model models the "branch" circuitry in heat exchangers. The model simulates each tube and determines the amount of refrigerant in each tube of a branch. The ORNL model requires the user to guess at the number of parallel circuits that are equivalent to the branch circuits. For example, the ORNL model treats the heat exchanger shown in Figure 2.2 as three to ten identical equivalent parallel refrigerant circuits (Figure 2.3). Because the refrigerant charge in the system is determined by accurately characterizing the two-phase regimes in the heat exchangers, the NIST model should give a more realistic estimate of the amount of refrigerant in the tubing.

Another difference between the two models is the charge inventory in the system. The charge inventory models in the ORNL model allow users to specify or determine the refrigerant charge in a system. For a two-phase refrigerant flow in the condenser and evaporator models, the refrigerant heat transfer coefficient and pressure drop were calculated depending upon the void fraction model. Eight choices of void fraction models ranging from simple to more complex models are available in the ORNL model to simulate the system performance and the refrigerant charge inventory. The void fraction in the NIST model is based only on the Lockhart-Martinelli model.

SUMMARY OF LITERATURE REVIEW

Central air conditioner ratings now include cycling tests as a mean of simulating actual on/off characteristics in the field. Thus, steady state measurements may not yield the same magnitude of degradation as seasonal performance measurements. The references cited above do not determine the system seasonal performance. The studies reviewed above were limited to steady state measurements. The impact of off-design charging on *SEER* would be more useful in evaluating actual effects on seasonal energy consumption.

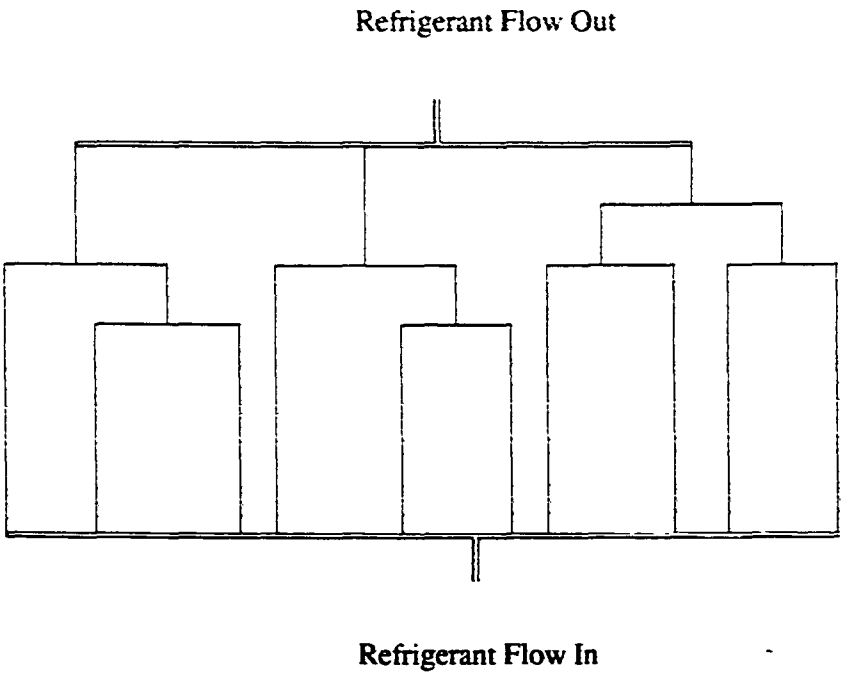

Figure 2.2 - Illustration of Refrigerant Circuitry in a Heat Exchanger

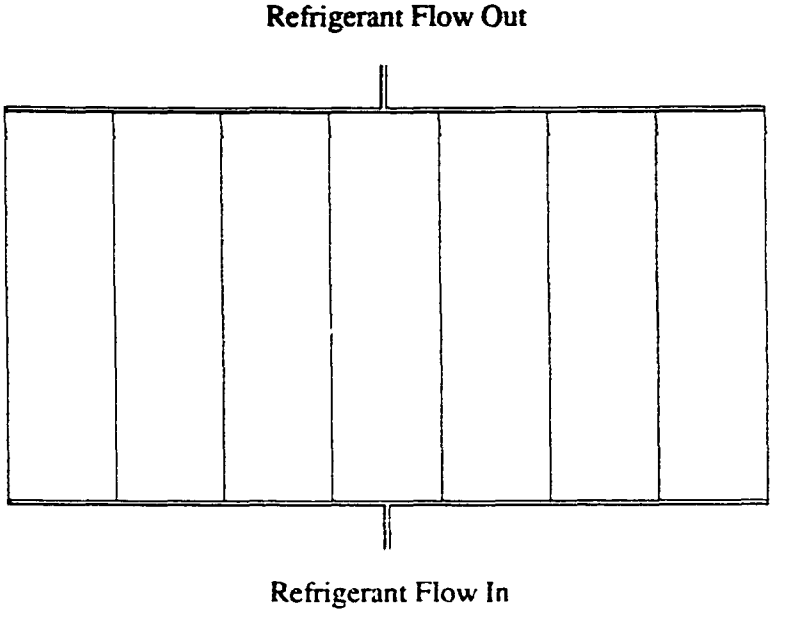

Figure 2.3 - Equivalent Parallel Refrigerant Circuits in the ORNL Model

These studies indicated that optimum charging (manufacturer's recommendation) was detrimental to air conditioner performance. Although a number of researchers have reported the importance of charging in the system, most have results for only a small number of charges in the system. No study provided enough data for developing quantitative guidelines on relating refrigerant charging to the performance of the system.

The effect of different expansion devices and ambient temperature on the performance of an air conditioner have not been explored experimentally for different charging conditions. Major experimental issues that need further investigation are:

(i) The effects of off-design charging on an air conditioner performance (*SEER*).

(ii) The effects of different expansion devices on *SEER* for the off-design charged unit.

The heat exchanger model in the ORNL model simulates only certain regular tube configuration and is insensitive to different coil circuitry patters. The refrigerant heat transfer coefficient and pressure drop calculated in the heat exchanger depend upon the void fraction model. From the eight void fraction models available in the ORNL, there are not sufficient data and independent comparisons to confidently recommend any one method. Major issues that need further investigation are:

(i) Determining the most accurate charge inventory model in the system.

(ii) Improving the heat exchanger model in the ORNL heat pump model.

CHAPTER III

MODEL DEVELOPMENT

The literature reviewed in Chapter II showed that there were two heat pump system simulation models (ORNL and NIST). These models were developed to predict the steady state performance of conventional, vapor compression, electrically driven, air-to-air heat pumps in both the heating and cooling modes. A major difference between the NIST and ORNL models are the heat exchanger models. In the ORNL model, a simplified heat exchanger model based on "equivalent" parallel refrigerant circuits was used. This approach simplified the computational complexity of the system. The NIST model simulates the heat exchangers more realistically and accurately than those in the ORNL model. The NIST model models the "branch" circuitry in heat exchangers. The model simulates each tube and determines the amount of refrigerant in each tube of a branch.

To improve the predictive capability of the ORNL model, the heat exchanger modeling based on tube-by-tube simulation which was used in the NIST model was integrated into ORNL model. The details of new heat exchanger model are discussed below as well as a description of the complete program.

THE MODEL CALCULATIONAL PROCEDURE

The heat pump model is organized into two major high and low pressure sections. The high-pressure section combines the compressor, condenser, and expansion device. The low-pressure section contains the evaporator model. The program uses enthalpy and pressure balances for simulating the performance of a heat pump with a TXV. The enthalpy balance implies that the energy input to the system must be equal to energy rejected by the system. The pressure balance states that the increase of refrigerant pressure during the compression process by a compressor must be equal to the total

pressure drop in the system. The refrigerant mass inventory balance is required if a capillary tube or an short-tube orifice expansion device is used and refrigerant mass inventory is requested. The mass inventory balance implies that amount of refrigerant in the system is the same at all times for any operating conditions. Calculations proceed iteratively between the high and low sections until the desired overall balance is obtained. Initially, the simulation starts in the high-pressure section. The user is required to specify:

* The level of superheat or refrigerant charge,
* The design parameters for an expansion device or the level of subcooling,
* Indoor and outdoor conditions,
* Heat exchanger void fraction model for refrigerant charge inventory,
* Power and refrigerant mass flow rate maps for compressor model, and
* Geometry dimensions of system components.

The user must also provide estimates for:

* The condenser refrigerant saturation temperature, and
* The evaporator refrigerant saturation temperature.

The simulation process starts with the specified superheat and the evaporator and condenser refrigerant saturation temperatures. The specified superheat remains fixed for the initial iteration of high-pressure and low-pressure calculations. Using these data along with the compressor map-based refrigerant flow rate, compressor performance is simulated yielding refrigerant mass flow rate and the condenser inlet conditions. Next, the condenser and the expansion device are simulated. A refrigerant mass flow balance is sought by comparing refrigerant mass flow rate through the compressor and the expansion device. If compared mass flows are not within a fixed tolerance, the simulation of the high-pressure section is repeated for a new condenser saturation temperature. For a specified subcooling, the condenser outlet refrigerant state is

computed and compared to the specified value. If not agreed within a fixed tolerance, then the condenser saturation is changed and the compressor and condenser calculations are repeated. Once the desired condenser subcooling is achieved, the equivalent expansion device parameters would be determined for the specified subcooling.

Once refrigerant mass flow balance is reached, simulation of the evaporator is performed based on the known refrigerant mass flow, refrigerant conditions at the evaporator inlet and outlet. The evaporator model is repeatedly called. The inlet air temperature is varied and the superheat and a pressure drop across the heat exchanger calculated. The evaporator model is repeated until the calculated superheat agrees with the specified one. Thus, the enthalpy and pressure balances are established.

In case of specified refrigerant charge in the system, the amount of refrigerant in the system is calculated and compared to the actual refrigerant mass input. If the amount of refrigerant calculated is smaller than actual refrigerant, the superheat guess must be decreased and the high and low pressure calculations repeated. The sequence of calculations is presented graphically in Figure 3.1.

Two compressor models are available in the ORNL heat pump model. The first compressor model is based on the use of compressor manufacturer's data (compressor maps). The second model, a loss and efficiency-based compressor model, is intended to predict how changes in compressor loss and efficiency terms affect system performance.

The map-based compressor model uses the compressor performance data provided by the manufacturers. Performance curves are generated for motor power input, refrigerant mass flow rate, and refrigerant capacity as functions of condenser and evaporator saturation temperatures. The refrigerant mass flow rate and motor power input curves were fitted in two bi-quadratic equations as functions of condenser and evaporator saturation temperatures. A form of a bi-quadratic equation is shown below:

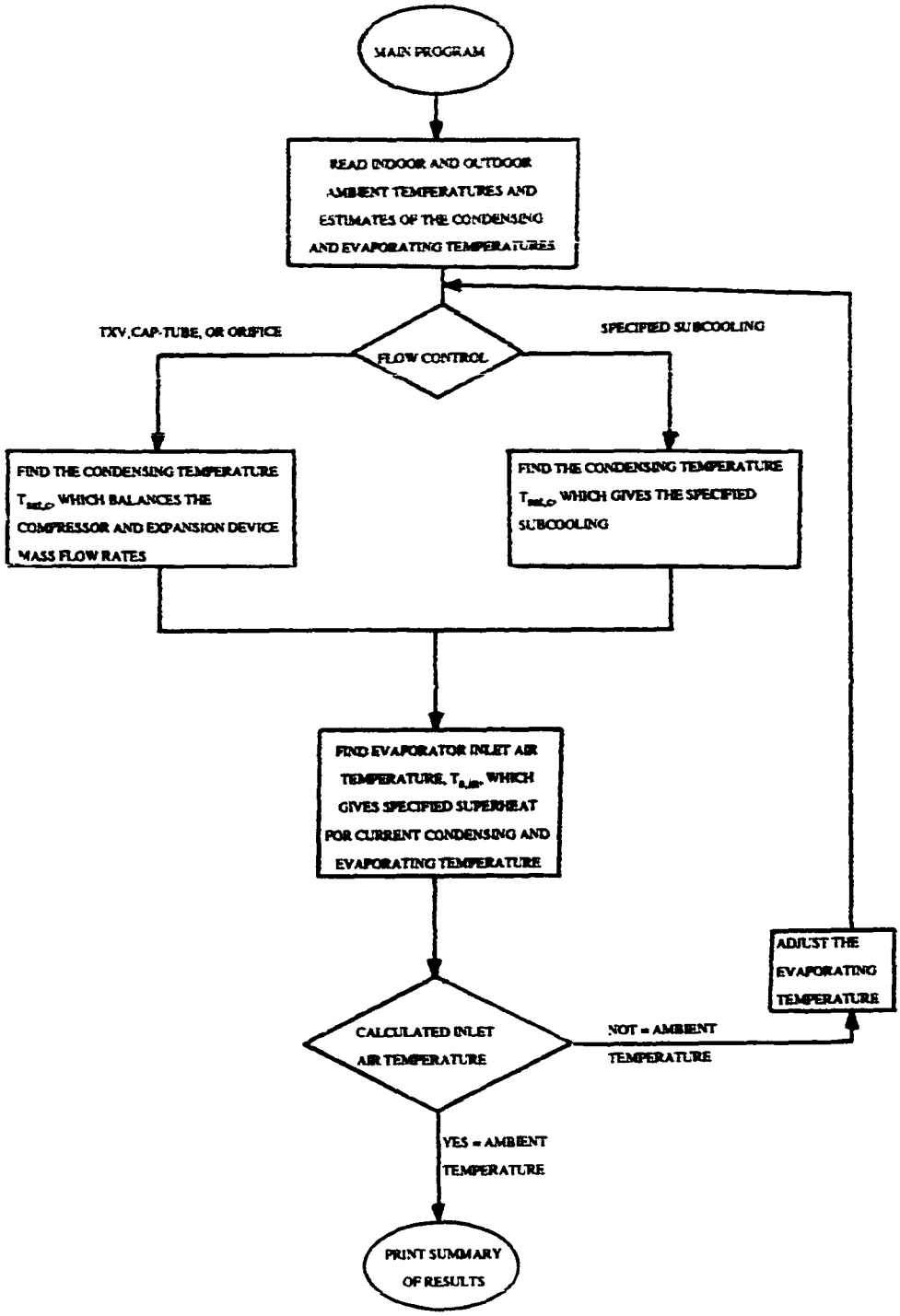

Figure 3.1 - Block Diagram of Iterating Loops for the ORNL Model

$$f(T_{con}, T_{evp}) = C_1T^2_{con} + C_2T_{con} + C_3T^2_{evp} + C_4T_{evp} + C_5T_{con}T_{evp} + C_6 \qquad (3.1)$$

The compressor maps and the bi-quadratic fits are generated only for one superheat specified by manufacturers. For a different superheat, the refrigerant mass flow rate and the power input must be corrected. To account for this effect, a linear correction as a function of refrigerant density was presented by Dabiri and Rice [1981].

The second model includes an energy balance on the compressor, and requires the motor efficiency, mechanical efficiency, and isentropic compression efficiency as input. This model does not predict compressor performance as accurately over the same range of operating conditions as the map-based model. However, it is well suited for studying internal compressor improvements and interactions and their effects on system performance [ORNL, 1981].

The ORNL heat pump model provides four methods of modeling the expansion device in the system. The program contains subroutines with correlations for a thermal expansion valve (TXV), capillary tube, fixed short-tube orifice, and fixed condenser subcooling.

HEAT EXCHANGER MODEL DEVELOPMENT

The heat exchanger model in the ORNL heat pump simulation program calculates the coil performance based on the effectiveness-NTU method for a cross-flow heat exchanger with both fluids unmixed. The ORNL model simulates only certain regular tube configuration and is insensitive to different coil circuitry patterns. For a typical heat exchanger shown in Figure 3.2., the ORNL heat exchanger model treats the coil as four identical equivalent parallel refrigerant circuits and simulates only one circuit. The coil performance is then calculated by the number of coil circuits multiplied by the simulated

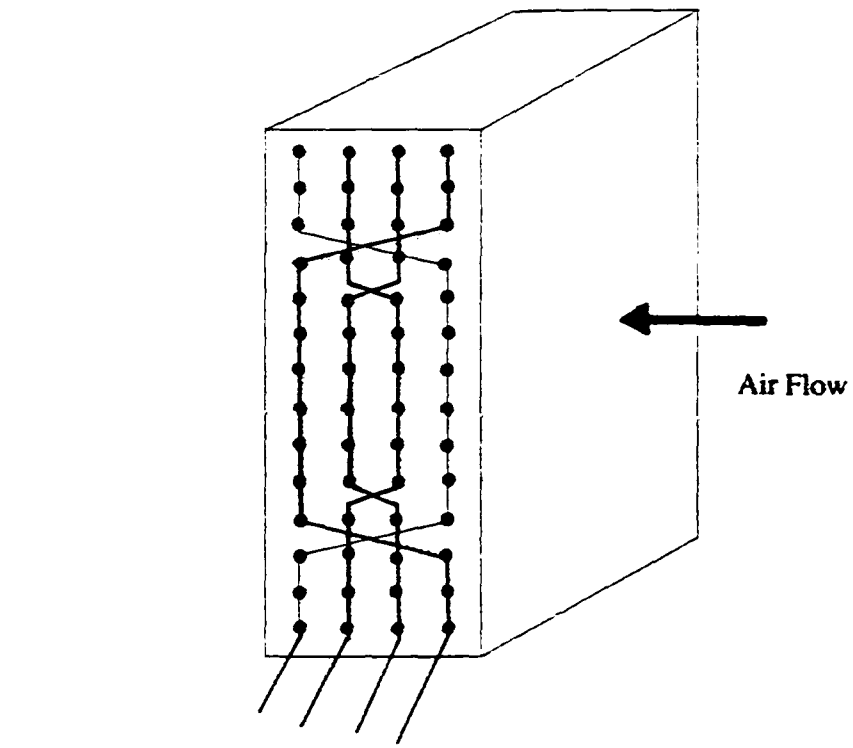

Figure 3.2 - A Typical Heat Exchanger Circuitry

circuit. The new heat exchanger model simulates the coil based on tube-by-tube simulation regardless of circuitry pattern. Although the tube-by-tube simulation approach increases the computational complexity of the system, it is more realistic and should be more accurate. Therefore, it was decided that a heat exchanger model with capabilities that could handle all types of configuration was necessary to get a more realistic and accurate coil performance.

Because there are many similarities between the condenser and evaporator, a similar heat exchanger methodology was used for both. The principal difference between the condenser and evaporator models is the dehumidification algorithm. The differences are pointed out where they occur.

It is assumed that the fin area served by each tube is equivalent in performance to a circular-plate fin of equal area [Carrier and Anderson 1944]. Thus a single tube is considered with a circular fin of diameter, D_f, as shown in Figure 3.3. D_f is calculated as a function of spacing of refrigerant tubes perpendicular to the direction of air flow, d_2, and in the direction of air flow, d_1, respectively.

Refrigeration Side Heat Transfer Rate Calculation

To simulate the heat exchanger, a separate tube is considered in a pure cross-flow arrangement. The refrigerant side heat transfer calculations are separated into superheated, two-phase and subcooled regions. The heat transfer rate for each mentioned flow condition can be calculated (as reported in NIST [1983]) as follows:

* single-phase flow only - superheated or subcooled refrigerant at inlet and outlet

$$Q = C_{Pr}\, m_r (T_{r,i} - T_{a,i})(1 - \exp[(\ \frac{-C_{Pa}\, m_a}{C_{Pr}\, m_r}\ )(1 - \exp(\ \frac{-U\, A_o}{C_{Pa}\, m_a}\ ))]) \qquad (3.2)$$

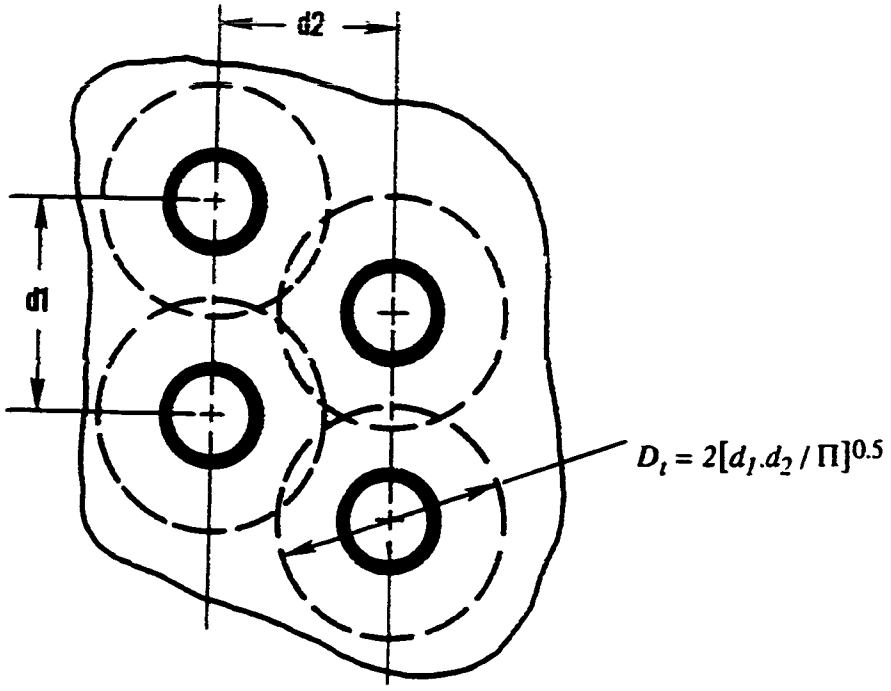

Figure 3.3 - Approximation Method for Treating a Rectangular-Plate Fin in Terms of a Flat Circular-Plate Fin of Equal Area

* two-phase flow only - refrigerant is in two-phase at both inlet and outlet

$$Q = C_{pa}\, m_a\, (1\text{-}exp(\ \frac{-U\, A_a}{C_{pa}\, m_a}\ ))\, (T_{r,g} - T_{a,i}) \tag{3.3}$$

* superheated at tube inlet and two-phase at the tube outlet

$$Q = m_r(I_{r,i}\text{-}I_{r,v})+C_{Pa}\, m_a(1\text{-}Z_v)(1\text{-}exp(\ \frac{-U\, A_o}{C_{Pa}\, m_a}\ ))(T_{r,g}\text{-}T_{a,i}) \tag{3.4}$$

Z_v is the fraction of the tube length in the superheated region. It can be calculated by the following equations:

$$Z_v = \frac{-C_{Pr}\, m_r\, Ln\,(1 - \frac{(I_{r,i} - I_{r,g})}{C_{Pr}(T_{r,i} - T_{a,i})})}{C_{Pa}\, m_a(1 - exp\,(1 - \frac{U\, A_o}{C_{Pa}\, m_a}))} \tag{3.5}$$

* two-phase at tube inlet and subcooled at the tube outlet

$$Q = C_{Pr}\, m_r(T_{r,g} - T_{a,i})(1 - exp(\ \frac{-C_{Pa}\, m_a(1\text{-}Z_{tp})}{(C_{Pr}\, m_r)}\ ))\,(1 - exp(\frac{-U\, A_o}{C_{Pa}\, m_a}\ ))$$
$$+\ m_r(I_{r,i} - I_{r,l}) \tag{3.6}$$

Z_{tp} is fraction of the tube length in the two-phase region. It can be calculated by the following equation:

$$Z_{tp} = \frac{m_r(I_{r,i} - I_{r,l})}{C_{Pa}\, m_a(1 - exp(\ \frac{-U\, A_o}{C_{Pa}\, m_a}\ ))(T_{r,i} - T_{a,i})} \tag{3.7}$$

Single-Phase Forced Convection

The refrigerant side heat transfer coefficient for the superheated region in the condenser inlet and evaporator outlet is a function of the Nusselt, Reynolds and Prandtl numbers. The heat transfer coefficient was determined from the Dittus-Boelter equation in the following form [Incropera and De Witt, 1981]:

$$Nu = 0.023\, Re^{0.8}\, Pr^{0.333} \tag{3.8}$$

where $Nu = \dfrac{h_r D_i}{k}$, $Pr = \dfrac{C_P \mu}{k}$, and $Re = \dfrac{G D_i}{\mu}$

Two-Phase Forced Convection with Condensation

The predominant flow pattern during condensation is annular flow with liquid refrigerant flowing on the pipe wall and vapor refrigerant flowing in the core [NIST, 1983]. A correlation proposed by Travis, Baron and Rohsennow [1971] based on the analytical and experimental studies of vapor condensation in annular flow with refrigerants R-12 and R-22 has the following form:

$$Nu = \frac{Re_L^{0.9}\, Pr_L\, F_1^{\beta}}{F_2} \tag{3.9}$$

where $Nu = \dfrac{h_r D_i}{k_L}$, $Re_L = \dfrac{m(1-x)D_i}{\mu_L}$, and $Pr_L = \dfrac{\mu_L C_{PL}}{k_L}$

F_1 and F_2 in Eq. (3.9) are dimensionless parameters expressed as follows:

$$F_1 = 0.15\,(X_{tt}^{-1} + 2.85 X_{tt}^{0.524}) \qquad \text{for } F1<1\ \ \beta=1,\ F1>1\ \ \beta=1.15 \tag{3.10}$$

$$F_2 = 0.707\, Pr_L\, Re_L^{0.5} \qquad \text{for } Re_L < 50$$

$$F_2 = 5\, Pr_L + 5\, Ln(1 + Pr_L(0.09636\, Re_L^{0.585} - 1)) \qquad \text{for } 50 < Re_L < 1125$$

$$F_2 = 5\, Pr_L + 5\, Ln(1 + Pr_L) + 2.5\, Ln(0.00313\, Re_L^{0.812}) \qquad \text{for } Re_L > 1125$$

The parameter, X_{tt}, was formulated by Lockhart-Martinelli with the assumption of no radial pressure gradient and for a smooth pipe. X_{tt} is function of refrigerant quality, specific volume, and viscosity and has the following form:

$$X_{tt} = \left(\frac{(1-x)}{x}\right)^{0.9} \left(\frac{v_L}{v_V}\right)^{0.5} \left(\frac{\mu_L}{\mu_V}\right)^{0.1} \tag{3.11}$$

Equation 3.9 is applicable only for annular condensation flow and qualities ranging from 0.1 to 0.9. It is assumed that for flow with qualities less than 0.1 and higher than 0.9, the heat transfer coefficient changes linearly from a two-phase to a single-phase flow. Thus, the heat transfer coefficient is calculated using linear interpolation between values obtained from Equations 3.9 and 3.8.

Two-Phase Forced Convection with Evaporation

The refrigerant enters the evaporator in two phase with a low quality. The quality of the refrigerant increases as the refrigerant travels through the evaporator. A correlation proposed by Pierr [1957] based on his experimental work with refrigerants R-12 and R-22 is used in the model. The correlation has the following form:

$$Nu = \frac{h_r D_i}{k_L} = 0.0009 \frac{m D_i}{\mu_L} \left[\frac{J \Delta x I_{fg}}{L}\right]^{0.5} \qquad \text{for } 28.5 < Nu < 753 \tag{3.12}$$

The correlation is applicable for a refrigerant with quality ranging from 0.15 to 0.9. For a refrigerant greater than 0.9, the heat transfer coefficient changes linearly from a two-phase to a single-phase flow. Thus, the heat transfer coefficient is calculated using linear interpolation between values obtained from Equations 3.12 and 3.8.

Air Side Heat Transfer Rate Calculation

The overall air-side heat transfer coefficient is divided into two sections: (i) dry and (ii) wet coil analysis. The difference between the wet and dry coil analysis is moisture being removed from an air stream in the case of a wet coil. The addition of fins to the tubes greatly increases the outer heat transfer area which affects the air side heat transfer rate. The geometry parameters affecting the heat transfer are illustrated in Figure 3.4.

Overall Heat Transfer Coefficient of a Dry Finned Tube

The air-side heat transfer coefficient was determined by the correlation proposed by Briggs and Yong [1962]. They conducted a regression analysis of the test data as a function of Reynolds number, Prandtl number, and dimensionless fin geometry parameters which yielded the following equation:

$$Nu = \frac{h_{co} D_o}{k_a} = 0.134\, Re_a^{0.681}\, Pr_a^{0.333} \left(\frac{z}{y}\right)^{0.2} \left(\frac{z}{t}\right)^{0.1134} \qquad (3.13)$$

where $Pr_a = \dfrac{\mu_a C_{Pa}}{k_a}$ and $Re_a = \dfrac{m_a D_o}{\mu_a}$

The addition of fins greatly increases the air heat transfer rate. The parameter fin efficiency, η, is used to rate the thermal effectiveness of a fin. It is assumed that each tube is furnished by a circular-plate fin of equivalent surface area. The fin efficiency is

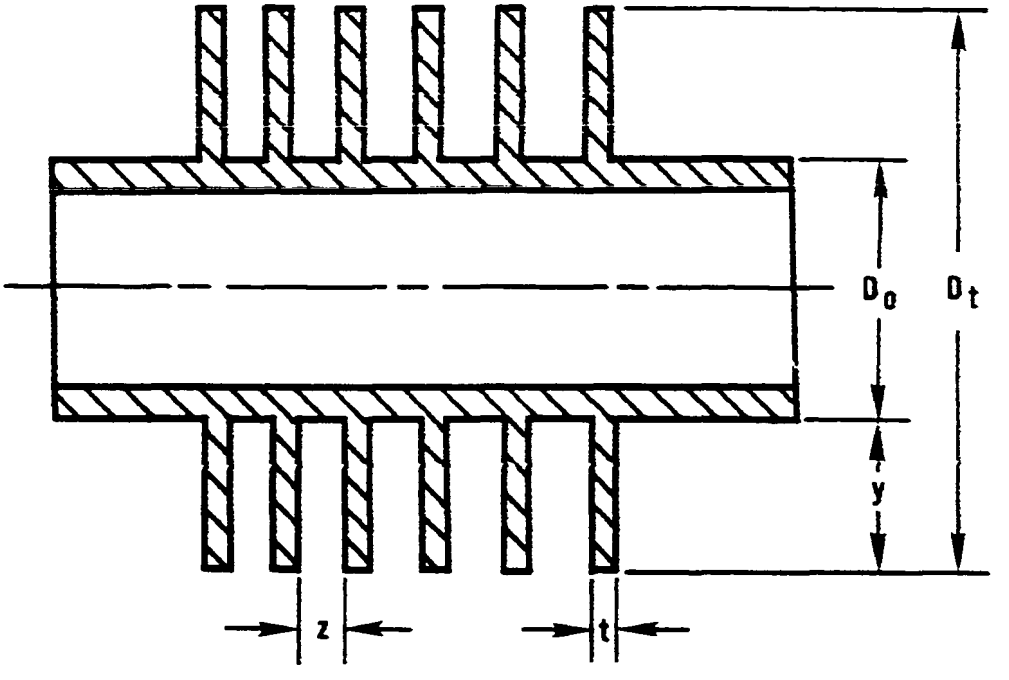

D_o = Tube Outside Diameter
D_t = Fin Tip Diameter
y = Fin Height
t = Fin Thickness
z = Distance Between Adjacent Fins

Figure 3.4 - Cross Section of a Flat-Finned Tube Indicating Parameters Which Affect the Air-Side Heat Transfer Coefficient

described in Eq. (3.14) and presented in terms of two dimensionless parameters [Briggs and Yong, 1962]:

$$\frac{D_o}{D_t} \qquad \text{and} \quad Y\left(\frac{2h_{c,o}}{k_f t}\right)^{0.5}$$

$$\eta = \sum_{j=1}^{8} \left(A_{1,j} + A_{2,j}\frac{D_o}{D_t} + A_{3,j}\left(\frac{D_o}{D_t}\right)^2\right)\left(Y\left(\frac{2h_{c,o}}{k_f t}\right)^{0.5}\right)^{j-1} \tag{3.14}$$

The coefficients, $A_{n,j}$, are given in Table 3.1.

Table 3.1 - Coefficients to be Used in Correlation of Fin Efficiency

J	A_{1J}	A_{2J}	A_{3J}
1	1.00000E+00	0.00000E+00	0.00000E+00
2	-0.22920E-01	-0.13755E+00	0.20130E-01
3	0.16106E+00	0.81890E-01	-0.11440E-01
4	-0.64975E+00	-0.55500E-01	-0.28753E-01
5	0.53491E+00	0.18040E-01	0.42477E-01
6	-0.19286E+00	0.36494E-03	-0.20335E-01
7	0.32564E-01	-0.10660E-02	0.40947E-02
8	-0.20972E-02	0.12410E-03	-0.29673E-03

Dry finned tube analysis is applicable to a condenser and also to an evaporator if no dehumidification takes place. The overall heat transfer coefficient, U, for a dry finned tube can be derived by summing the individual resistances between the refrigerant and the air.

$$U = \left[A_o/h_i A_{p,i} + A_o/h_{d,i} A_{p,i} + A_o t_p/A_{p,m} k_p + 1/h_{c,o}\left(1 - \frac{A_f}{A_o}(1-\eta)\right) \right]^{-1} \tag{3.15}$$

The first term in Equation 3.15 is the tube inside convection resistance which was

discussed above. The heat transfer coefficient for inside tube deposit, $h_{d,i}$, was assumed to be 5000 Btu/h.F.ft^2. The third term was the tube conduction. Finally, the fourth term was the outside convective resistance which was evaluated in Equation 3.13.

Overall Heat Transfer Coefficient of a Wet Finned Tube

The dehumidification process involves both sensible and latent heat transfer where the sensible heat transfer is associated with the decrease in dry bulb temperature and the latent heat transfer is associated with the decrease in humidity ratio. The heat transfer rate between the air stream and the finned-tube is presented in the following form [NIST, 1983]:

$$dQ = h_{c,o}\left(1 + \frac{l_{fg,w}(\omega_a - \omega_w)}{C_{Pa}(T_a - T_w)}\right)\left(1 - \frac{A_f}{A_o}\ (1 - \eta)\right)(T_a - T_w)\, dA_o \qquad (3.16)$$

The Lewis number is close to 1 for air at atmospheric pressure in the above equation. The one-dimensional heat conduction across the condensate film can be expressed by the following equation [as reported in NIST, 1983]:

$$dQ = h_L\, \Delta T_L\, dA_o \qquad (3.17)$$

Where $h_L = h_w/\delta$, is the heat transfer coefficient for condensate film. Using Equations (3.15) and (3.16), the following relation for overall heat transfer coefficient for a wet finned tube can be derived:

$$U = \left[\, A_o/h_i A_{p,i} + A_o/h_{d,i} A_{p,i} + A_o t_p/A_{p,m} k_p + 1/h_L + 1/E \,\right]^{-1} \qquad (3.18)$$

where,

$$E = h_{c,o}\left(1 + \frac{l_{fg,w}(\omega_a - \omega_w)}{C_{Pa}(T_a - T_w)}\right)\left(1 - \frac{A_f}{A_o}\ (1 - \eta)\right)$$

In the above equation for the overall heat transfer coefficient, it is assumed that the effect of water film conductance on fin efficiency is negligible and the temperature difference across the liquid film is uniform. The rate of moisture removal per unit area, R, can be calculated from the difference in humidity ratios.

$$R = \frac{m_a(\omega_{a,i} - \omega_{a,e})}{A_o} \tag{3.19}$$

the tube outlet humidity ratio, $\omega_{a,e}$, can be obtained from the following:

$$\omega_{a,e} = \omega_{a,i} - (\omega_{a,i} - \omega_w)(1 - exp\ [\frac{-h_{c,o} A_o (1 - \frac{A_f}{A_o}(1 - \eta))}{C_{Pa} m_a}]) \tag{3.20}$$

The dehumidification calculations are performed only if the evaporator temperature is above 32°F. Thus, the condensate flows down on the fin. The condensate thickness, δ_w, can be found by the following expression:

$$\delta_w = 1.083 (\frac{\mu_w R}{g \rho^2_w})^{1/3} \tag{3.21}$$

Pressure Drop in a Tube

Total pressure drop by the refrigerant in the heat exchanger is due to friction, momentum change and gravity. The pressure drop due to the gravity is very small and was neglected.

Single-Phase Flow

Frictional pressure drop for a single-phase flow in a tube is calculated by the Fanning equation as follows:

$$\Delta P = \frac{Re^{-0.2} m^2 L}{D \cdot \rho} \tag{3.22}$$

Pressure drop due to momentum change can be calculated by the following equation:

$$\frac{dP}{dL} = - m^2 \frac{dv}{dL} \tag{3.23}$$

Two-Phase Flow with Condensation

Frictional pressure drop for two-phase flow with condensation is related to the pressure drop of the liquid portion of the flow flowing alone in the pipe and correction factor, Θ, for two-phase pressure drop. This correction factor, Θ, was proposed by Lockhart and Matinelli [1949]. They performed a semi-empirical study of adiabatic two-phase flow with air and several different liquids in pipes varying in diameter from 0.586 to 1.017 inch. The frictional pressure drop was calculated from the following relationship:

$$\Delta P_{tp} = \Delta P_L \cdot \Theta \tag{3.24}$$

To determine ΔP_{tp}, first the pressure drop of the liquid portion of the flow must be evaluated. ΔP_L can be calculated by the single-phase pressure drop relation given in Eq. 3.22.

$$\Delta P_L = 0.092 \, (Re_{tp,L})^{-0.2} \, \frac{m^2 L}{D \rho} \tag{3.25}$$

where the liquid Reynolds number, $Re_{tp,L}$, can be calculated as follows:

$$Re_{tp,L} = \frac{(1 - x) m D}{\mu_L} \tag{3.26}$$

The correction factor, Θ, was correlated for horizontal two-phase flow of two-component systems at low pressure as a function of X_{tt} which is defined in Eq. 3.11.

$$\Theta = 10^{B} \tag{3.27}$$

where,

$$B = \sum_{i=1}^{5} A_i (\log X_{tt})^{i-1}$$

$A_1 = 1.4$

$A_2 = -0.87917$

$A_3 = 0.14062$

$A_4 = 0.0010417$

$A_5 = -0.00078125$

Two basic postulates were used to establish the correlation [Lockhart and Matinelli 1949]:

(a) Four flow regimes were defined on the basis of the behavior of the flow (viscous or turbulent).

(b) The liquid and gas phase pressure drops were considered equal irrespective of the details of the particular flow pattern.

Combining Equations (3.25), (3.26) and (3.27), the two-phase pressure drop equation has the following form:

$$\Delta P_{tp} = \frac{2 f_{tpL} m^2 (1-x)^2 L \Theta}{(D \rho_L)} \tag{3.28}$$

Equation 3.28 was developed based on several assumptions for two-phase flow pressure drop by Lockhart and Martinelli. The flow of both the liquid and the gas were assumed to be turbulent and artificially segregated into two streams. The stream velocities were assumed constant but not necessarily equal for the vapor and liquid phases. It was further assumed that thermodynamic equilibrium exists at all points in the flow.

The pressure drop due to momentum change for separated two-phase flow can be estimated by the following equation:

$$\frac{dP}{dL} = -m^2 \frac{d}{dL}\left[\frac{v_V x^2}{\alpha} + \frac{v_L(1-x)^2}{(1-\alpha)}\right] \tag{3.29}$$

Equation 3.29 is a function of void fraction, α, which is the ratio of tube cross-sectional area occupied by vapor to total cross-sectional area occupied by two-phase flow. The void fraction, α, was correlated by Wallis [1969] in term of X_{tt}.

$$\alpha = (1 + X_{tt}^{0.8})^{-0.378} \qquad \text{for } X_{tt} < 10 \tag{3.30}$$

$$\alpha = 0.823 - 0.157\, Ln\,(X_{tt}) \qquad \text{for } X_{tt} > 10 \tag{3.31}$$

The correlation between α and X_{tt} as derived by Wallis (Eqs. 3.30 and 3.31) is independent of flow regime.

Two-Phase Flow with Evaporation

The pressure drop for two-phase flow with evaporation is calculated by the correlation proposed by Pierre [1964], based on his experiments with refrigerants R-12 and R-22. In Pierre's correlation, the homogeneous model which considers the two phases flow as a single phase possessing mean fluid properties was assumed. It was also assumed that the velocities of the vapor and of the liquid were identical, so that flowing medium could be considered a homogeneous vapor-liquid mixture. This assumption was reasonably validated by the visual observations made during the experimental tests. It was further assumed that the flow resistance due to friction was generated from a shear force on the wetted tube wall and the flow resistance was a function of vapor-liquid mixture velocity [Pierre, 1964].

$$\Delta P = (f\frac{L}{D} + \frac{\Delta x}{x_m}) m^2 v_m \qquad (3.32)$$

The first term of above equation is for fractional pressure drop while the second is for the pressure drop due to change of momentum. The empirical friction factor to be used in Eq. (3.32) is presented as followings:

$$f = 0.0185 (Re \frac{L}{J I_{fg} \Delta x})^{0.25} \qquad (3.33)$$

In Equation 3.33, the term, $J I_{fg} \Delta x$, is considered as a boiling number which make the friction factor sensitive to vapor generation rate at the vapor-liquid interface.

The tube-by-tube approach to coil simulation has been explained in detailed. The input to coil simulation program is coil geometry data, refrigerant flow distribution sequence, and air and refrigerant inlet conditions. Appendix A provides details of the input data used to calculate the unit performace data. The block diagram for the refrigerant side heat transfer calculation is shown in Figure 3.5.

To illustrate the effects of "branch" circuitry found in the heat exchanger model on the system performance, the ORNL and modified ORNL models were run for the unit with a capillary tube expansion device at 80°F DB and 82°F DB indoor and outdoor temperatures, respectively. The unit refrigerant charge was set at 154 ounces and the Hughmark void fraction model was used for both simulations. The unit performance data were compared with the experimental results and shown in Table 3.2. The predicted superheat temperature by the modified ORNL model was within 2°F of measured superheat. The evaporator outlet refrigerant temperature and pressure predicted by the modified ORNL model were closer to the measured data that those of ORNL model. The predicted evaporator capacity was within 2% and 12% of the measured evaporator

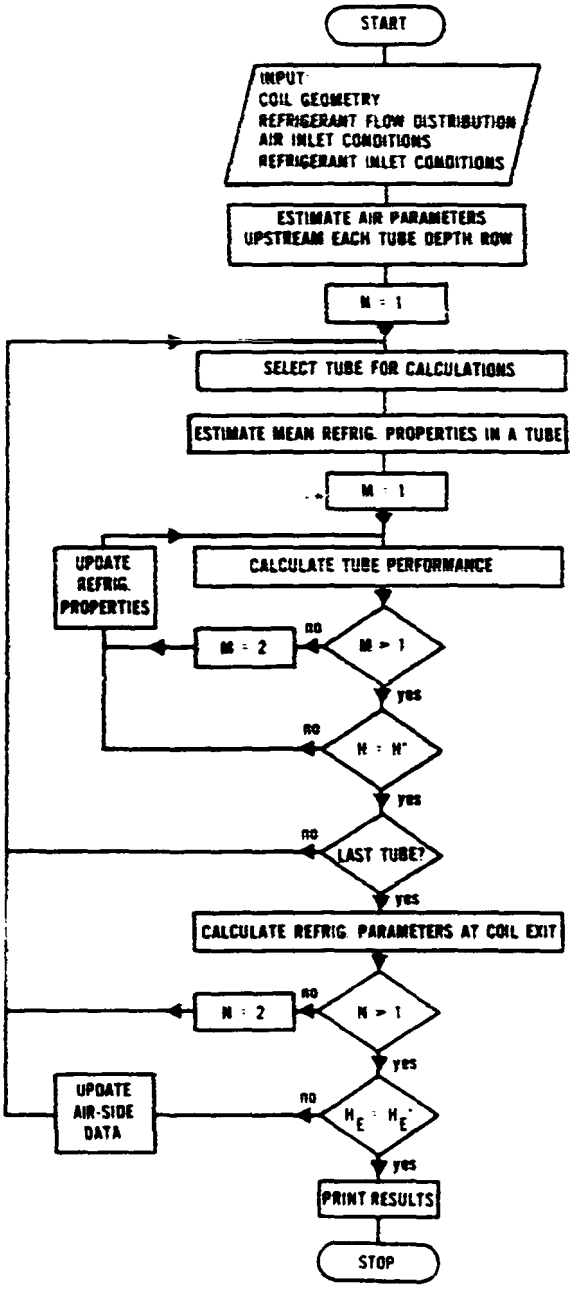

Figure 3.5 - Flow Chart for the Heat Exchanger Simulation Program

capacity for the modified ORNL and ORNL models, respectively. The precise prediction of the evaporator capacity by the modified ORNL model was the result of close prediction of the refrigerant flow rate and superheat temperature. The predicted EER was within 3.4% and 15.4% of the measured *EER* for the modified ORNL and ORNL models, respectively.

Table 3.2 - The Comparison of the Predicted System Performance with the Measured Data

System Parameters	ORNL Model	Modified ORNL Model	Measured Data
Superheat (F)	7.7	0.0	2.0
Evp. Inlet Temp.(F)	48.7	49.6	N/A
Evp. Outlet Temp. (F).	51.6	46.2	48.0
Evp. Inlet P. (psia)	96.6	98.0	N/A
Evp. Outlet P. (psia)	90.9	92.7	92.1
Ref. Flow (lbm/hr)	531	519	498
Evap. Cap. (kbtu/hr)	40.2	36.5	35.8
Unit Cap. (kbtu/hr)	38.7	35.1	34.2
Unit *EER*	11.3	10.1	9.77

CHAPTER IV

EXPERIMENTAL APPARATUS AND PROCEDURE

The objective of the experimentation was to quantify the effect of refrigerant charge on the performance of a residential air conditioner during steady state and cyclic operations. The data included pressures and temperatures of refrigerant throughout the system, temperatures, pressure and humidity of air across the heat exchangers, power consumption of compressor and fan, and refrigerant and air flow rates. An experimental apparatus was constructed that consisted of: (i) existing psychrometric rooms, (ii) indoor test section, (iii) outdoor test section, (iv) test air conditioner, and (v) a data acquisition system. Also, a procedure was established for testing that would ensure the repeatability and reliability of the test data. These are described below.

PSYCHROMETRIC ROOMS

The air conditioner was located in the psychrometric rooms of the Energy System Laboratory (ESL) at the Texas A&M University Riverside Campus Research Center. The placement of the air conditioner and associated instrumentation is shown in Figure 4.1. The psychrometric rooms simulated the indoor and outdoor conditions (temperature and humidity) necessary for all experiments. These rooms were constructed and maintained according to the American Society of Heating Refrigeration and Air-Conditioning Engineers (ASHRAE) specifications [ASHRAE Standard, 1983]. Dew point and room temperatures could be maintained within +/-0.2 F of the set point. The room temperature was controlled by a Texas Instruments PM-550 controller.

Room temperatures were maintained with chilled water coils and electric resistance heaters. The chilled water coils were fed with an ethylene glycol solution that was chilled by a 150 ton capacity chiller. A 300 gallon chilled water thermal storage tank was mounted in the chilled water system to provide some thermal capacity. There

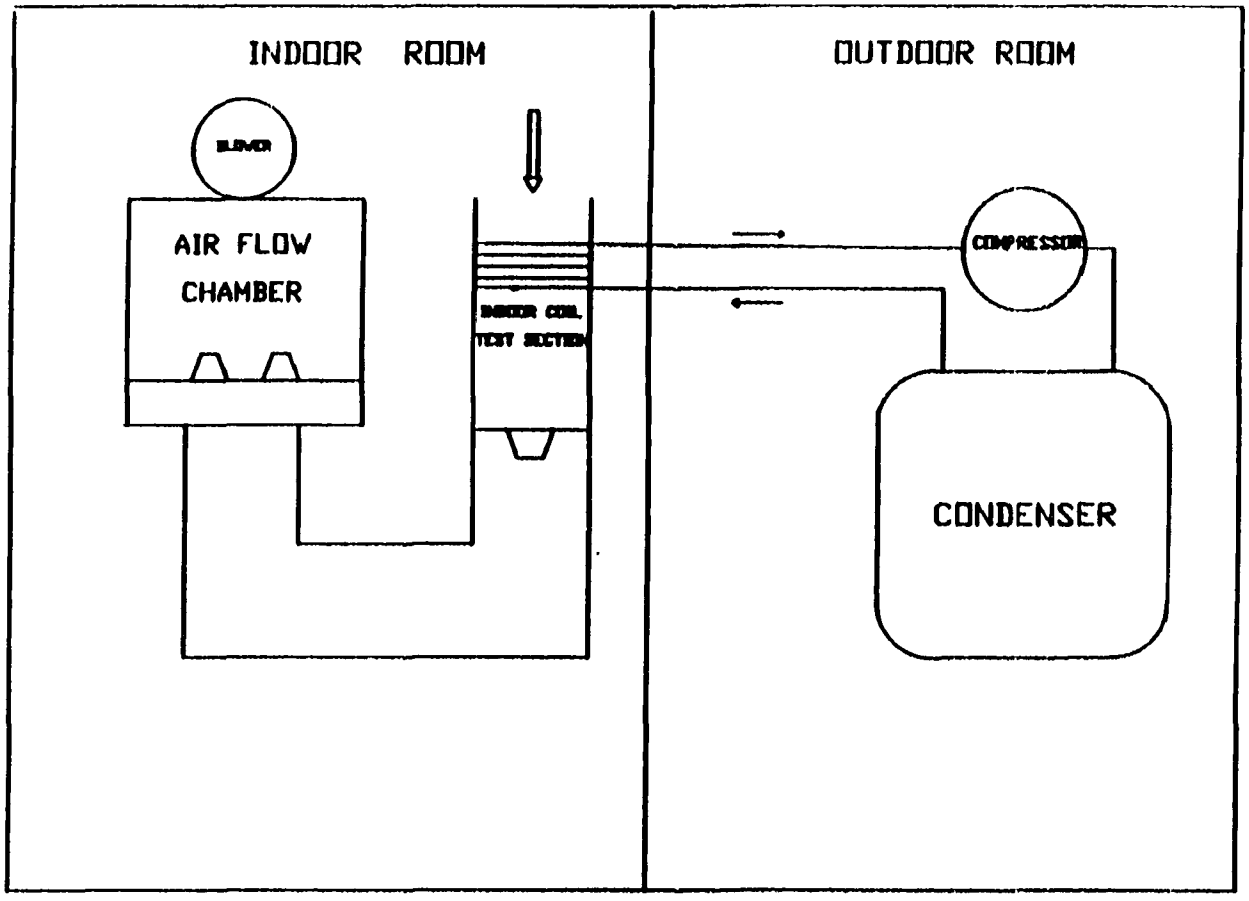

Figure 4.1 - The Placement of the Air Conditioner and Associated Instrumentation

were four banks of electric heaters in each room with 9900 watts per bank.

Humidity in the rooms was controlled by electric humidifiers and dehumidification coils. The dehumidification coils were fed from the same circuit as the cooling coils. The humidifiers were mounted in each room and supplied steam directly into the supply air duct.

The indoor test section consisted of the indoor coil (evaporator) and the indoor air flow chamber. Conditioned air from the indoor room was drawn through the indoor test section by the air flow chamber fan. A damper was mounted on the outlet that was adjustable and was set to maintain a constant air flow of 1200 cubic feet per minute(cfm) through the indoor test coil. The air was routed back into the indoor room after leaving the chamber.

The outdoor room section consisted of the compressor and outdoor coil. The conditioned outdoor air entered the outdoor coil and was exhausted by the unit fan back into the room through the outdoor coil.

INDOOR TEST SECTION

In the indoor test section (Figure 4.2), conditioned air flowed through a 22x34 inch, one-inch insulated sheet metal duct. A set of straighteners was used as the air entered this section. The air temperature was measured by a 16-element thermocouple grid before it entered the coil. Next, the air flowed through a set of mixers which removed any temperature stratifications caused by non-uniform heat exchange with the indoor coil of the air conditioner. There were two dampers installed before and after the coil. The dampers were driven by two hydraulic actuators which were controlled by an "on-off" switch from the control room. After leaving the coil, the air again passed through flow straighteners. A downstream 16-node thermocouple grid was used to measure air temperature after it was mixed and straightened. Finally, the air entered the

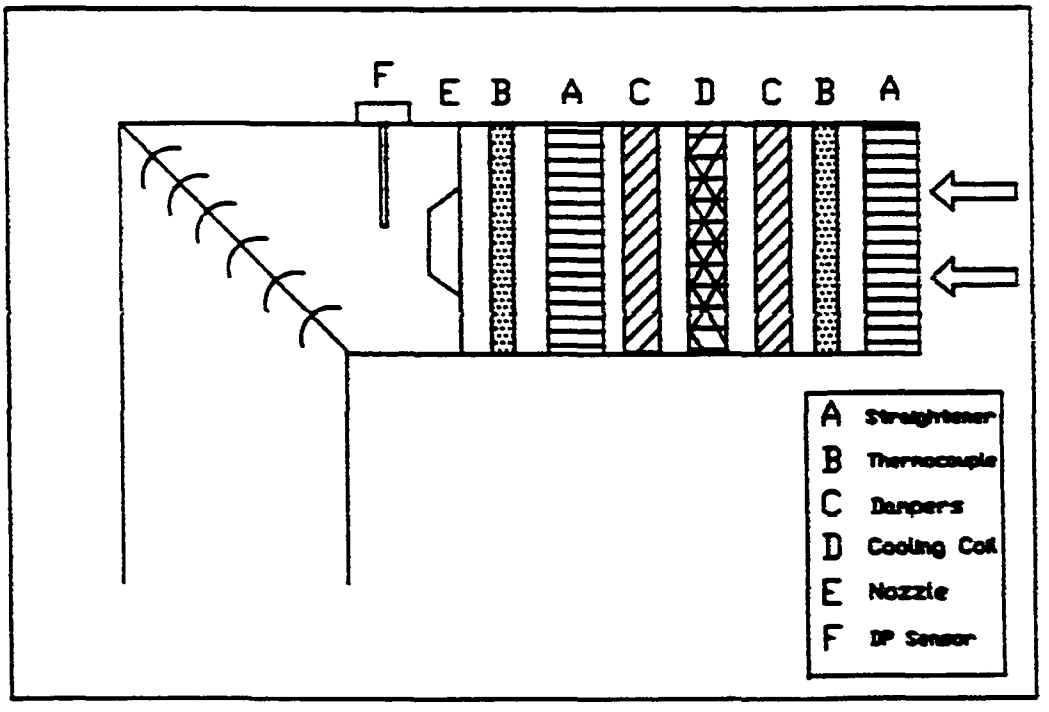

Figure 4.2 - Detail of Indoor Test Section

flow chamber for flow rate measurement. Flow straighteners, mixers, and thermocouple grids were constructed following ASHRAE Standard 41.1-74 [1974], which specifies procedures for temperature measurement.

To measure the dew point temperature accurately, the dew point sensors had to be mounted in an air stream of 500 to 3000 fpm. An air sampler was constructed to sample the air entering the indoor coil. The sampler was a 4x6 inch duct with a fan at the end of the duct. The fan drew air through the duct where the dew point sensor was mounted. The air velocity through the duct was approximately 1700 fpm which was within the operating range of the sensor. A 12-inch nozzle was mounted after the second 16-element thermocouple grid to increase the velocity of air up to 1500 fpm for the down stream dew point sensor. In addition to the optical mirror dew point sensors, a dry/wet bulb thermometer test rig placed in the vicinity of the test section measured the condition of the air entering the test section. The test rig used a small centrifugal fan to pull air across a dry-bulb thermometer and a thermometer whose bulb was wetted with a cotton sock saturated with distilled water.

After leaving the test section, the air was drawn into an Air Movement and Control Association (AMCA) 210 flow chamber [1985] where the air flow was measured. The chamber contained four ASME air flow nozzles (one-8, two-5, and one-3 inch diameters) that could be used in any combination to measure accurately a flow range of 100 to 5000 cfm. A booster fan mounted on the end of the chamber provided the air flow through the setup. The air flow was adjusted by operating a set of dampers mounted on the fan outlet. For the steady state and cyclic tests, two 5 inch nozzles were used in the chamber to achieve a pressure drop of 1.13 inch WG which was equivalent to 1150 cfm through the indoor test coil.

OUTDOOR TEST SECTION

The outdoor test section included the compressor, the outdoor coil (condenser), and a turbine flow meter, (Figure 4.3). The outdoor coil had one row with spine fins at 20 fins per inch. The face area of the coil was 20.94 ft^2 with refrigerant tube sizes of 3/8 inch. The outdoor fan was located on the top of the outdoor coil. The fan specifications are given in Table 4.1.

Table 4.1 - Fan Specifications.

Fan Type	Propeller
Diameter	22
Drive Type	Direct
CFM @ 0 in. w.g.	2735
Motor HP	1/4
Motor Speed RPM	825
F.L. Amps	1.9

The temperature of the air leaving the outdoor coil was measured by a 6 element thermocouple grid. According to ARI standard, the wet bulb temperature was not required when testing an air-cooled condenser which did not evaporate condensate.

TEST AIR CONDITIONER

A nominal 3-ton capacity split-system residential Trane air conditioner (Model TTX736A100A1/TWV742) was used in this experiment. The indoor heat exchanger was a four-row, four-circuit vertical coil. Refrigerant tubing in the coil was 3/8 inch nominal diameter copper tubing. Vertical extended surfaces were placed on the tubing at 12 fins per inch. These fins were wavy and are commonly used in the air-conditioning industry.

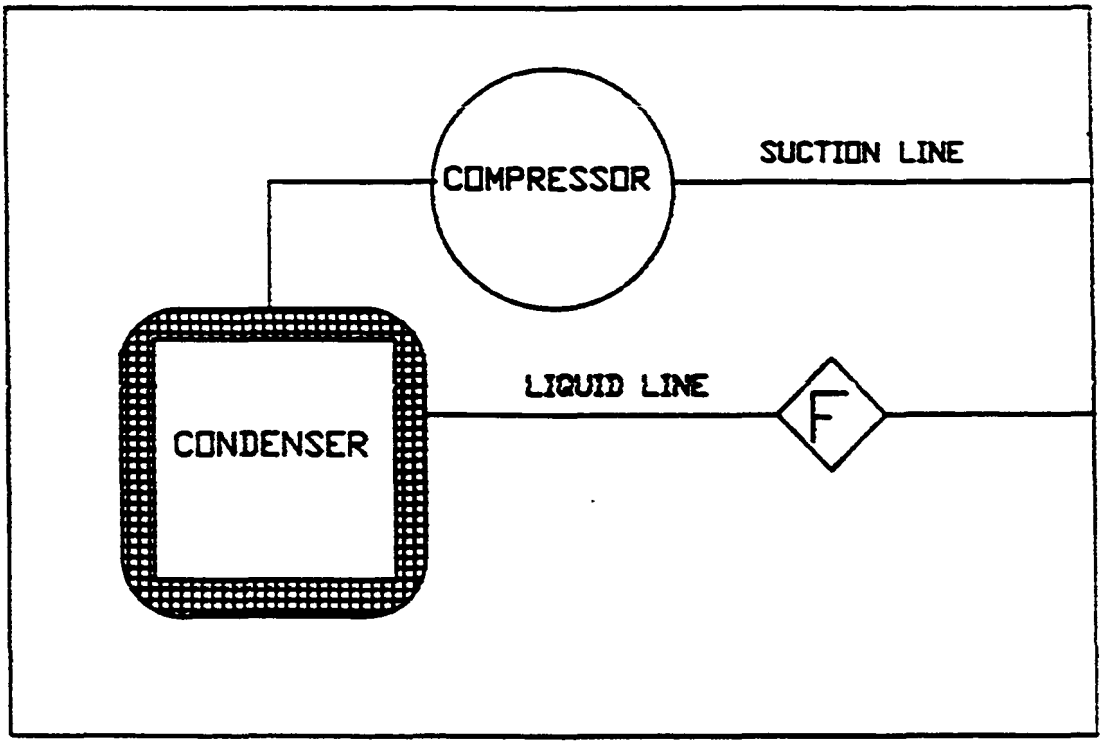

Figure 4.3 - Detail of Outdoor Test Section

Each row of the coil had fifteen total passes of the horizontal refrigerant tubing. The coil frontal area was 3.33 ft^2, and was rated at three tons capacity. A capillary tube was used as the expansion device with this unit. The capillary tube diameter and length was 0.1 and 26 inches, respectively.

An A-shape coil was used with a thermal expansion valve and an short-tube orifice. The TXV was rated at three ton capacity and the superheat at rating condition was 11°F. The short-tube orifice diameter was 0.071 inches. The indoor heat exchanger was a three-row, four-circuit A-coil. The vertical extended surfaces were placed on the tube at 14 fins per inch. Each row of the coil had nine total passes of the horizontal refrigerant tubing. Each leg of the coil had 15 inches wide and 18.5 inches high. The coil was rated at three ton capacity.

REFRIGERANT SIDE

A schematic of the refrigerant circuit is shown in Figure 4.4. Refrigerant pressures were monitored at the 6 points shown with the use of 0-300 and 0-500 psig pressure transducers. To measure accurately the refrigerant temperatures and reduce the conduction effects of the copper tubing, seven thermocouple probes were installed in the refrigerant lines. The probes were 1/16 inch diameter and mounted far enough into the flow of the refrigerant to minimize the tube conduction effects (Figure 4.5).

Refrigerant mass flow was measured with two mass flow meters mounted in parallel. The flow meters measured mass flow according to the Coriolis principle as the refrigerant flows through a U-shaped tube. The flow meters were placed on the liquid line after the condenser unit (Figure 4.4). The flow rate through the meters varied from 0 to 10 pounds per minute with a pressure drop at maximum flow rate of approximately 10 psi. This pressure drop was less than the 12 psi pressure drop acceptable by ASHRAE Standard 116-83 (12 psi is the equivalent pressure drop for refrigerant at the test

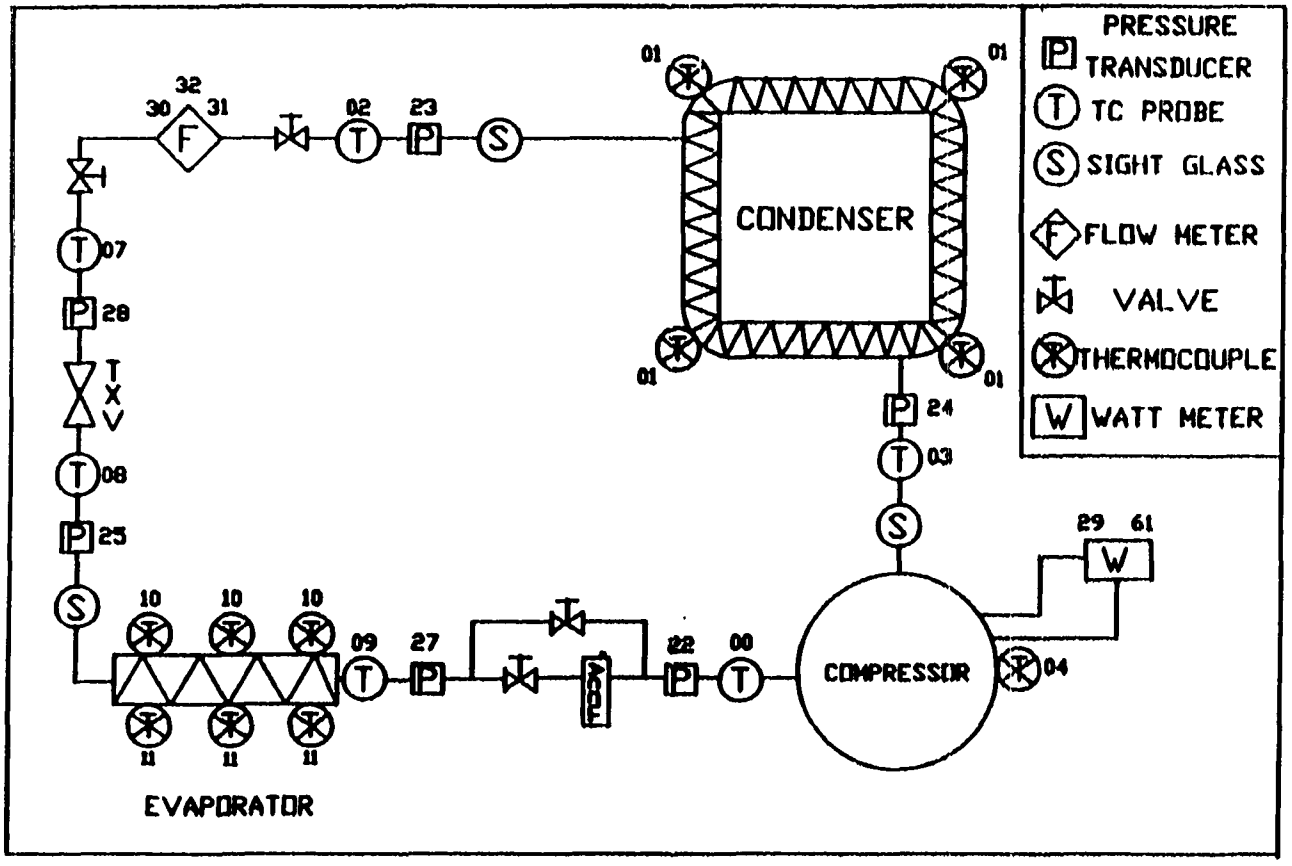

Figure 4.4 - Schematic of the Refrigerant Circuit

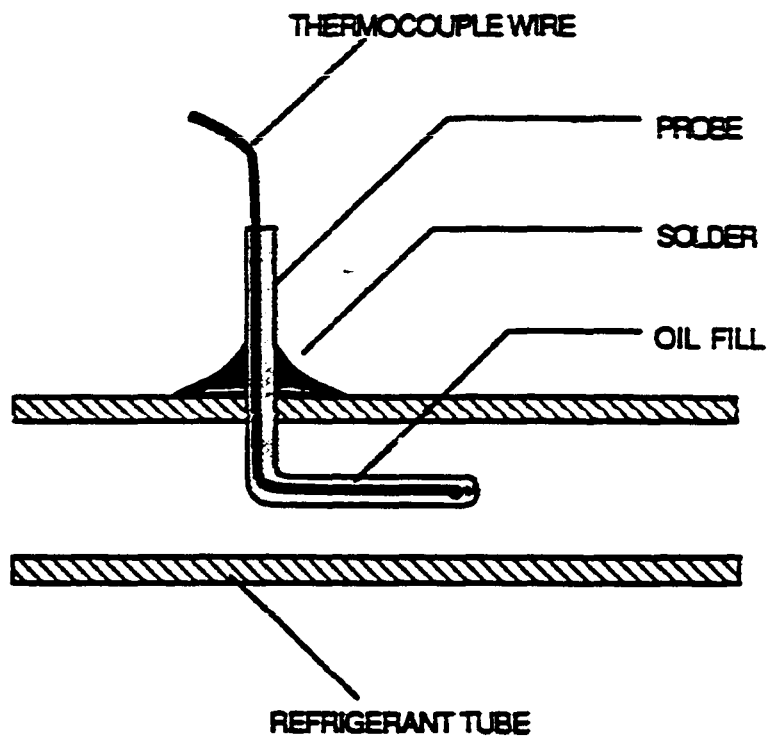

Figure 4.5 - A Typical Refrigerant Temperature Probe

conditions experiencing the maximum allowed temperature drop of 3°F).

The valves shown in the refrigerant circuit diagram were lever-actuated shut-off valves. Several ball valves were mounted around all sections of the refrigerant circuit to allow easy disassembly of the unit without any loss of refrigerant charge. Charging taps in each section of the circuitry allowed purging and charging of each section independently.

DATA ACQUISITION

Sensor signals from the test points listed in Table 4.2 were collected and converted to engineering units by an Acurex (model Autocalc) data logger. The data logger handled millivolt and milliamp signals as well as larger voltages and frequency signals. During each test, the data processed by the data logger was transferred to a portable Compaq personal computer where it was stored on a 10 megabyte hard disk. The maximum collection and storage rate for the set of data channels used in a test was eight seconds per set. The scan rate was adjustable, so data from each test (cyclic and steady state) were collected every 15 seconds.

A feature of the data acquisition set-up was the continual display of run-time data on the screen during testing. After completion of a test series, all data collected on the hard disk were transferred to a VAX minicomputer for analysis. Data were backed up on floppy disks. All data analysis programs were written in FORTRAN. Refrigerant and moist air property subroutines were used in calculation of air and refrigerant-side cooling capacities to provide an energy balance for data validation. Additional calculated properties and performance parameters for each test were plotted.

TESTING PROCEDURE

The first step of the procedure was to set the system refrigerant charge. Three expansion devices were used: thermal expansion valve (TXV), capillary tube, and

Table 4.2 - Description of Test Points Used in the Test Set-Up

Channel	Sensor	Location
00	TC-Probe	Compressor Inlet
01	Thermocouple	Outdoor Room Temp.
02	TC-Probe	Condenser Outlet
03	TC-Probe	Compressor Outlet
04	Thermocouple	Compressor Shell Temp
05	Thermocouple	Before Nozzle-Chamber
06	Thermocouple	After Nozzle-Chamber
07	TC-Probe	TXV Inlet Temp.
08	TC-Probe	Evap.Inlet Temp.
09	TC-Probe	Evap.Outlet Temp.
10	TC-Grid	DB Indoor Coil Outlet
11	TC-Grid	DB Indoor Coil Inlet
12	Thermocouple	Chilled Water Temp.
13-20		-- Not Used --
21	Dew-Point	Downstream Indoor Coil
22	Dew-Point	Upstream Indoor Coil
23	Pressure Trans.	Compressor Inlet
24	Pressure Trans.	Condenser Outlet
25	Pressure Trans.	Compressor Outlet
26	Pressure Trans.	Evaporator Inlet
27	Pressure Trans.	Evaporator Outlet
28	Pressure Trans.	TXV Inlet
29	Watt Trans.	208 VAC (kw)
30	Flow Meter	Ref. Liquid Line
31	Flow Meter	Ref. Liquid Line
32		Sum of 30 & 31
33-60		-- Not Used --
61	WattHr Trans.	Compressor Powe

short-tube orifice. The manufacturer charging recommendations called for a certain superheat leaving the evaporator for capillary tube and short-tube orifice expansion devices. For the TXV, a fixed subcooling temperature leaving the condenser was used for setting the charge in the system. Initially, the charge was set at an outdoor temperature of 95°F and indoor conditions of 80°F dry bulb and 67°F wet bulb. Refrigerant was added to the system in one ounce increments until the desired subcooling or superheat was obtained. The full charge for each expansion device according to the manufacturer's suggestion is shown in Table 4.3 along with the measured superheat or subcooling attained for the full charge.

Once the full charge was determined, a set of tests was performed at that charge. The system was then evacuated of refrigerant. Refrigerant was then added in 5% increments from -20% of full charge to +20% of full charge to cover the full range of charging conditions for the particular expansion device being tested. The system with the TXV was also subjected to 40% and 30% undercharging to determine the effects of severe refrigerant off-design conditions on the system performance. A scale was used to weigh the refrigerant added to the system.

Table 4.3 - Refrigerant Charge and the Corresponding Superheat or Subcooling Temperature for each Expansion Device.

Expansion Device	Refrigerant Charge (oz)	Superheat(F) and Subcooled(F)
Cap.tube	140	7.4 (sup)
Orifice	136	8.5 (sup)
TXV	140	13.5 (sub)

The steady state and cyclic tests recommended by the Department of Energy (DOE) were run to estimate the effect of charge on the seasonal performance of the system. The DOE test procedure calls for four tests: A, B, C, and D. The DOE test procedure requires two steady state tests (A and B) in which dehumidification occurs on the evaporator coil. Both tests are at the same indoor conditions (80°F DB and 67°F WB) and at two outdoor temperatures (82°F and 95°F). In addition to the two outdoor temperatures required by the test procedure, steady state tests were also performed at two more outdoor temperatures (90°F and 100°F) to determine the influence of outdoor temperature on energy consumption and cooling capacity. The DOE test procedure also requires testing of an air conditioner under conditions in which no condensation would occur on the evaporator coil (C and D). Both steady state and cyclic tests were performed with indoor conditions set at 80°F DB and 57°F WB. The wet bulb temperature was sufficiently low enough so that no condensate formed on the evaporator coil. The outdoor room was constantly kept at 82°F DB and 20% relative humidity during these tests. Test A was used to determine the rated capacity and tests B, C, and D were used to determine the *SEER* of the unit.

The cooling cyclic test was conducted by cycling the compressor 6 minutes "on" and 24 minutes "off". During the "on" period, electrical energy and capacity measurements were made. According to the ASHRAE Standard [1983] test procedure, during the first two minutes of the "off" period, the capacity was also measured. Then the evaporator coil was isolated by shutting off the dampers during the "off" time for 22 minutes. The capacity was calculated for the 8 minutes (the six minutes during the "on" cycle and two minutes after). All electrical energy (outdoor fan and compressor) was measured for the "on" time of 6 minutes. The indoor fan power for the time period during 6 and 8 minutes was added to the measured electrical energy. The power was calculated based on 365 watts per 1000 cfm of air [ASHRAE Standard test procedure,

1983].

For all the tests, the psychrometric rooms were operated for more than one hour to allow the rooms and the equipment inside them to stabilize to the pre-set conditions before initiating a test run. The rooms were always maintained within the tolerance prescribed by the ASHRAE Standard [1983]. For steady state tests, the air conditioner was operated for more than 30 minutes until equilibrium conditions were attained in the rooms. Data was then recorded at fifteen-second intervals for 40 minutes. For cyclic tests, due to the change in indoor and outdoor rooms conditions during the start up of the unit, the test was repeated four times. This procedure was established for testing that would ensure the repeatability and reliability of the test data.

The cooling capacity was measured by two methods: indoor air enthalpy and the refrigerant enthalpy. According to the ASHRAE Standard [1983], the total instantaneous cooling capacity obtained from air-enthalpy must be within +/-5% of refrigerant-enthalpy. All measurements and calculations were in compliance with the ASHRAE Standard [1983]. The air-side capacity is the sum of the latent and sensible capacities based on the indoor side test data and is estimated from the following equations:

Sensible,

$$q_s = \frac{60\, Q_a\, C_{pa}(T_{i,a} - T_{o,a})}{[v_n(1+w_n)]} \tag{4.1}$$

Latent,

$$q_l = \frac{636000\, Q_a\, (w_{i,a} - w_{o,a})}{[v_n(1+w_n)]} \tag{4.2}$$

Total,

$$q_t = \frac{60\, Q_a(h_{i,a} - h_{o,a})}{[v_n(1+w_n)]} \tag{4.3}$$

The refrigerant side heat transfer is calculated from the following equation:

$$q_r = m_r (h_{i,r} - h_{o,r}) \tag{4.4}$$

The steady state energy efficiency ratio (*EER*) of the unit is determined from the air side measurements and is given by:

$$EER_{ss} = \frac{q_t}{E_t} \tag{4.5}$$

A number of variables are used to quantify the *SEER*. These include: the steady state dry coil energy efficiency ratio (EER_C), the cyclic energy efficiency ratio (EER_D), the cooling load factor (*CLF*), the part load factor (*PLF*), and the degradation coefficient (C_D). A non-dimensional parameter which is widely used to compare the steady state and cyclic efficiency is the part load factor (*PLF*). The EER_D is the ratio of the cyclic heat removal rate from the conditioned space (Btu/hr) to the cyclic energy input (watts).

The calculation of the *SEER* with a single-speed compressor and single-speed condenser fan is done according to the ASHRAE Standard [1983]. First, a cyclic-cooling-load factor (*CLF*) is determined from:

$$CLF = \frac{Q_D}{(Q_C t_C)} \tag{4.6}$$

The degradation coefficient, C_D, is the measure of the efficiency loss due to the cyclic of the unit. C_D is calculated from:

$$C_D = \frac{(1 - \frac{EER_D}{EER_C})}{(1 - CLF)} \tag{4.7}$$

Therefore, *SEER* can be estimated. According to the ASHRAE Standard [1983] the

SEER is defined as:

$$SEER = \frac{\Sigma_{j=1,n} LF(T_j)\, q_{ss}(T_j) n_j}{\Sigma_{j=1,n} [\, LF(T_j)\, E_{ss}(T_j) n_j / PLF \,]} \tag{4.8}$$

where,

$$LF(T_j) = \frac{BL(T_j)}{q_{ss}(T_j)} \tag{4.9}$$

the building load, $BL(T_j)$, is estimated from:

$$BL(T_j) = \frac{(5j - 3)\, q_{ss}(T_{od})}{(T_{od} - 65)\, SF} \tag{4.10}$$

T_{od} is the outdoor design temperature and SF, the size factor, is the amount normally 10% of over or undersizing desired. For all the equations:

j = 1,2,3 ....,n correspond to the j^{th} temperature bin

n = total number of non-zero temperature bins in the climatic region

Substituting Eq. 4.9 into Eq. 4.8

$$SEER = \frac{\Sigma_{j=1,n} BL(T_j) n_j}{\Sigma_{j=1,n} [BL(T_j)\, E_{ss}(T_j) n_j / q_{ss}(T_j)\, PLF]} \tag{4.11}$$

$$EER_{ss}(T_j) = \frac{q_{ss}}{E_{ss}} \tag{4.12}$$

$$SEER = \frac{\Sigma_{j=1,n} BL(T_j) n_j}{\Sigma_{j=1,n} [BL(T_j) n_j / EER_{ss}(T_j)\, PLF]} \tag{4.13}$$

SEER is then determined from a bin hours cooling method calculated based on the representative use cycle of 1000 cooling hours per year. A 95°F cooling outdoor design temperature was used. In accordance with the ARI test procedure, the cooling building load size factor 1.1 (10% oversizing) was used.

EXPERIMENTAL TESTS

A series of tests was run to investigate the influence of the charge and outdoor temperature on the performance of the air conditioner. The tests conducted for each expansion device included the steady state wet coil tests shown in Tables 4.4 - 4.6 as well as the standard DOE/ARI tests (A-D) to determine *SEER*. The indoor condition was set at 80°F dry-bulb temperature and 65°F wet-bulb for the wet coil tests. For the dry coil steady state and cyclic tests (C and D), the indoor condition was set at 80°F DB and 57°F WB.

Table 4.4 - Steady State Tests Varying Refrigerant Charge in the System with the TXV

Charge	OUTDOOR TEMPERATURE			
	82	90	95	100
-40%	X	X	X	X
-30%	X	X	X	X
-20%	X	X	X	X
-15%	X	X	X	X
-10%	X	X	X	X
-5%	X	X	X	X
Full	X	X	X	X
+5%	X	X	X	X
+10%	X	X	X	X
+15%	X	X	X	X
+20%	X	X	X	X

Table 4.5 - Steady State Tests Varying Refrigerant Charge in the System with the Short-Tube Orifice

Charge	OUTDOOR TEMPERATURE			
	82	90	95	100
-20%	X		X	
-15%				
-10%	X	X	X	X
-5%	X		X	
Full	X	X	X	X
+5%	X		X	
+10%	X	X	X	X
+15%				
+20%	X		X	

Table 4.6 - Steady State Tests Varying Refrigerant Charge in the System with the Capillary Tube

Charge	OUTDOOR TEMPERATURE			
	82	90	95	100
-20%	X	X	X	X
-15%	X	X	X	X
-10%	X	X	X	X
-5%	X	X	X	X
Full	X	X	X	X
+5%	X	X	X	X
+10%	X	X	X	X
+15%	X	X	X	X
+20%	X	X	X	X

CHAPTER V

BASE CASE STEADY STATE AND CYCLIC TESTS FOR FULL CHARGING CONDITIONS

Four variables were used to quantify the overall performance of the unit: total capacity, total electrical power consumption, energy efficiency ratio (*EER*), and seasonal energy efficiency ratio (*SEER*). The unit was charged according to the procedures specified by the manufacturer. The steady state and cyclic tests were compared with those from the manufacturer.

STEADY STATE TESTS (Wet Coil) RESULTS

The DOE A and B tests were run to compare the experimental results with those from the manufacturer. Both tests are at the same indoor room conditions (80°F DB and 67°F WB) and at two outdoor temperature (82°F and 95°F). In addition to the two outdoor temperatures required by the test procedure, steady state tests were also performed at two more outdoor temperatures (90°F and 100°F). The air flow rate across the cooling coil was maintained at 1150 cfm. The flat indoor coil was used with the capillary tube expansion system. In the case of the TXV and the short-tube orifice expansion systems, the A-shape indoor coil was used.

The total instantaneous cooling capacity obtained from the air-enthalpy and refrigerant enthalpy calculation varied +/- 5%. This agreement was within the ASHRAE test standard requirements [1983] and was observed in all test data that were retained during the current experimentation. Only the air-side measurements were used to characterize the capacity of the various tests. The steady state results compared well with the manufacturer's data (within +/-5%). Figures 5.1 and 5.2 show the unit net total capacity (sensible and latent) and *EER* as a function of outdoor temperature for each expansion device under the fully charged condition. Both the capacity and *EER*

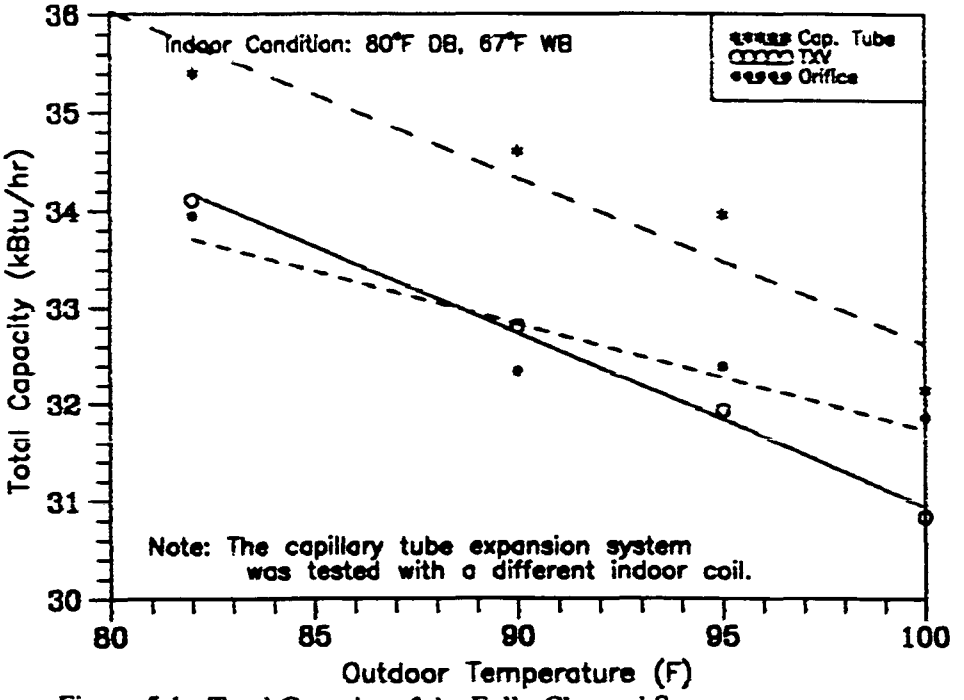

Figure 5.1 - Total Capacity of the Fully Charged System with Various Expansion Devices

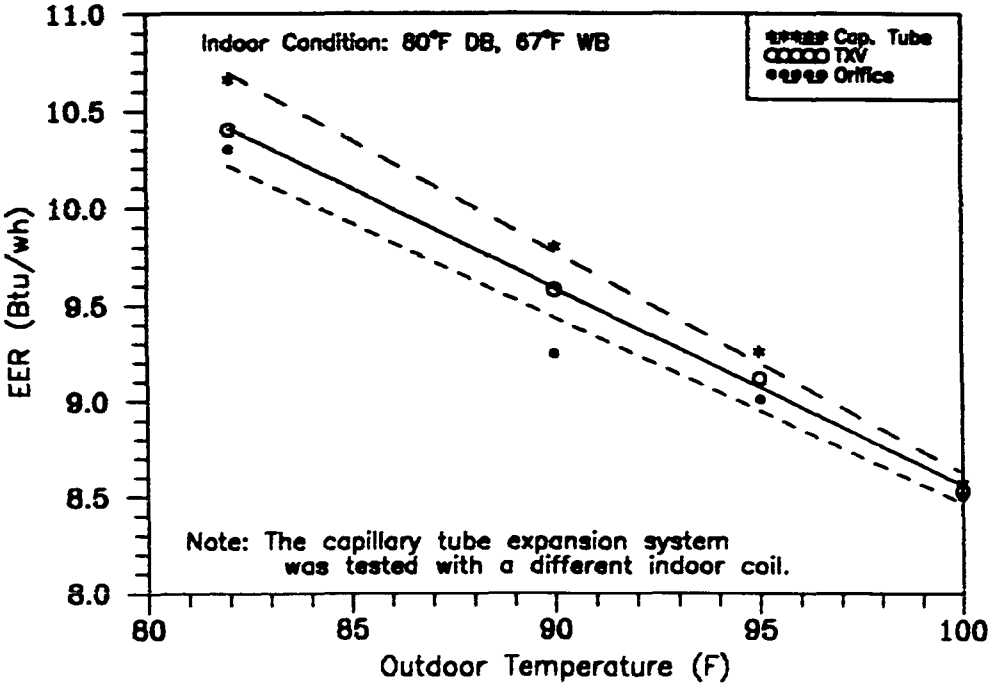

Figure 5.2 - Energy Efficiency Ratio of the Fully Charged System with Various Expansion Devices

decreased with increasing outdoor temperature. The capacity of air conditioners with the TXV and capillary tube expansion devices show a more observable dependence on the outdoor temperature than that of the unit having the short-tube orifice expansion device. The capacity of the units having the TXV and capillary tube expansion devices dropped by 10% as the outdoor temperature increased from 82°F to 100°F while the unit capacity with short-tube orifice dropped off by 6% for the same increasein temperature. The effect of outdoor temperature on the *EER* was similar for all three units. The reason for lower *EER* at higher outdoor temperature was due to higher compressor power consumption and lower unit capacity. As the condensing temperature increased due to the higher outdoor temperature, the power (kw) to the compressor increased too. Figure 5.3 shows the outdoor unit power consumption as a function of outdoor temperature for each expansion device under the fully charged condition. The power consumption for all three units increased linearly by an average of 12%, as the outdoor temperature increased from 82°F to 100°F.

STEADY STATE AND CYCLIC TESTS (Dry Coil) RESULTS

The DOE test procedure also requires testing of an air conditioner under conditions in which no water condensation would occur on the evaporator coil. Both steady state and cyclic tests were performed with indoor conditions set at 80°F DB and 57°F WB. The wet bulb temperature was sufficiently low enough so that no condensate formed on evaporator coil. The outdoor room condition was maintained at 82°F DB and 20% relative humidity during these tests.

The cooling cyclic test was conducted by cycling the compressor 6 minutes "on" and 24 minutes "off". During the "on" period, electrical energy and capacity measurements were made. According to the DOE test procedure, during the first two minutes of the "off" period, the capacity was also measured. Upon compressor start-up, the cooling capacity of an air conditioner increases to its steady state value gradually,

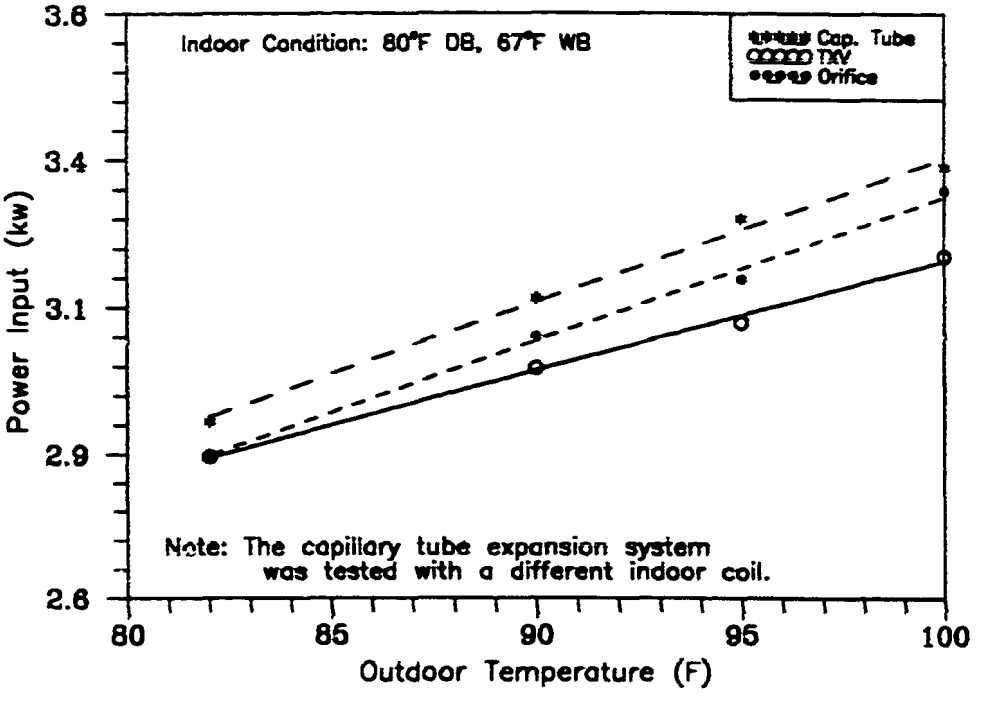

Figure 5.3 - Power Consumption of the Fully Charged System with Various Expansion Devices

rather than instantaneously. This lack of an instantaneous response leads to lower average capacities and efficiencies than the respective steady state values. The first few minutes after start-up are the most crucial for cyclic losses. The start-up losses result from off-cycle phenomena. One of the major losses is due to the refrigerant migration from the condenser to evaporator. Table 5.1 shows the unit performance for the three expansion devices under fully charged conditions for steady state and cyclic tests.

Table 5.1 - Dry Coil Steady State and Cyclic Tests Performance

Expansion Device	EER_C	EER_D	$SEER$	C_D
Cap. Tube	9.75	7.84	9.44	0.235
Orifice	9.38	8.40	9.61	0.130
TXV	9.46	8.46	9.70	0.186

The coefficient of degradation (C_D) is a measure of the efficiency loss due to the cycling of the unit. The unit with the short-tube orifice expansion device had the lowest C_D among the three expansion devices. The smaller C_D value in Table 5.1 suggested that the unit with the short-tube orifice expansion device reached steady state after start-up more rapidly than the systems with the TXV and capillary tube expansion devices. This phenomena is shown in Figure 5.4 where the normalized capacities are plotted as a function of time for the three systems. The systems with the TXV and short-tube orifice expansion devices reached 95% of its steady state capacity in 3.2 minutes. For the capillary tube system, it took 4.8 minutes to reach 95% of its steady state capacity.

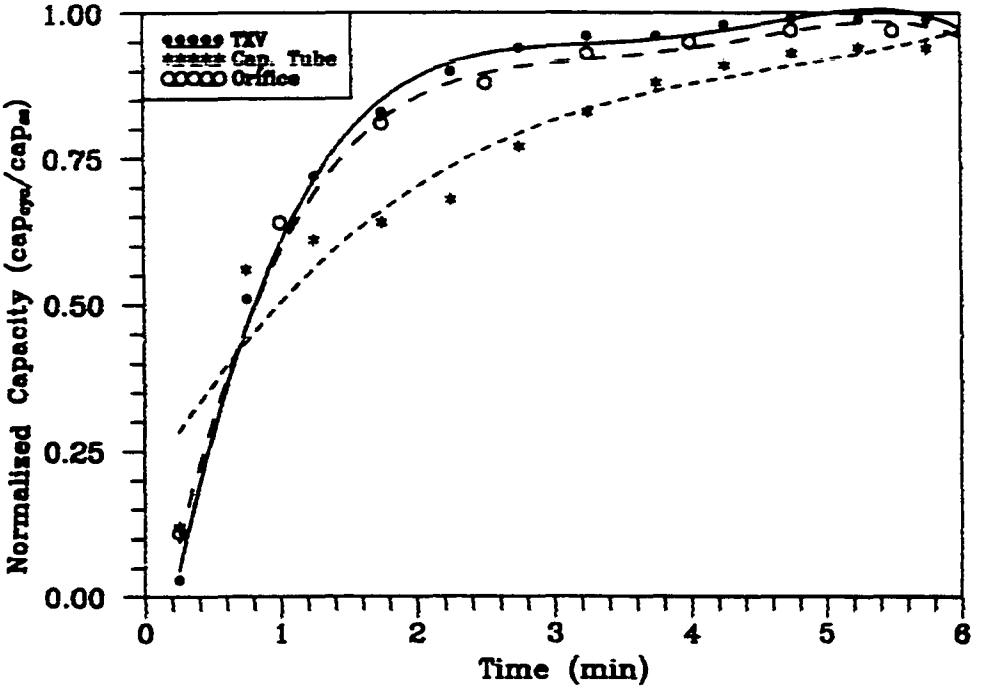

Figure 5.4 - Normalized Capacity During Startup of the Fully Charged System with Various Expansion Devices

CHAPTER VI

EXPERIMENTAL RESULTS FOR OFF-DESIGN CHARGING CONDITIONS

The amount of refrigerant charge in the system was varied to determine its effect on the performance of an air conditioner. For each charge, the air conditioner was subjected to a range of outdoor temperatures and three expansion devices. The influence of these variables on the system performance (Capacity, Power, *EER*, and *SEER*) was investigated. Once the manufacturer's full charge was determined, as described in chapter V, a set of tests was performed at that charge. The system was then evacuated of refrigerant. Refrigerant was then added in increments to cover a large range of off-design charging conditions for the particular expansion device being tested. Three expansion devices were investigated: capillary tube, TXV and short-tube orifice. The outdoor unit was subjected to four different (82°, 90°, 95° and 100°F) temperatures for each charge. The indoor conditions for the "wet" coil (evaporator condenses moisture) tests were set at 80°F DB and 67°F WB. Next, the steady state test C and cyclic test D were conducted. The indoor conditions were set at 80°F DB and 57°F WB, while the outdoor conditions were kept constant at 82°F DB and 20% RH throughout the "dry" coil (evaporator condenses no moisture) tests.

STEADY STATE WET COIL TESTS

The steady state wet coil tests were conducted at four outdoor temperatures: 82°, 90°, 95° and 100°F DB and 20% RH. The indoor conditions were set at 80°F DB and 67°F WB. These tests were repeated on the unit from 80% to 120% of full charge.

Total Capacity

The total capacity of the unit was based on the measurements on the air-side of the evaporator and was calculated using the air-enthalpy method found in ASHRAE

Standard 116-1983. The effects of charging and the outdoor temperature on the system capacity is presented for each expansion device.

Capillary Tube Expansion System

At 82°F, the system had a well defined peak in capacity at full charge (Figure 6.1). At this temperature, the drop in capacity for the low-charge was much steeper per unit of charge than for high-charge conditions. For instance, a -10% charging resulted in an 13.6% reduction in capacity. In contrast, a +10% charging produced only a 3.3% reduction in capacity. With an increase in outdoor temperature, the peak capacity occurred at a lower charge than that for 82°F. For 100°F, the peak capacity was at 133 ounces, which corresponded to a -5% charging. For high-charge conditions, the capacity of the unit decreased as the charge increased. At 95°F outdoor temperature, the total unit capacity dropped to 31 and 29.8 kBtu/hr for +10 and +20% charging, respectively.

Outdoor room temperature was another factor for decreasing the capacity during the off-design charging conditions. For +20% charging, the capacity of the unit dropped by 6.7% and 12.3% at 82°F and 95°F outdoor temperatures, respectively (Figure 6.1). The drop in total capacity (kBtu/hr) was higher for higher outdoor temperature.

One surprising result shown in Figure 6.1 was the difference in the behavior of the capacity for the low-charge conditions as compared to the full or high-charge case. Normally, the capacity of an air conditioner is expected to decrease as the outdoor temperature increases. However, for the low-charge tests, the capacity increased as the outdoor temperature increased.

One possible explanation for this behavior for the low-charge condition might be found in the control of the refrigerant flow rate by the capillary tubes for different charges. Liquid refrigerant enters the capillary tube, and as it flows through the tube, the pressure drops because of friction and acceleration of the refrigerant. Some of the liquid

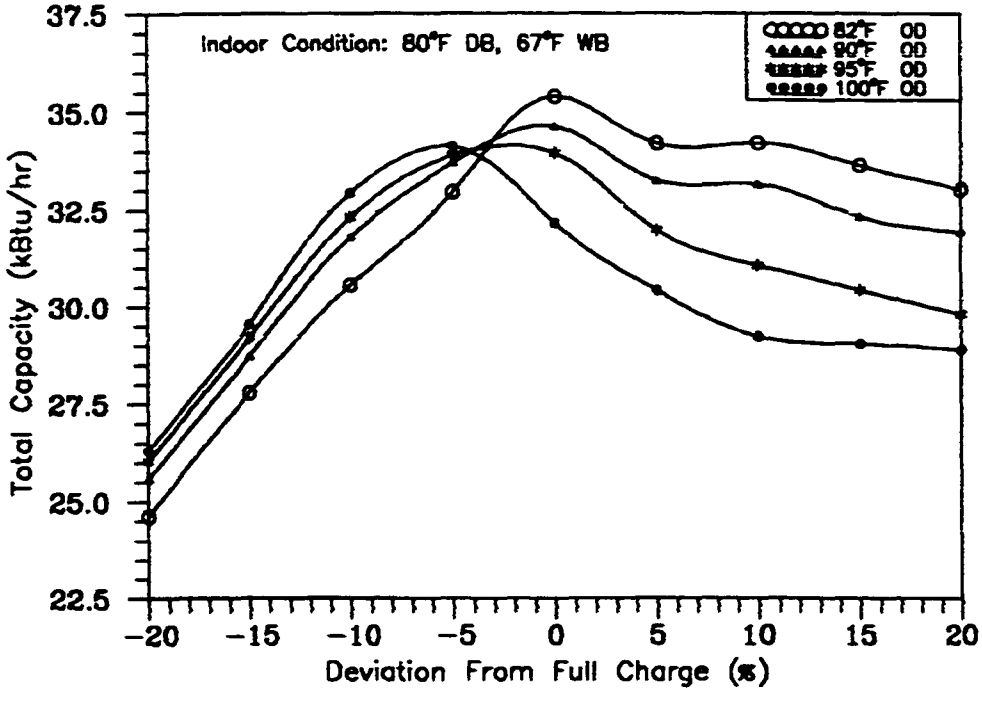

Figure 6.1 - The Capillary Tube System Total Capacity for Various Outdoor Temperatures and Charging Conditions

flashes into vapor as the refrigerant flows through the tube. Once the capillary tube was selected and installed in a unit, the tube is fixed in the adjustments it can make to variations in discharge pressure, suction pressure, load, or amount of charge in the system. Figure 6.2 shows such a generic plot of the flow through the capillary tube as a function of condensing and evaporating temperatures. At high condensing pressures the capillary tube feeds more refrigerant to the evaporator than it does at low condensing pressure, because of the increase in pressure difference across the capillary tube.

As the outdoor temperature increased, the pressure drop across the capillary tube increased (Figure 6.3). As the pressure drop increased, the capillary tube fed more refrigerant to the evaporator. Also, at the higher outdoor temperatures, the suction pressure increased slightly while the suction temperature decreased (Figures 6.4 and 6.5). A decrease in suction temperature due to the higher pressure drop across the capillary tube would result in lower superheat temperature. Thus, the higher refrigerant flow rate is the reason for higher capacity at higher outdoor temperatures for the conditions of low-charge. The refrigerant flow rate as a function of condenser pressure and charge is given in Figure 6.6. For the -20% charging tests, the refrigerant flow rate increased by 13.5% when the outdoor room temperature increased from 82°F to 100°F. A 13.5% increase in refrigerant flow resulted in a 5.7% increase in total capacity of the unit. However, for the same increase in outdoor room temperature, the refrigerant flow rate only increased by 3.7% and 2.6% for the +10 and +20 percent charging conditions, respectively. The effect of outdoor temperature and off-design charging conditions on the refrigerant flow rate is shown in Figure 6.7.

The measured refrigerant flow rates shown in Figure 6.6 showed a similar trend to the calculated flow rates from the ASHRAE handbook of equipment. According to the ASHRAE handbook, refrigerant mass flow rate is calculated as follows:

$$MFR = k\,Q$$

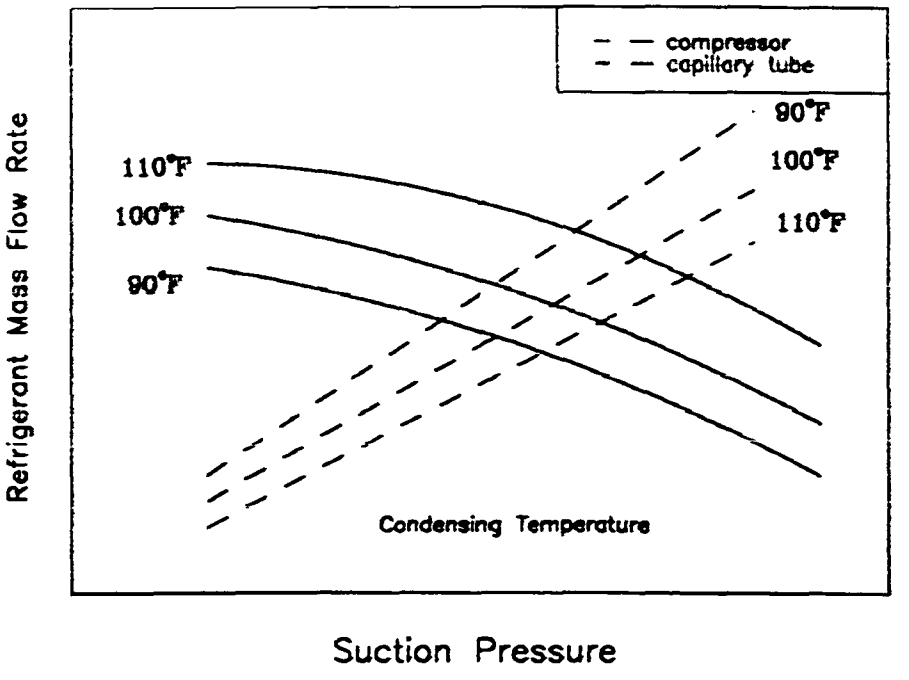

Figure 6.2 - Generic Balance Points for a Unit with Capillary Tube

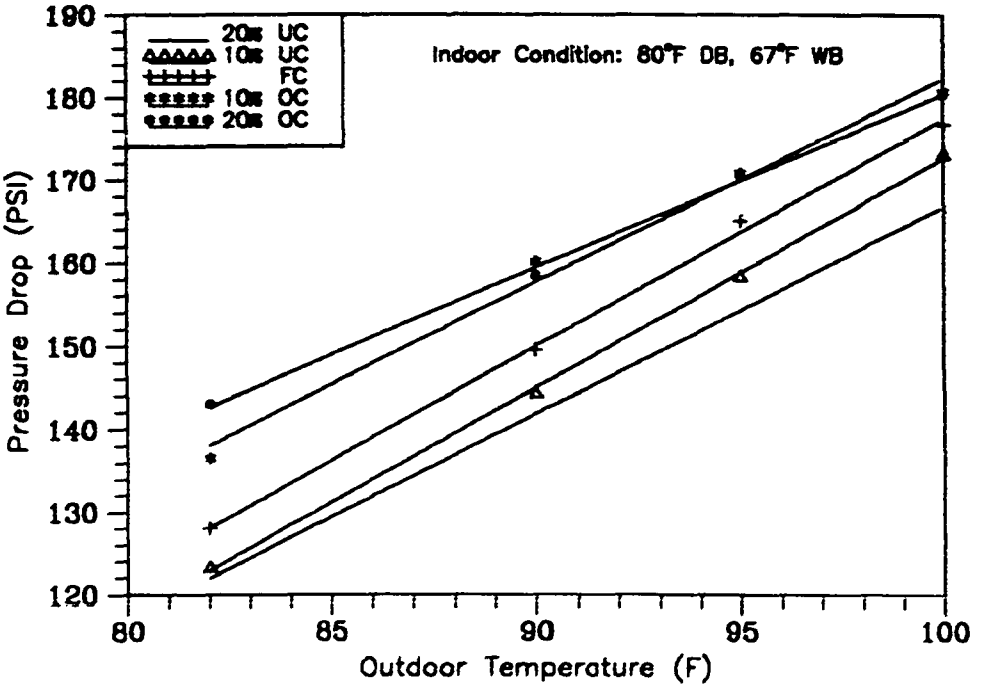

Figure 6.3 - Pressure Drop Across the Capillary Tube for Various Outdoor Temperatures and Charging Conditions

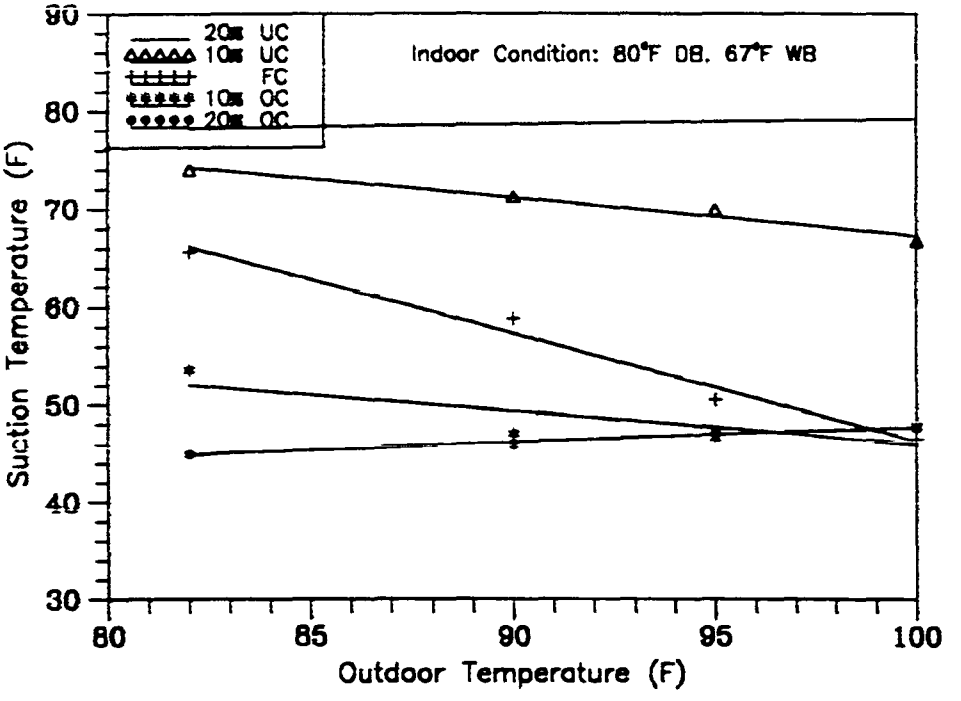

Figure 6.4 - The Capillary Tube System Suction Temperature for Various Outdoor Temperatures and Charging Conditions

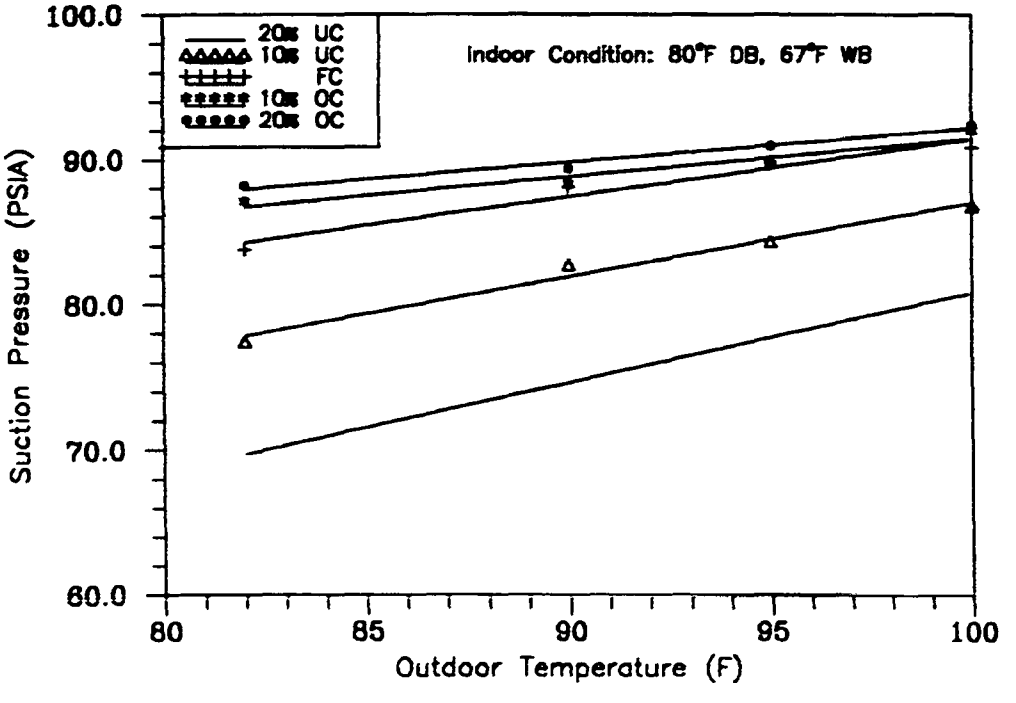

Figure 6.5 - The Capillary Tube System Suction Pressure for Various Outdoor Temperatures and Charging Conditions

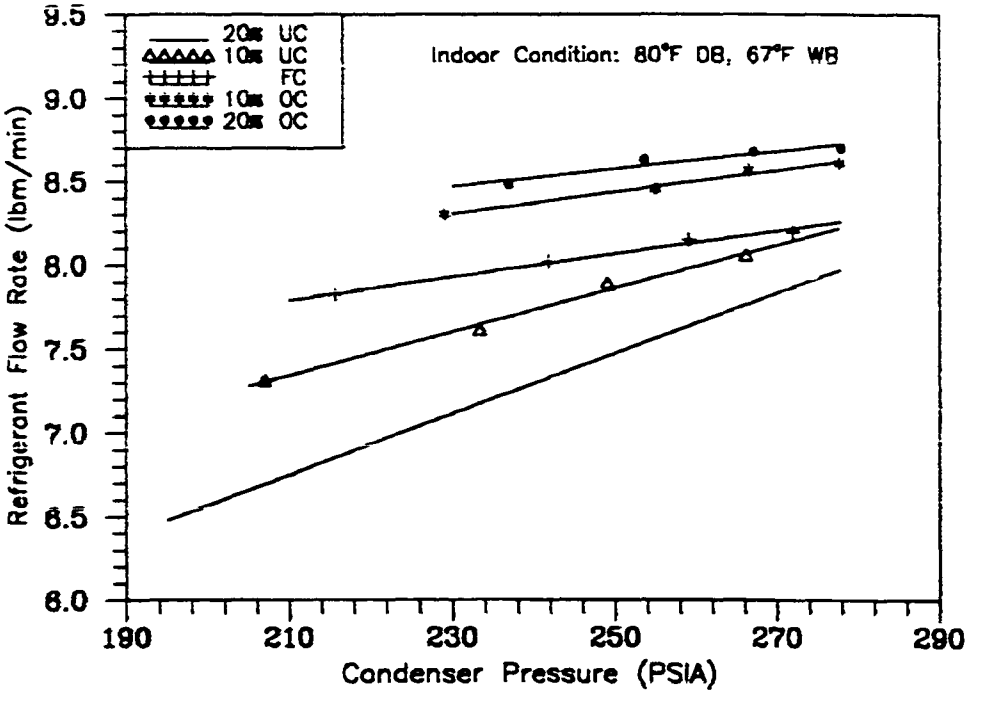

Figure 6.6 - The Capillary Tube System Measured Refrigerant Flow Rate for Various Condenser Pressures and Charging Conditions

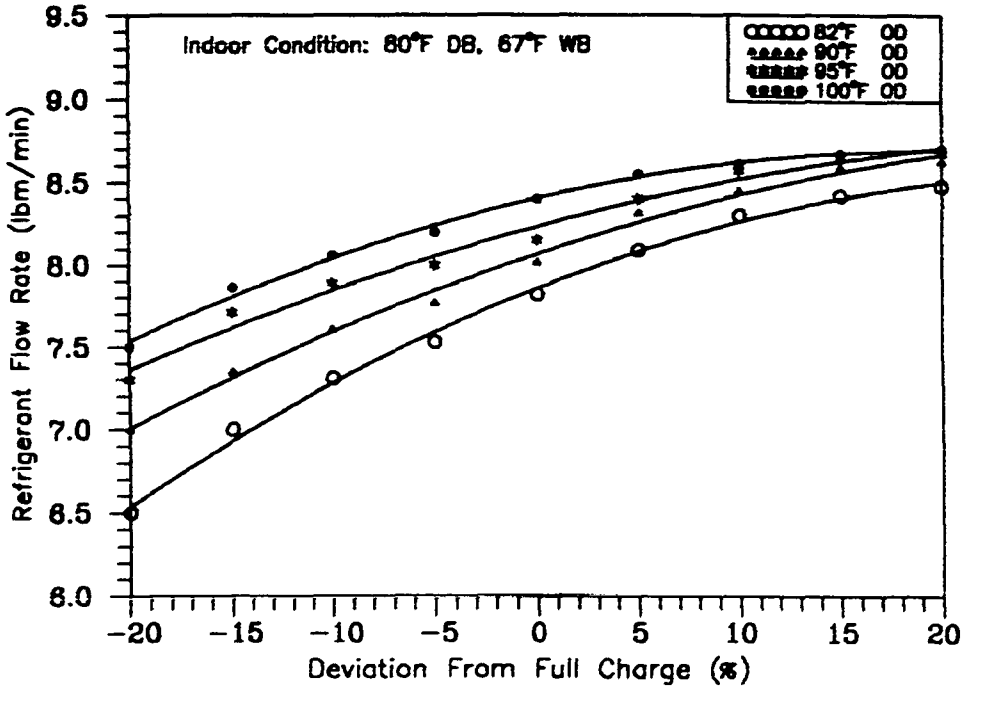

Figure 6.7 - The Capillary Tube System Measured Refrigerant Flow Rate for Various Outdoor Temperatures and Charging Conditions

where,

MFR = actual mass flow rate of refrigerant
k = flow factor
Q = standard mass flow rate

The flow factor and standard mass flow rate of refrigerant curves are obtained from the ASHRAE Handbook of Equipment. The standard mass flow rate is directly proportional to the subcooling temperature and condenser pressure. For the test condenser pressures and subcooling temperatures, the refrigerant mass flow rate was calculated and is shown in Figure 6.8. For the -20 and -10 percent charging tests, the refrigerant flow rate increased by 18% when the outdoor temperature increased from 82°F to 100°F. However, for the same increase in outdoor temperature, the refrigerant flow rate increased by 5.7% and 1.6% for the +10 and +20% charging tests, respectively. The similarities between the calculated and experimental refrigerant flow rates in the capillary tube indicate that the refrigerant flow rate was more sensitive to the outdoor temperature for low-charging tests than high-charging conditions.

Thermal Expansion Valve System

Once the full charge was determined , the unit was vacuumed and recharged initially to -40% charging condition (84 oz). Figure 6.9 shows the unit total cooling capacity as a function of the outdoor temperature and the refrigerant charge. The highest capacity was obtained at 82°F outdoor temperature and -10% charging. The capacity was nearly constant from -15% to +5% charging for the four outdoor temperatures. From -15% to +5% charging conditions, the capacity of the unit dropped off by an average of 10% as the outdoor room temperature increased from 82°F to 100°F. At 95°F outdoor temperature, the total capacity was 24, 27.9, and 29.1 kBtu/hr for -40%, -30%, and -20% charging, respectively.

A thermal expansion valve (TXV) regulates the rate of flow of liquid refrigerant to produce a specified superheat at the outlet of the evaporator. A TXV responds to: (i)

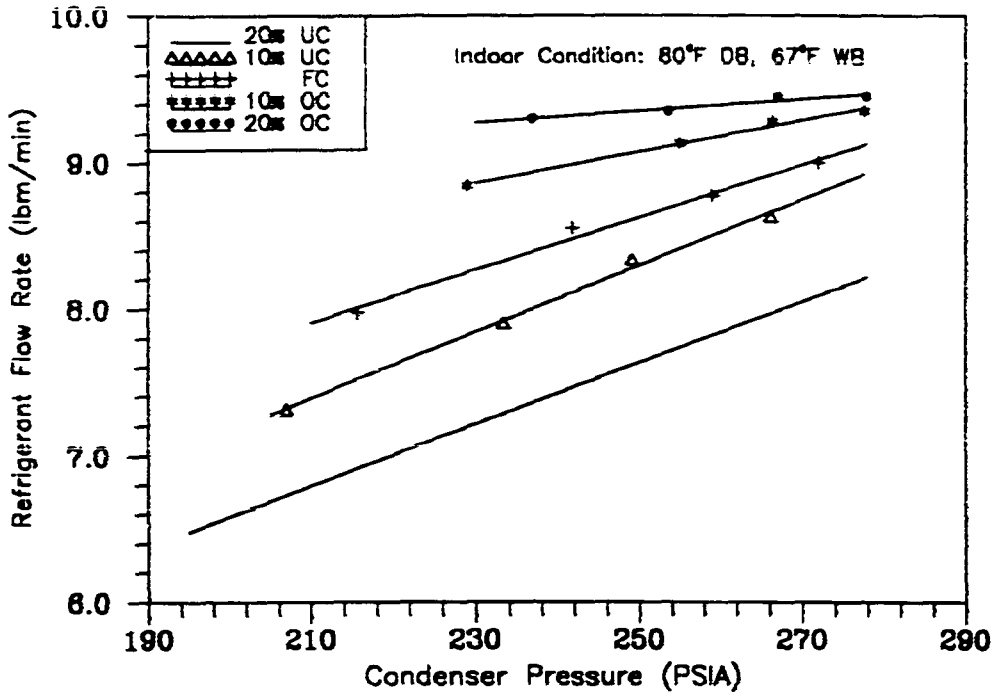

Figure 6.8 - The Capillary Tube System Calculated Refrigerant Flow Rate for Various Outdoor Temperatures and Charging Conditions

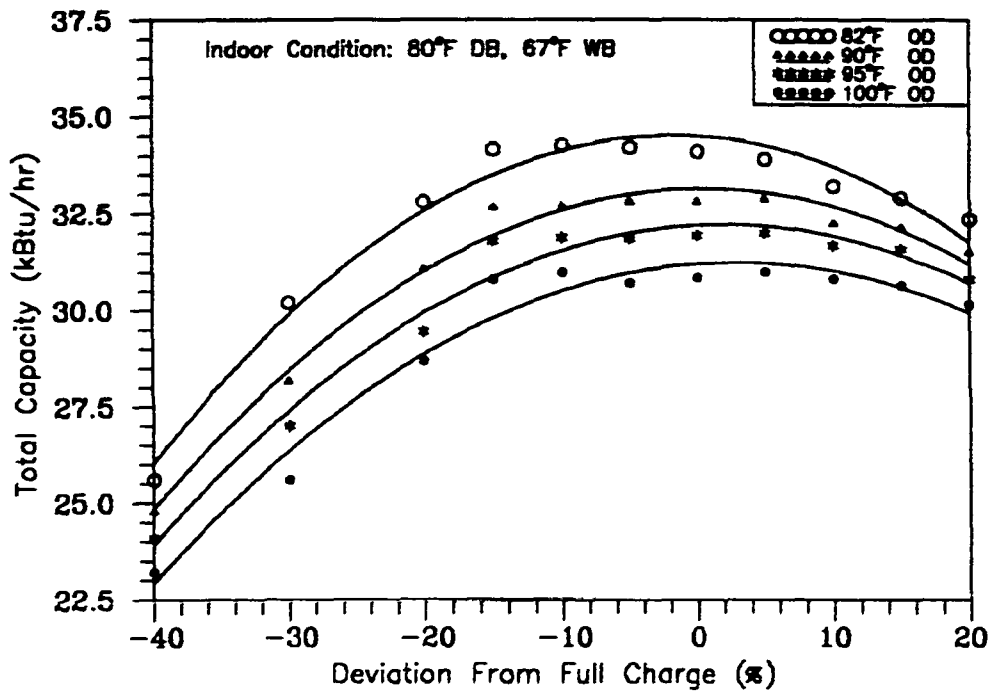

Figure 6.9 - The TXV System Total Capacity for Various Outdoor Temperatures and Charging Conditions

the temperature of the refrigerant gas leaving the evaporator, (ii) the pressure in the evaporator and (iii) subcooling temperature. As the temperature of the refrigerant increases, the pressure in the remote bulb also increases and causes the valve to open more. As the outdoor temperature increases, the superheat temperature should decrease for a given charge. Higher outdoor temperatures should also increase the condenser pressure. For lower superheat, the TXV constrained the refrigerant flow rate. Figure 6.10 shows the refrigerant flow rate as a function of TXV inlet pressure for different charge. From -15% to +20% charging conditions, the refrigerant flow rate dropped from an average of 7.7 to 7.5 lbs/min when the outdoor temperature increased from 82°F to 100°F. At any given outdoor temperature, the refrigerant flow rate was relatively constant as the charge in the system increased. The largest increase in refrigerant flow rate was the increase in charge from -20% to -10% charging conditions. The refrigerant flow rate increased by 7% at 95°F outdoor temperature.

The results from Figure 6.10 indicated that the refrigerant flow rate was similar for all the charging tests except for -40%, -30%, and -20% charging. The similar flow rates would explain why the capacities remained relatively constant from -15% charging to +10% charging and why they dropped for -20%, -30%, and -40% charged conditions.

Short-Tube Orifice Expansion System

The unit with the short-tube orifice expansion device was subjected to +/-20%, +/-10%, +/-5% charging, and fully charged conditions for 82°F and 95°F outdoor temperatures. The system was also tested for -10% charging, full charge, and +10% charging for 90°F and 100°F outdoor temperatures. The capacity data (Figure 6.11) had more scatter than the capacity data for the capillary tube and TXV expansion systems in Figures 6.1 and 6.9. The capacity dropped as the charge decreased from full charge. The capacity showed a peak that was dependent on the outdoor temperature. It also appeared to peak between +10 and +20% charge for 82°F, between +5% and +10%

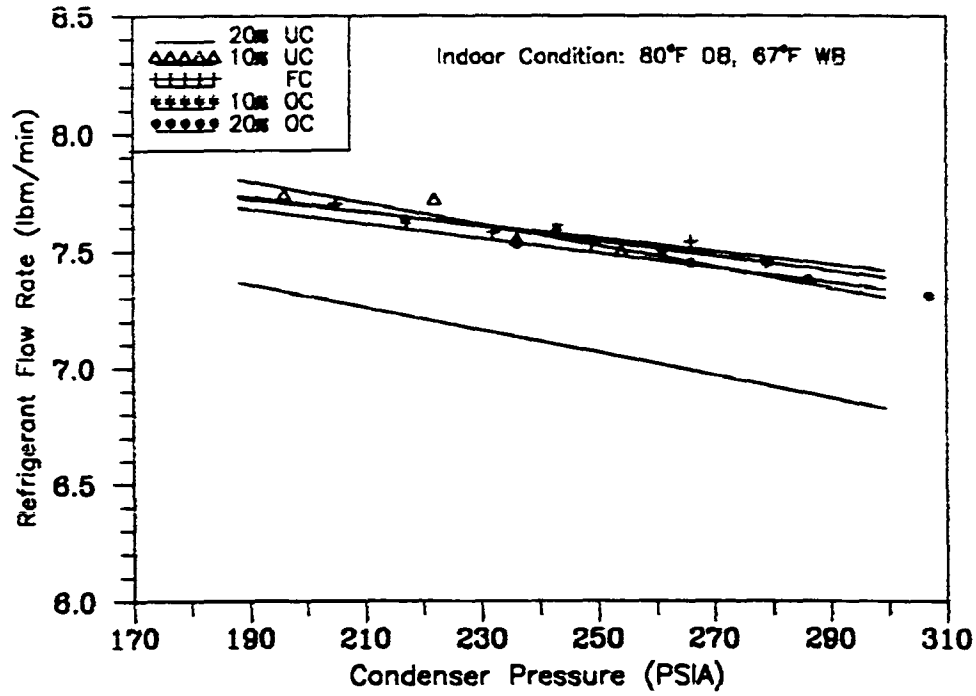

Figure 6.10 - The TXV System Refrigerant Flow Rate for Various Outdoor Temperatures and Charging Conditions

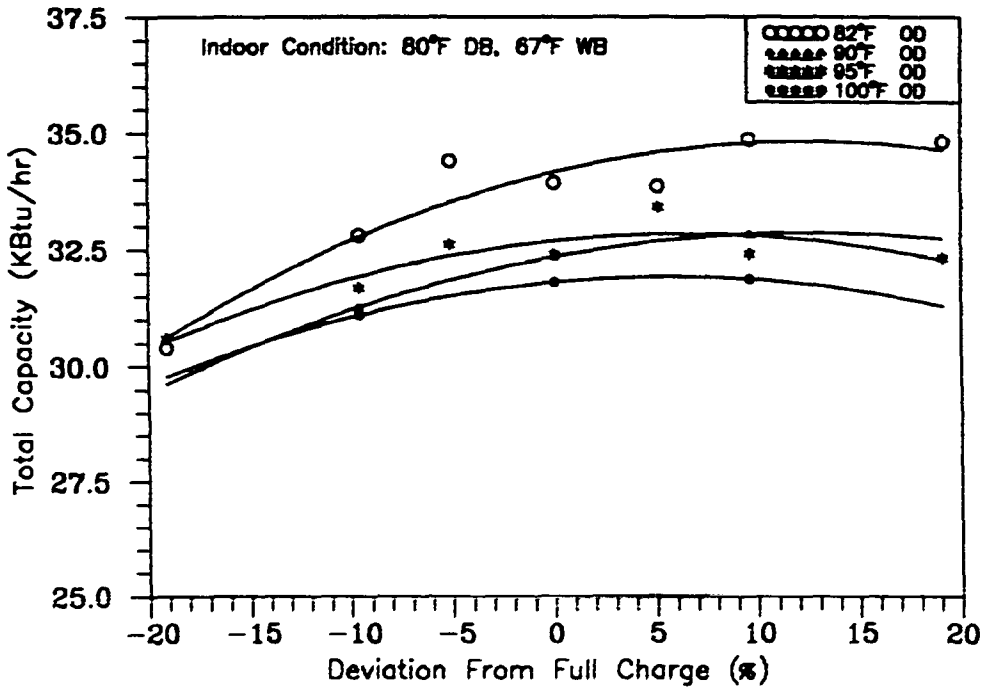

Figure 6.11 - The Short-Tube Orifice System Total Capacity for Various Outdoor Temperatures and Charging Conditions

charge for 95°F, and at approximately +5% charge for 100°F. As shown in Figure 6.11, the effects of outdoor temperature was much more noticeable in high-charging than low-charging conditions. For -10% charging, the capacity dropped from 32.7 to 30.5 kBtu/hr when the outdoor temperature increased from 82°F to 100°F. For the same increase in outdoor temperature, the capacity dropped from 34.7 to 31 kBtu/hr for +10% charging condition.

Power and Energy Efficiency Ratio (*EER*)

EER is a calculated by dividing the net total cooling capacity in Btu/hr by the power input in watts (w) at any given set of rating conditions, expressed in Btu/wh. The effects of charging on the system outdoor unit power consumption and *EER* is presented for each expansion device.

Capillary Tube Expansion System

Figure 6.12 shows the *EER* as a function of outdoor temperature and refrigerant charge. As the outdoor temperature increased, *EER* decreased for a given charge. The maximum *EER* occurred at 82°F outdoor temperature for the fully charged condition. As the outdoor temperature increased, the peak of the curves shifted to the left (lower charge). For instance, the *EER* curves for 95°F, and 100°F outdoor temperatures were maximum at -5% charging rather than full charge. At 95°F, and 100°F outdoor temperatures, the fully charged *EER* actually dropped by 1.4% and 6.4%, respectively. The drop in *EER* was more noticeable for the low-charge conditions than high-charge conditions at an outdoor room temperature of 82°F. The *EER* dropped to 8.3 for -20% charging and 9.23 for +20% charging tests. The reason for lower *EER*s at higher outdoor temperature was due to higher compressor power consumption and lower unit capacity. The increase in power (kw) was due to the higher condensing temperature of the unit. The condenser outlet temperature decreased as the refrigerant charge in the system increased for a given outdoor temperature. This drop was due to the increase in the

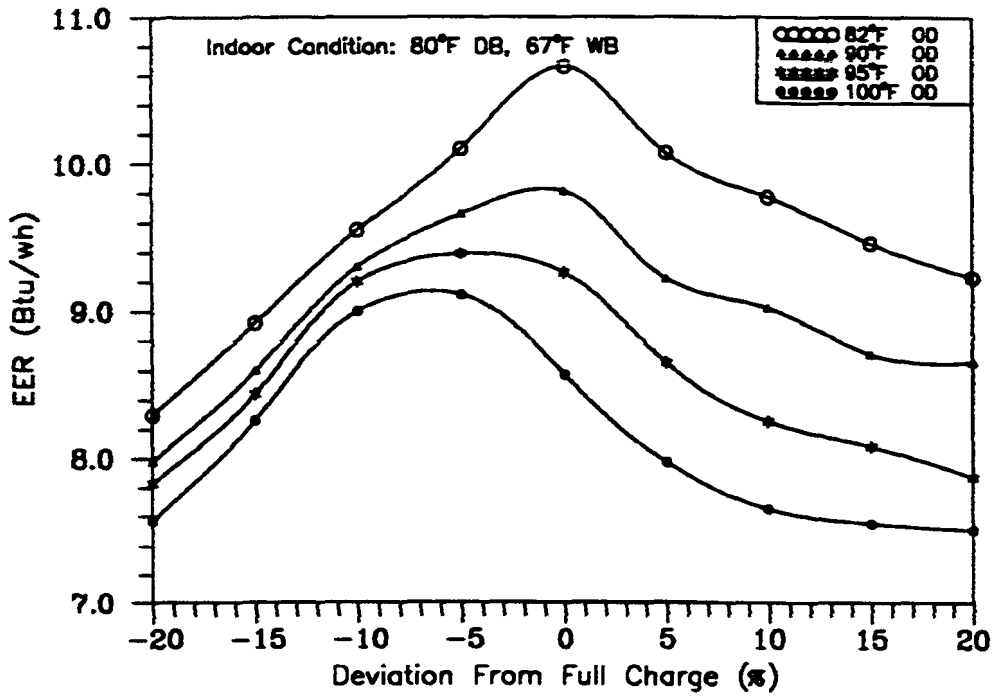

Figure 6.12 - The Capillary Tube System *EER* for Various Outdoor Temperatures and Charging Conditions

subcooled temperature. As the condensing temperature increased, the power (kw) to the compressor increased (Figure 6.13) too. For -20% charging, the power (kw) increased by 19.6% when the outdoor room temperature increased from 82°F to 100°F. However, for the same increase in outdoor room temperature, the power increased by 8.5% for +20% charging condition.

Thermal Expansion Valve System

Figure 6.14 shows the *EER* as a function of outdoor room temperature and refrigerant charge. As the outdoor temperature increased, *EER* decreased for a given charge. The maximum *EER* occurred at 82°F outdoor room temperature for the -15%, -10%, and -5% charging conditions. The *EER* curves were approximately constant from -15% to +5% charging conditions, as the outdoor temperature increased. For instance, the *EER* curves for 95°F outdoor temperature varied from 9.26 to 9.11 over the range of -15% to +5% charging conditions. For the full charge, *EER* dropped by 22% when the outdoor temperature increased from 82°F to 100°F. The drop in *EER* was more noticeable for the -40%, -30%, and -20% charging than high-charge conditions at the four outdoor temperatures. The reason for lower *EER* at higher outdoor temperatures was due to higher compressor power consumption and lower unit capacity. The increase in power (kw) was due to the higher condensing temperature of the unit. The condenser outlet temperature decreased as the refrigerant charge in the system increased. This drop was due to the increase in the subcooling. As the condensing temperature increased, the power (kw) to the compressor increased too.

Figure 6.15 shows the power consumption of the outdoor unit as a function of outdoor temperature and charge. For the fully charged condition, the power (kw) increased by 12% when the outdoor temperature increased from 82°F to 100°F. However, for the same increase in outdoor room temperature, the power increased by 12.5% for -/+20% charging tests. As the charge in the unit increased, the power (kw)

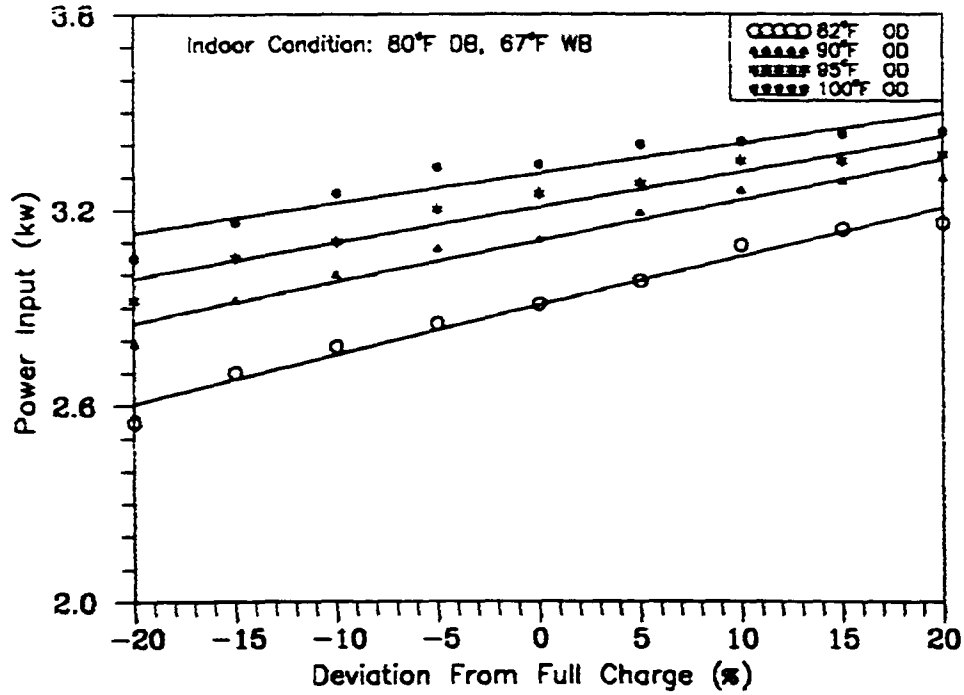

Figure 6.13 - The Capillary Tube System Power Consumption for Various Outdoor Temperatures and Charging Conditions

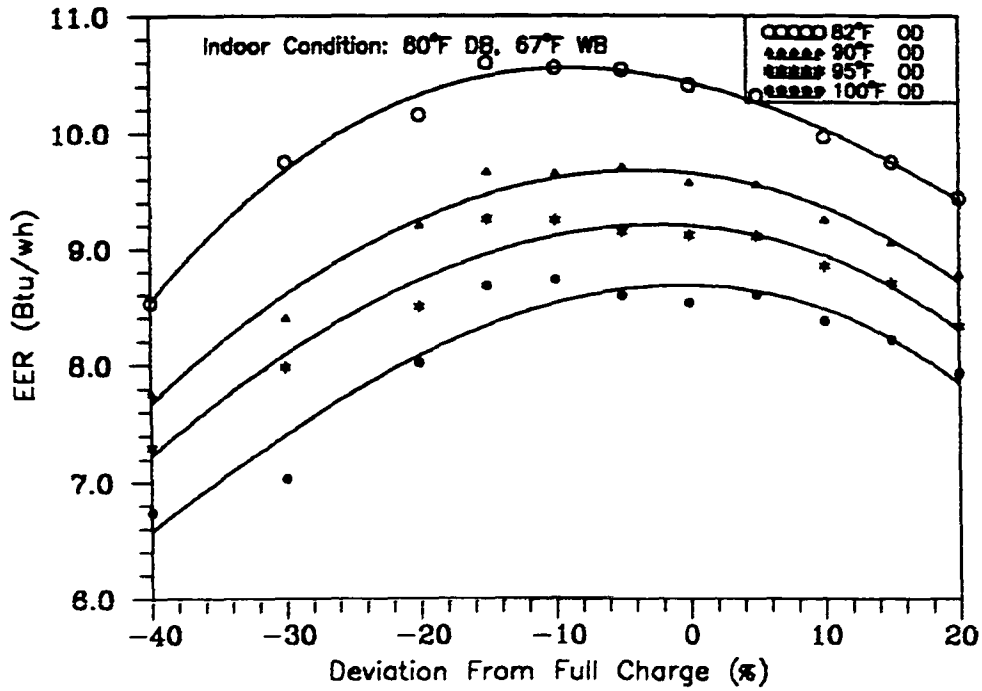

Figure 6.14 - The TXV System *EER* for Various Outdoor Temperatures and Charging Conditions

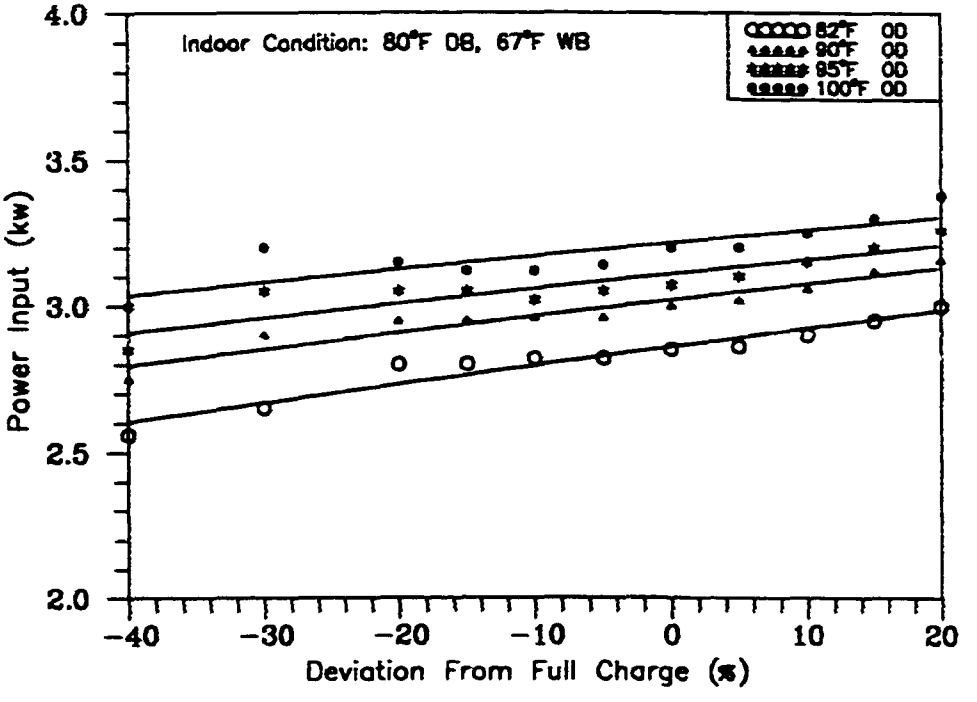

Figure 6.15 - The TXV System Power Consumption for Various Outdoor Temperatures and Charging Conditions

increased linearly. At 82°F outdoor temperature, the power (kw) increased by 5% when the unit's charge was increased from -20% to +20% charging.

Short-Tube Orifice Expansion System

The *EER* showed a strong dependence on outdoor temperature, but varied little with charge (Figure 6.16). For instance, at 95°F, the *EER* varied from 9.1 at -20% charging to 8.6 at +20% charging. This behavior contrasts quite dramatically with the behavior of the capillary tube expansion system. At full charge, the *EER* dropped from 10.2 to 8.6 when the outdoor temperature increased from 82°F to 100°F. As shown in Figure 6.16, the *EER* decreased slightly as the charge increased. The reason for this behavior is due to the slight increase of unit power consumption as a function of charge (Figure 6.17). The outdoor unit power consumption increased as the outdoor temperature increased but it varied little with charge. The reason for the small increase in the unit power consumption was due to the small increase in refrigerant flow rate handled by the compressor as a function of charge. The refrigerant flow rate as a function of charge and outdoor temperature is shown in Figure 6.18. The refrigerant flow rate increased slightly as the charge in the system increased but it showed a strong dependence on the outdoor temperature.

System Subcooling and Superheat Temperatures

The subcooling temperature is the difference between the refrigerant temperature and the refrigerant saturation temperature at the condenser exit. The subcooled temperature was used to determine the full charge for the TXV expansion system. Subcooling of the liquid refrigerant increases the capacity of the system and decreases the amount of vapor produced in the expansion device during the expansion process. Higher subcooling temperatures can be obtained by two options: (i) increasing the heat transfer from the condenser or (ii) increasing the refrigerant charge in the system. Increasing the heat transfer is usually accomplished by the addition of or improvement of

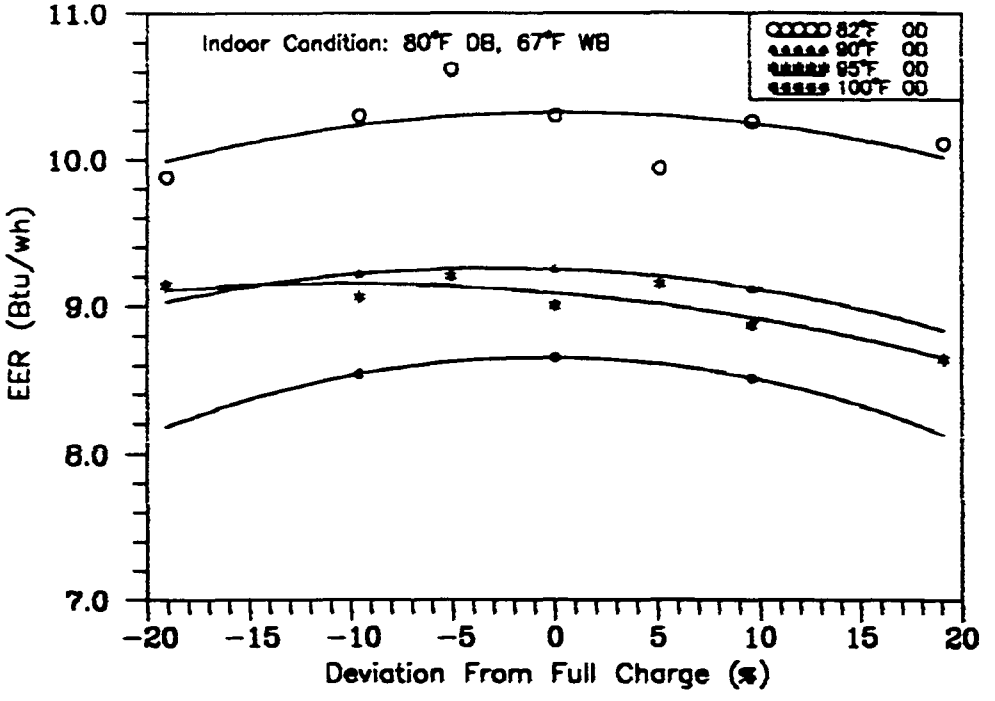

Figure 6.16 - The Short-Tube Orifice System *EER* for Various Outdoor Temperatures and Charging Conditions

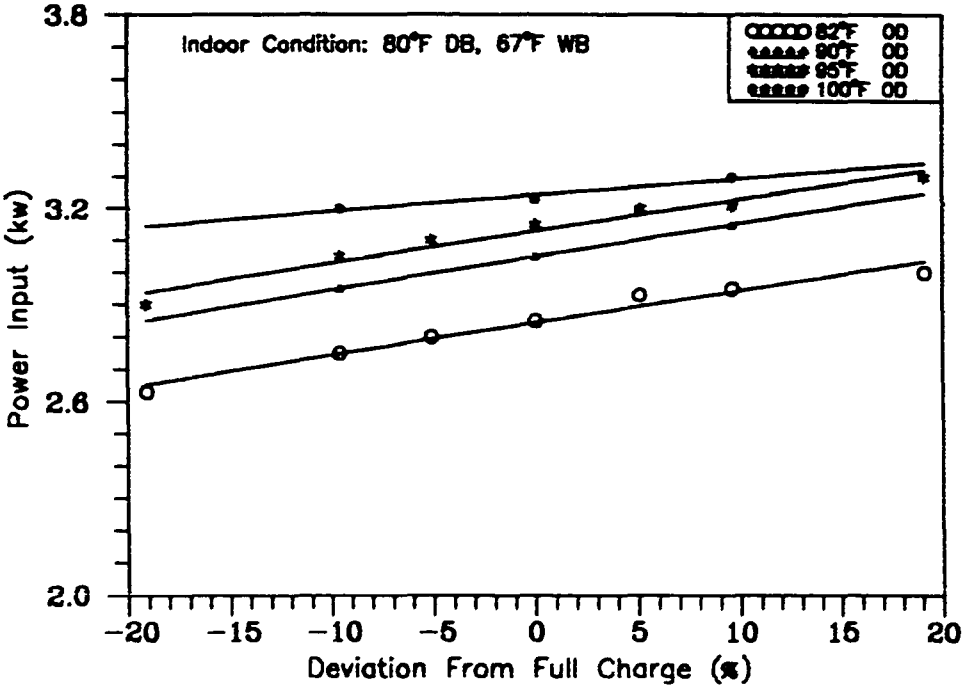

Figure 6.17 - The Short-Tube Orifice System Power Consumption for Various Outdoor Temperatures and Charging Conditions

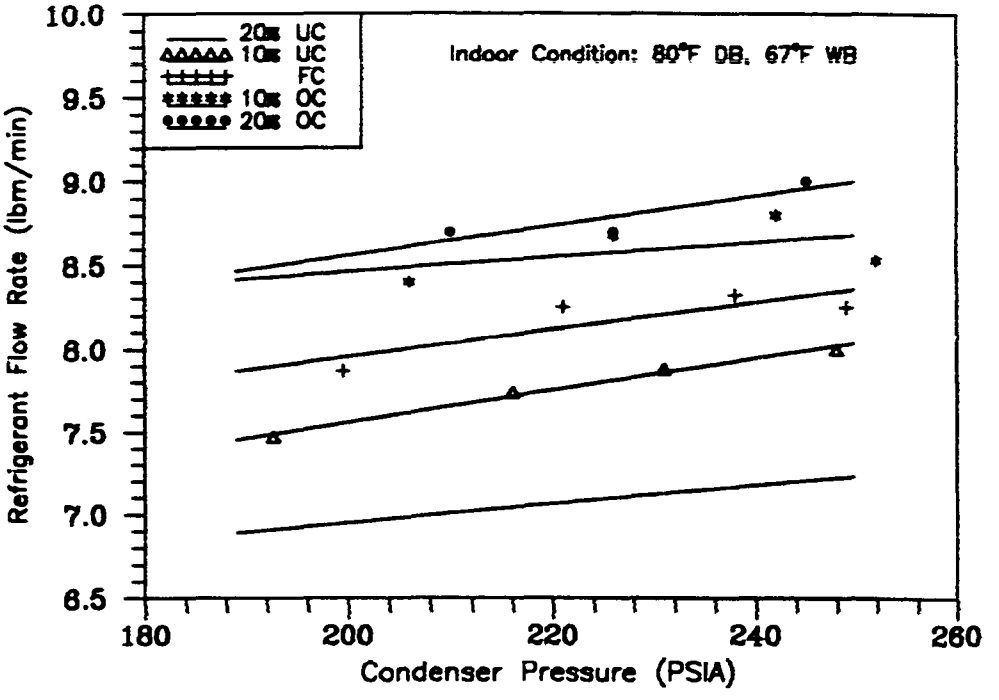

Figure 6.18 - The Short-Tube Orifice System Refrigerant Flow Rate for Various Outdoor Temperatures and Charging Conditions

the heat exchanger surface area which increases the cost of the system and can produce high pressure drops. The disadvantage of increasing the system refrigerant charge is a possible introduction of wet vapor (no superheat) into the compressor. Thus, from the design standpoint, an optimum subcooling is desired for manufacturers.

The superheat temperature is the difference between the refrigerant temperature and the refrigerant saturation temperature at the evaporator exit. The superheat temperature was used to determine the full charge for the capillary tube and short-tube orifice expansion systems. The capacity of the refrigeration system is increased when the refrigerant is superheated. Two additional advantages for superheating are: (i) superheating assures complete evaporation of liquid refrigerant before it enters the compressor and (ii) for the TXV, variations in superheat temperature serves as a means of modulating the size of the opening of the expansion device. On the other hand the refrigerating capacity is decreased when the refrigerant density is deceased during superheating. Thus, for a best unit performance, an optimum superheat temperature is desired.

Capillary Tube Expansion System

For different outdoor temperatures, the subcooling was constant at 10°F and 14.5°F for -20% and -10% charging conditions, respectively. As shown in Figure 6.19, the subcooled temperature dropped for high-charge conditions when the outdoor room temperature increased from 82°F to 100°F. For instance, the subcooled temperature dropped from 26.5°F to 19.6°F for +20% charging conditions.

As the amount of refrigerant in the system increased, the superheat at the exit of the evaporator reduced and reached saturation (Figure 6.20) for the high-charge conditions. The superheat at the outlet of the evaporator decreased as the outdoor temperature increased. For +10%, +15%, and +20% charging, the refrigerant at the

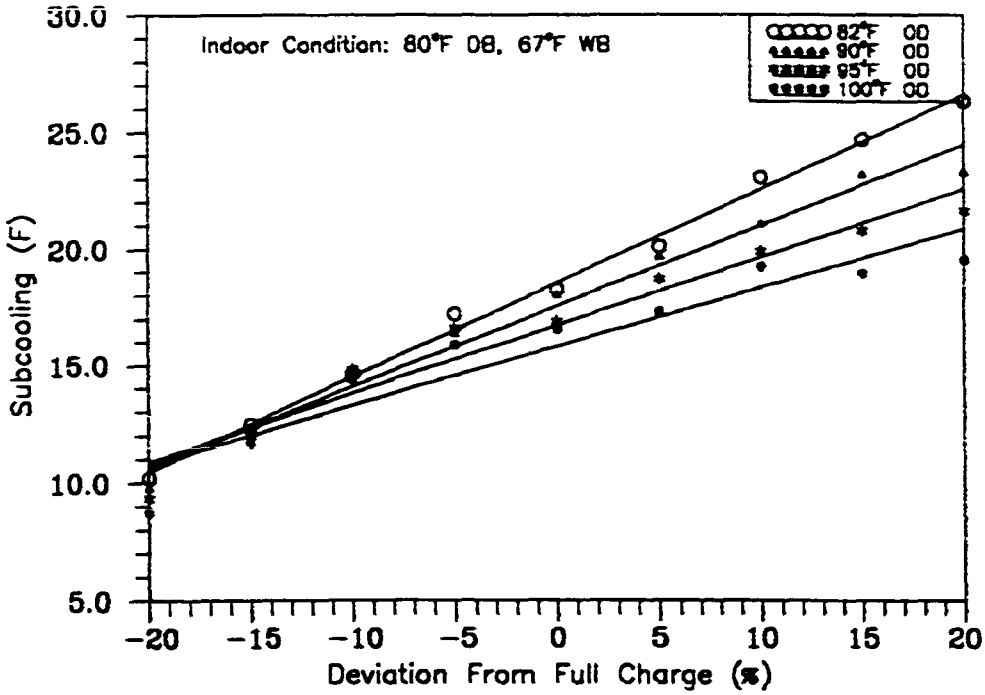

Figure 6.19 - The Capillary Tube System Subcooling for Various Outdoor Temperatures and Charging Conditions

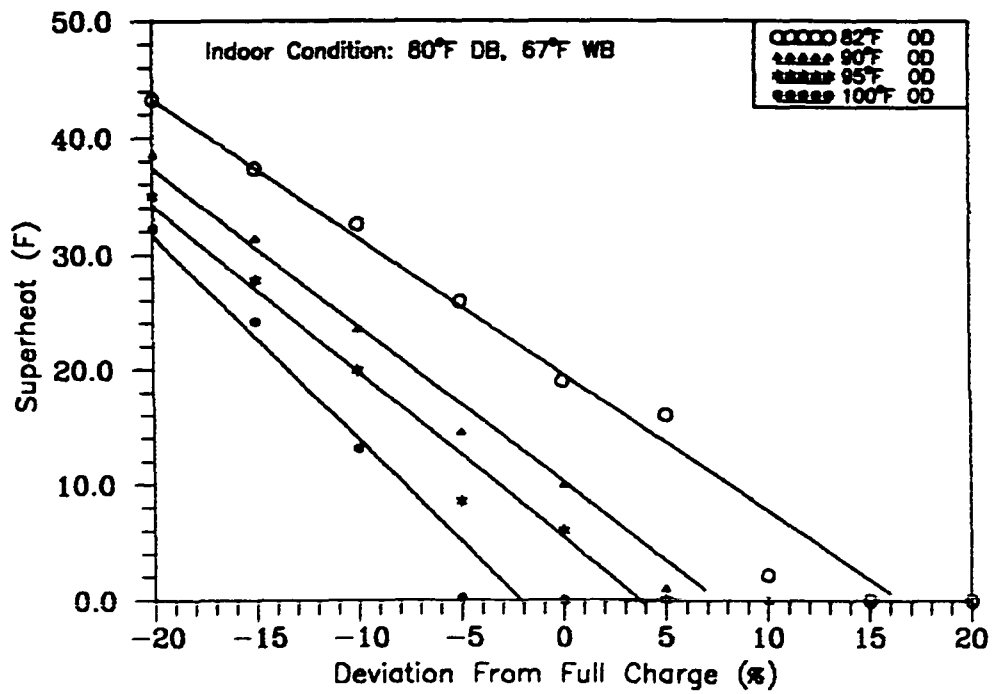

Figure 6.20 - The Capillary Tube System Superheat for Various Outdoor Temperatures and Charging Conditions

outlet of the evaporator was saturated. The saturated conditions at the evaporator outlet would indicate possible introduction of wet vapor into the compressor.

Thermal Expansion Device System

For -40%, -30%, -20%, and -15% charging, the refrigerant at the inlet of the TXV was saturated (no subcooling). This subcooling increased slightly as the outdoor temperature increased when the refrigerant charge in the system increased from -10% to +20% charging conditions (Figure 6.21).

At 95°F, the subcooling temperature was constant at less than 1°F for -40%, -30%, and -20% charging. The less than 1°F subcooling for -40% to -20% charging probably corresponded to saturated conditions. This small subcooling could be due to the error associated with the refrigerant temperature and pressure probes.

The superheat temperature decreased as the outdoor temperature increased. As the charge in the system increased, the superheat decreased slightly (Figure 6.22). The superheat temperature dropped from an average of 17.5°F to an average of 16°F when the outdoor temperature increased from 82°F to 100°F for a charge condition. A TXV should provide relatively constant superheat over the outdoor temperature tested in this study. The results from Figure 6.22 indicated that this TXV was able to maintain a relatively constant superheat for the range in outdoor temperatures tested from -20% to +20% charging conditions.

Short-Tube Orifice Expansion System

Subcooling increased with increasing charge for all the outdoor temperatures (Figure 6.23). For 95°F outdoor temperature, the subcooling increased from 1°F at -20% charging to 12.5°F at +20% charging condition. For the same range in charge, the pressure at the short-tube orifice inlet increased from 228 psia to 245 psia. Thus, with both pressure and subcooling increasing, the flow rate increases.

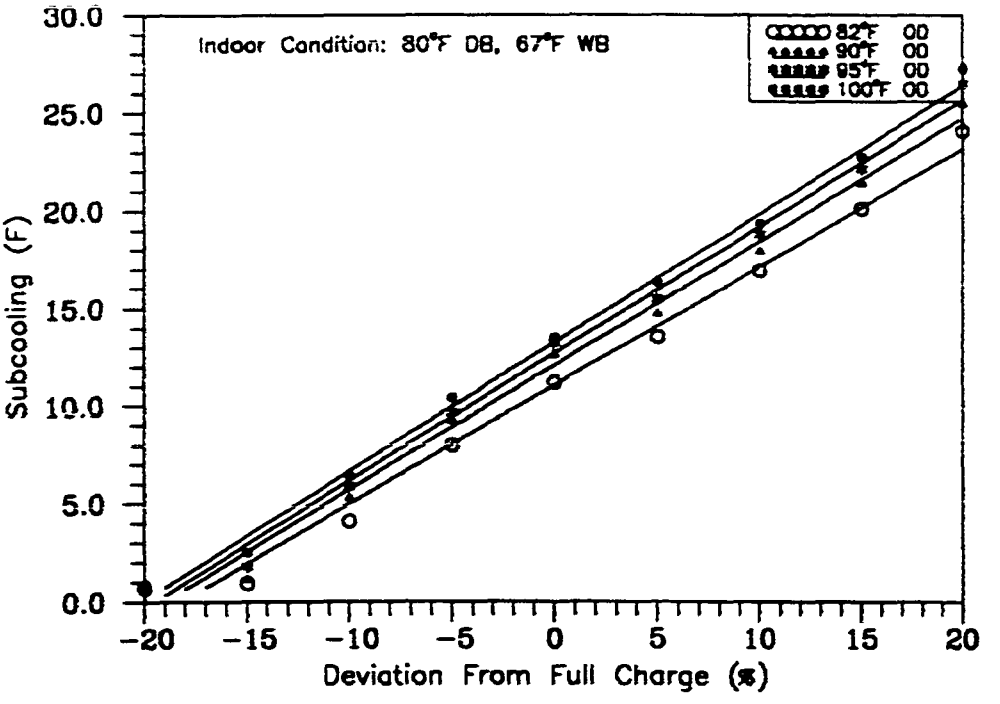

Figure 6.21 - The TXV System Subcooling for Various Outdoor Temperatures and Charging Conditions

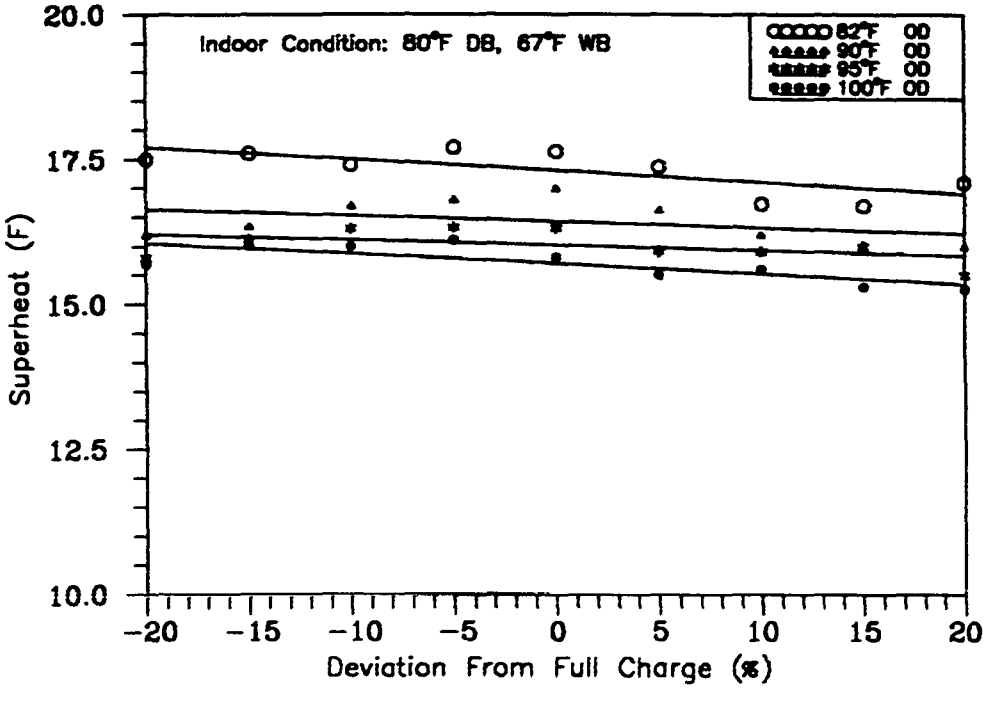

Figure 6.22 - The TXV System Superheat for Various Outdoor Temperatures and Charging Conditions

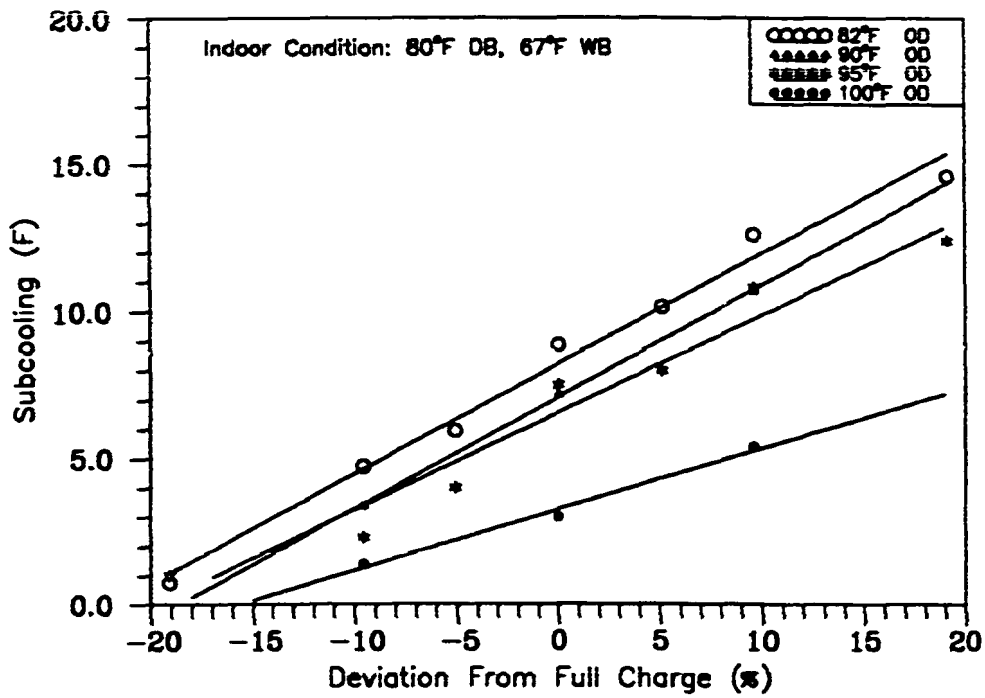

Figure 6.23 - The Short-Tube Orifice System Subcooling for Various Outdoor Temperatures and Charging Conditions

The superheat near the compressor disconnect was extremely sensitive to the charge (Figure 6.24). At full charge the superheat was 8°F for 95°F outdoor dry bulb temperature. A drop in charge of 5% (7 ounces) increased the superheat to 19°F. The superheat dropped 3°F at +10% charging and remained at 3°F for +20% charging. For +10% charging and greater, the refrigerant was superheated at the outlet of the evaporator. Thus, the 3°F superheat reflects the pressure drop between the evaporator outlet and the location where superheat was measured near the compressor inlet.

Sensible Heat Ratio (SHR)

The sensible heat ratio is defined as the ratio of the sensible capacity to the total capacity of the unit.

Capillary Tube Expansion System

The SHR increased as the amount of the charge in the system increased systematically (Figure 6.25). The SHR increased linearly at 82°F, 90°F, 95°F, and 100°F outdoor temperatures with increased charge. For instance, the SHR was 0.727 for -20% charging at 82°F outdoor temperature. It increased linearly to 0.745 and 0.774 for full charged and +20% charging tests. As the outdoor temperature increased, the SHR also increased for a given charge. The effect of outdoor temperature was more noticeable on full charged and high-charge than low-charge conditions. For the -20% charging tests, the SHR increased by 2.5% when the outdoor temperature increased from 82°F to 100°F. However, for the same increase in outdoor temperature, the SHR increased by 6% for +20% charging condition.

Thermal Expansion Valve System

The SHR decreased as the amount of the charge in the system increased until reaching full charge where the SHR remained approximately constant (Figure 6.26). At 95°F outdoor temperature, the SHR dropped by 5% when the unit was charged from

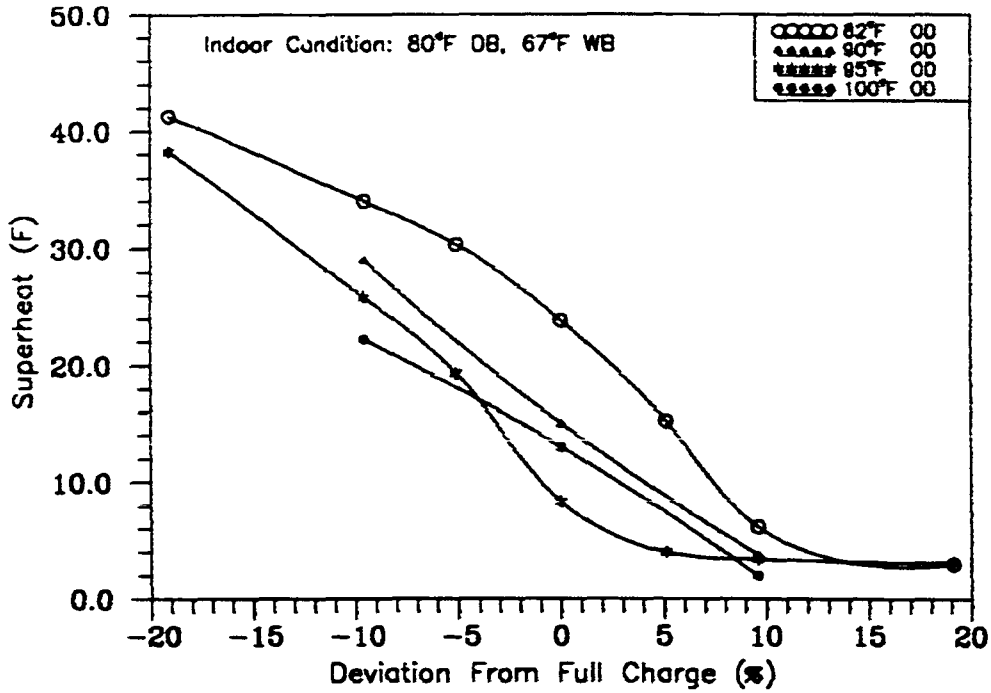

Figure 6.24 - The Short-Tube Orifice System Superheat for Various Outdoor Temperatures and Charging Conditions

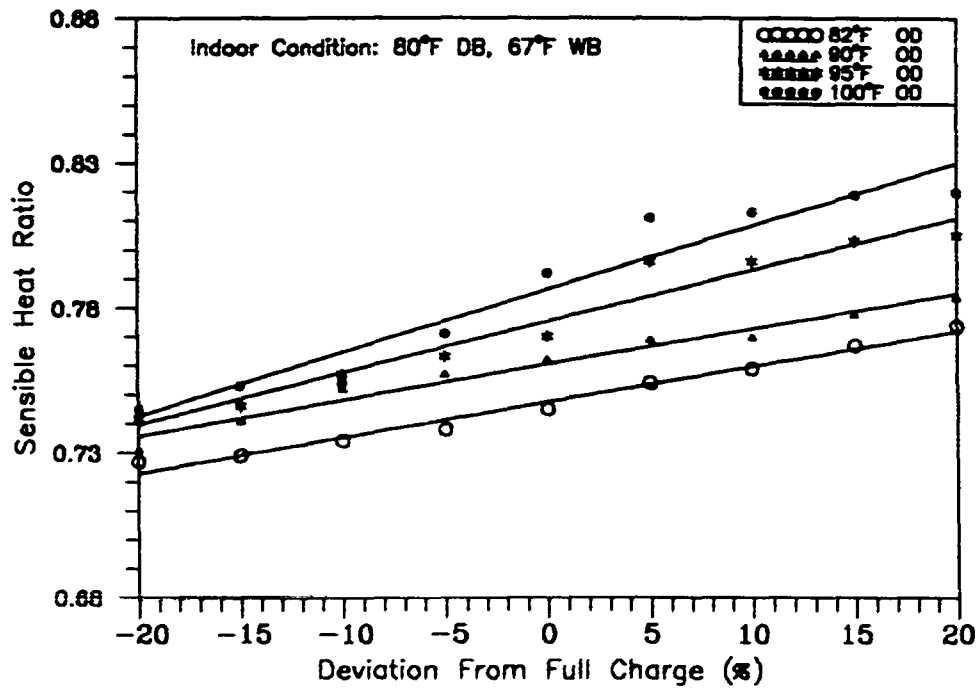

Figure 6.25 - The Capillary Tube System Sensible Heat Ratio for Various Outdoor Temperatures and Charging Conditions

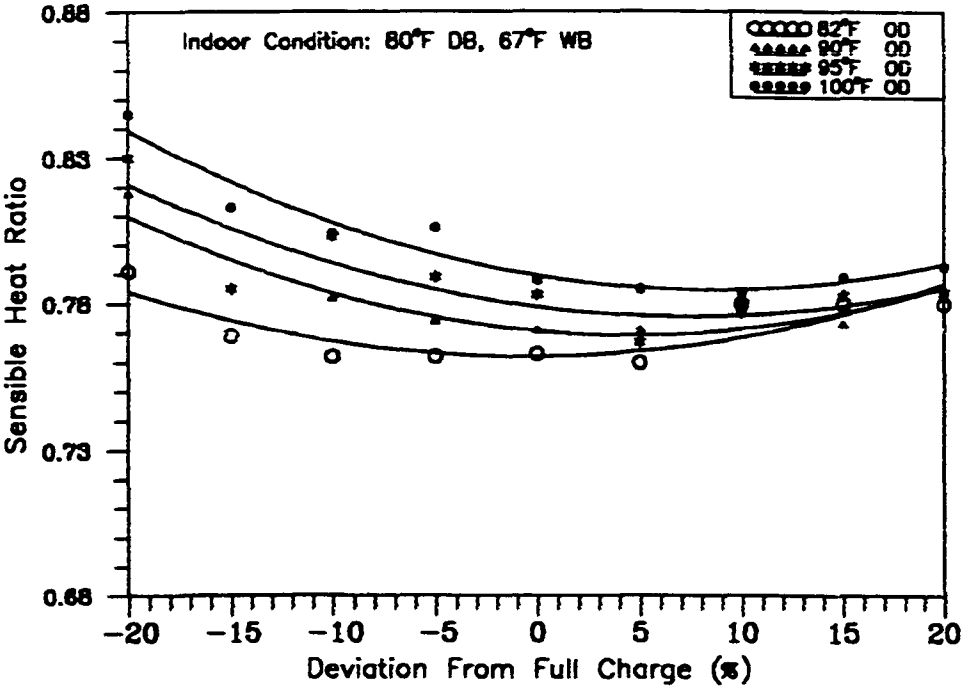

Figure 6.26 - The TXV System Sensible Heat Ratio for Various Outdoor Temperatures and Charging Conditions

-20% charging to full charge. For -20% charging, the SHR increased from 0.79 to 0.85 when the outdoor temperature increased from 82°F to 100°F. In case of high-charge conditions, the SHR was constant for 90°F, 95°F, and 100°F outdoor temperatures. However, the SHR increased slightly for 82°F outdoor temperature. The effect of outdoor temperature was less noticeable for high-charge than low-charge tests. For instance, the SHR increased by less than 2% for high-charge tests when the outdoor temperature increased from 82°F to 100°F.

Short-Tube Orifice Expansion System

The SHR for the short-tube orifice expansion system showed no clear or definitive trends (Figure 6.27). At both 82°F and 95°F outdoor temperatures, the SHR showed a slight increase with increasing charge. For the other two temperatures (90°F and 100°F), there was a small decrease. However, the 90°F and 100°F temperatures only included three charge conditions (-10%, full, and +10%). Because of the small number of data points and the observed scatter, an addition (or reduction) of one data point could change the direction of the trends observed. The SHR for the short-tube orifice system showed less variation with temperature and charge than did the capillary tube system. For instance, the SHR varied from a low of 0.727 (-20% charge, 82°F) to a high of 0.820 (100°F, +20% charge) for the capillary tube system. The SHR for the short-tube orifice system only varied from 0.728 (-5% charge, 82°F) to 0.785 (-10% charge, 90°F).

STEADY STATE AND CYCLIC DRY COIL TESTS

For the dry coil tests, both steady state and cyclic tests were performed with indoor condition set at 80°F DB and 57°F WB. The wet bulb temperature was sufficiently low that no condensate formed on evaporator coil. The outdoor room condition was constantly kept at 82°F DB and 20% RH. The steady state and cyclic tests were repeated on the units for each refrigerant charging condition.

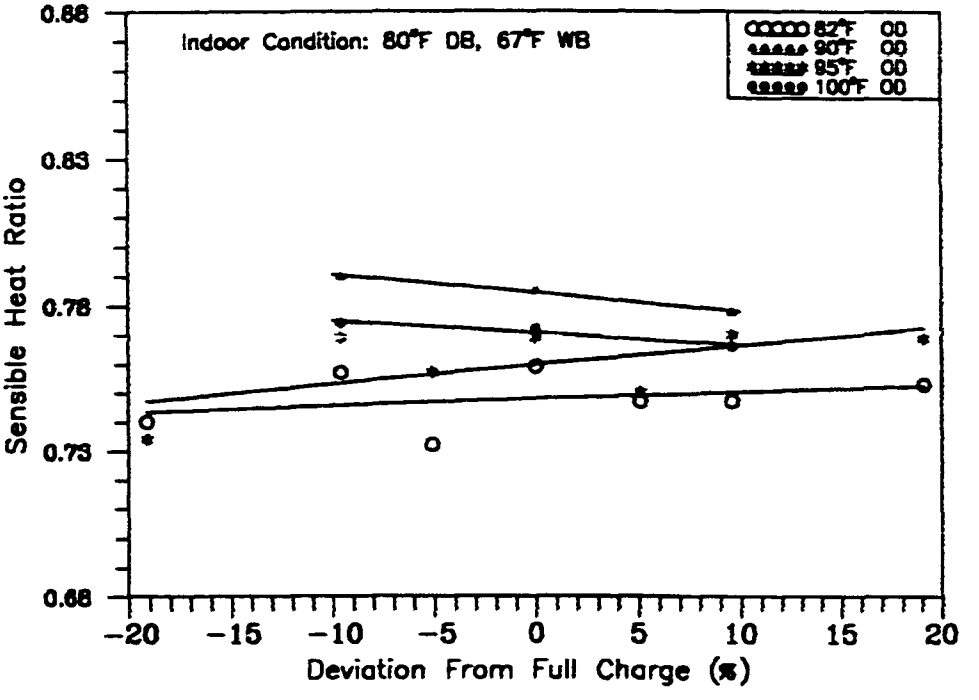

Figure 6.27 - The Short-Tube Orifice System Sensible Heat Ratio for Various Outdoor Temperatures and Charging Conditions

Steady State Capacity

The steady state capacity as a function of charge is shown in Figure 6.28 for the three expansion device systems. For the capillary tube expansion system, the capacity peaked at 32.4 kBtu/hr at full charge and dropped to 25 and 32 kBtu/hr for -20% and +20% charging conditions, respectively. The effect of refrigerant charge as the charge decreased from full charge to -20% charging was more dramatic on the capacity than high-charge conditions.

The capacity for the TXV system was constant at 29.5 kBtu/hr from -5% to +20% charging conditions. The reason for constant capacity was due to the constant refrigerant flow rate and superheat temperature regulated by the TXV. It only dropped to 27.5 kBtu/hr at -20% charging.

For the short-tube orifice expansion system, the capacity was fairly independent of the refrigerant charge. The capacity was constant at 29.0 kBtu/hr for all the charging conditions. This behavior contrasts quite dramatically with the behavior of the capillary tube expansion system shown in Figure 6.28.

Steady State Energy Efficiency Ratio (EER_C)

EER_C is a ratio calculated by dividing the net cooling capacity of dry coil steady state test in Btu/hr by the power input in watts (w) at the given set of rating condition, expressed in Btu/wh.

The EER_C for the capillary tube expansion system showed the same trend as the capacity. As shown in Figure 6.29, the EER_C peaked at 9.8 for fully charged condition. It dropped to 8.5 and 9.2 for -20% and +20% charging conditions, respectively. The effect of charge on EER_C for the capillary tube expansion system was more noticeable than short-tube orifice and TXV expansion device systems.

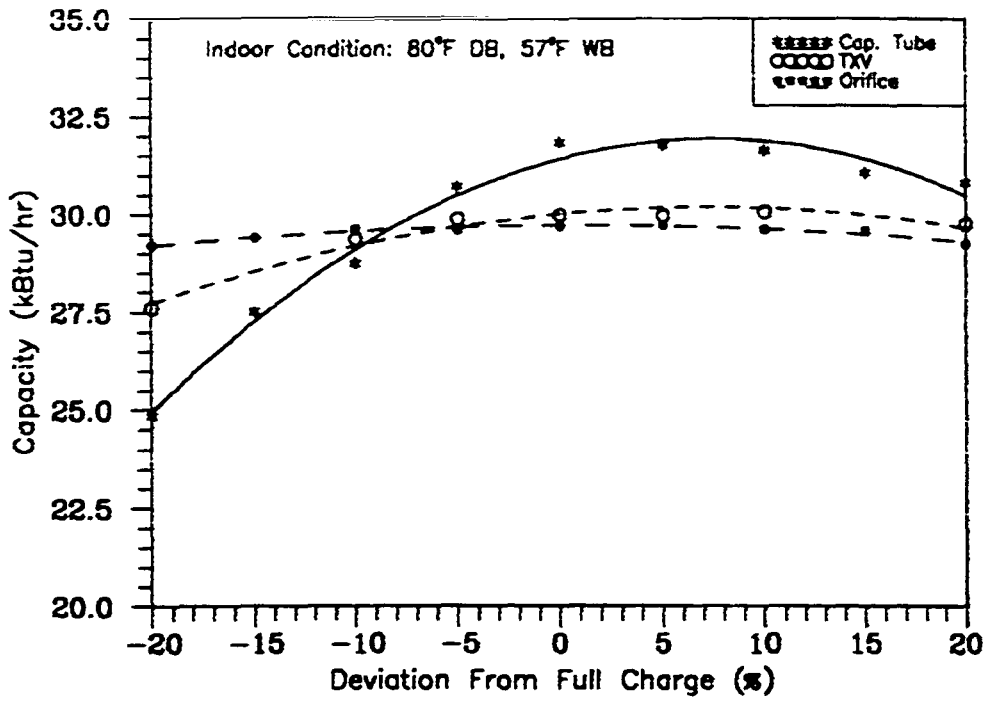

Figure 6.28 - Dry Coil Capacity for the System with Various Expansion Devices and Charging Conditions

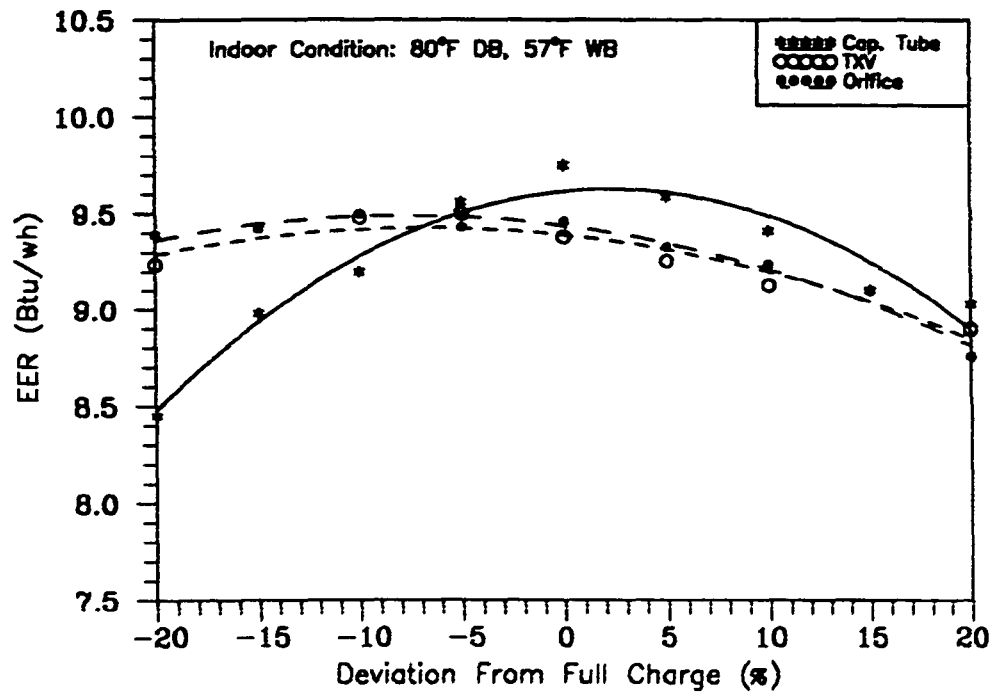

Figure 6.29 - Dry Coil *EER* for the System with Various Expansion Devices and Charging Conditions

EER_C had the same trend for the short-tube orifice and TXV expansion device systems. EER_C peaked at 9.5 for both systems at -10% charging conditions. Both EER_C dropped to 9.3 and 8.9 at -20% and +20% charging conditions, respectively. The effects of refrigerant charge at low-charge conditions on EER_C was less noticeable than that of at high-charge conditions for both short-tube orifice and TXV expansion device systems.

Seasonal Energy Efficiency Ratio (*SEER*)

An important variable in the calculation of the *SEER* is the coefficient of degradation (C_D). This coefficient is a measure of the efficiency loss due to on/off cycling of the system. Upon compressor start-up, the cooling capacity of an air conditioner increases to its steady state value gradually, rather than instantaneously. This lack of an instantaneous response leads to lower average capacities and efficiencies than the respective steady state values. The larger the value of C_D, the larger the losses attributed to cycling in the system. It is determined from measurements taken in tests steady state and cyclic tests specified in the DOE/ARI test procedure.

For the unit with the capillary tube expansion device, C_D varied from 0.21 at -20% charging to 0.25 at -5% charging conditions. With increasing refrigerant charge in the system, C_D rapidly dropped down to 0.15 at +20% charging condition (Figure 6.30). The smaller C_D value at high-charge condition (+10, +15 and +20%) suggested that the unit reached steady state after start up more rapidly than with the low-charge tests. With more refrigerant charge in the system, the compressor can move more refrigerant through the heat exchangers and produce the required heat transfer effect more rapidly. For the short-tube orifice expansion system, C_D was relatively constant at 0.125 from -20% charging to full charge conditions. As the charge in the system increased, the C_D dropped to 0.115 at +20% charging.

C_D varied little with the refrigerant charge for the TXV system. It was 0.123 at

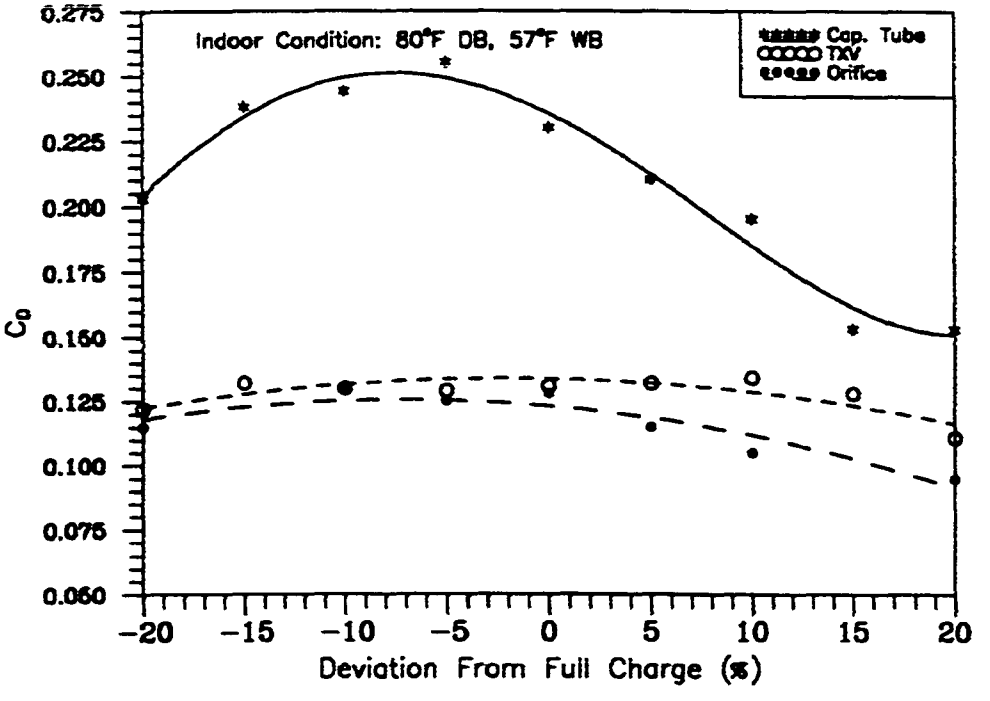

Figure 6.30 - Coefficient of Degradation for the System with Various Expansion Devices and Charging Conditions

-20% charging condition and gradually dropped to 0.115 at +20% charged condition. The trend of a low C_D at low-charge, reaching a plateau, and then decreasing slowly with increasing charge was similar to the trend found in the short-tube orifice expansion system.

Figure 6.30 showed that C_D for the capillary tube expansion system was higher than the short-tube orifice and TXV expansion systems at any given charge. This suggested that the units with short-tube orifice and TXV expansion devices reached steady state after start up more rapidly than the unit with the capillary tube expansion device. The trend of a low C_D at low charge, reaching a plateau, and then decreasing with increasing charge is similar to the trend found in the capillary tube system. It was also found that C_D for the short-tube orifice and TXV systems varied little with refrigerant charge. However, the capillary tube expansion system showed a strong dependence on the refrigerant charge in the system.

Figure 6.31 shows that the *SEER* had a distinct peak at full charge of 9.44. The sharp peak in *SEER* at the full charge would suggest that for this system and perhaps others with capillary tube expansion, that precise charging is important for optimal performance. For a 5% loss in charge (only 7 ounces), there was a 6.1% drop in *SEER*. For a +5% charging, there was a 4.7% drop in *SEER*. The *SEER* continued dropping rapidly down to a low of 7.50 for charging of -20%. For +20% charging the drop in *SEER* was only to 8.47. For this system, high-charge conditions did not degrade the *SEER* as much as low-charge cases.

At full charge, the *SEER* was 9.7 for the TXV system. The *SEER* curve peak was 9.86. It occurred at -15%, -10%, and -5% charging conditions. It dropped to 8.9 for +20% charging. At low-charge conditions, the *SEER* did not show the dramatic drop that the capillary tube expansion system showed.

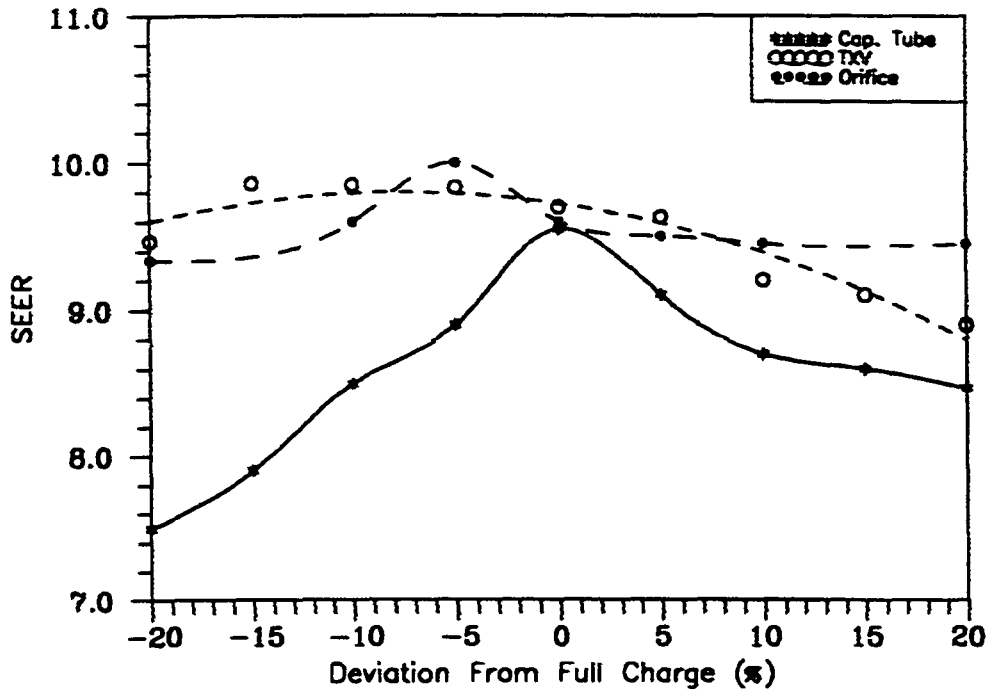

Figure 6.31 - Seasonal Energy Efficiency Ratio (*SEER*) for the System with Various Expansion Devices and Charging Conditions

The *SEER* peaked at 9.9 for -5% charging and decreased to approximately 9.3 (6% drop) for both +20% and -20% charging for the unit with the short-tube orifice expansion device (Figure 6.31). This suggests that the effect of charge on the *SEER* was not as dramatic as the capillary tube expansion system. The *SEER* was constant at 9.3 for all the charging conditions.

SUMMARY OF EXPERIMENTAL RESULTS FOR OFF-DESIGN TESTS

A number of tests were run for a wide range of refrigerant charge in the system. For each charge, the air conditioner was subjected to a range of outdoor temperatures and three expansion devices. This study illuminated certain trends required to characterize the off-design charging on the performance of air conditioner. In the following section, the effects of charging on the system performance is presented for each expansion device.

Capillary Tube Expansion System

The results of the experimentation showed that the total capacity (wet and dry coil tests), *EER*, and *SEER* decreased with increasing outdoor temperature for the fully charged case. The sensible heat ratio increased as the outdoor temperature increased.

One surprising result was the increase of the capacity for the low-charge conditions as compared to the full or high-charge cases. For the low-charge tests, the capacity increased as the outdoor temperature increased. One possible explanation for this behavior was in the changes of the refrigerant flow rate by the capillary tube for different charges.

In general, the degradation of performance was larger for low-charge than that of for high-charge conditions. The measure of seasonal performance, *SEER*, dropped from 9.5 to 7.5 for -20% charging while only dropping to 8.4 for +20% charging. The data for capacity showed similar trends. Another measure of performance is the capacity and power during the hottest part of the summer days. The 100°F test would provide some

hints at this performance. The total capacity peaked for -5% charging at 34.0 kBtu/hr. It dropped to 26.3 kBtu/hr at -20% charging and 28.9 kBtu/hr at +20% charging condition.

As the outdoor temperature increased, the subcooling was constant for the low-charge tests where it increased for the high-charge cases. The superheat at the outlet of the evaporator decreased as the outdoor temperature increased. For +10%, +15%, and +20% charging, the refrigerant at the outlet of the evaporator was saturated. The refrigerant saturated conditions at the evaporator outlet could indicate possible introduction of wet vapor into the compressor.

Thermal Expansion Valve System

The results of the experimentation showed that the total capacity (wet and dry coil tests) and *EER* decreased with increasing outdoor temperature for at any charging condition. The degradation of performance was larger for the extreme off-design charging (-40%, -30%, and -20%) than that for other charging tests. The *EER* and the total capacity (wet and dry tests) of the unit were approximately constant over a wide range of charging (from -15% to +10%) for a given outdoor temperature.

The TXV maintained a relatively constant superheat by regulating the refrigerant flow rate in the system. The data indicated that the refrigerant flow rate were similar for all the charging tests except for -40%, -30%, and -20% charging. The similar flow rates would explain why the total capacity remained relatively constant from -15% to +10% charging.

SEER peaked between -10% and -5% charging rather than manufacturer suggestion (full charge). It dropped from 9.7 at full charge to 9.4 for -20% charging while only dropping to 8.9 for +20% charging. With a TXV, the maximum *SEER* was 9.85 at -15%, -10%, and -5% charging. For -20% charging, the degradation of performance was larger for the capillary tube than the TXV system. The *SEER* dropped

to 7 (27% reduction) with capillary tubes and only to 9.5 (3.5% reduction) with the TXV. In case of +20% overcharging, *SEER* dropped to 8.55 (11.4% reduction) and 8.9 (9% reduction) for capillary tube and TXV systems, respectively.

Another conclusion from the TXV study was the small variation of capacity, *EER*, and *SEER* with refrigerant charge. The results from the study on the capillary tube expansion system suggested that a fixed expansion device would be extremely sensitive to changes in refrigerant charge. For instance, a reduction of 10% refrigerant charging would result in a 11.5% reduction in the *SEER* for the system with a capillary tube. However, the same condition would lead to 1.5% increase in the *SEER* for the TXV system.

Short-Tube Orifice Expansion System

The unit total capacity showed a peak at +15% charging and between +5% and +10% charging for 82°F and 95°F outdoor temperatures, respectively. The effect of outdoor temperature was much more noticeable in high-charge than low-charge conditions on the unit total capacity. The *EER* showed a strong dependence on outdoor temperature, but varied little with charge. The *EER* varied from 9.1 at -20% to 8.6 at +20% charging. This behavior contrasts quite dramatically with the behavior of the capillary tube expansion system.

Subcooling increased with increasing charge for all the outdoor temperatures. It increased from 1°F at -20% to 12.5°F for +20% charging conditions steadily. The superheat was extremely sensitive to the charge. At full charge the superheat was 8°F for 95°F outdoor temperature. A drop in charge of 5% increased the superheat to 19°F.

The *SEER* peaked at 9.9 for -5% charging and decreased to approximately 9.3 (6% drop) for both +20% and -20% charging for the unit with the short-tube orifice expansion device. This suggests that the effect of charge on the *SEER* was not as

dramatic as the capillary expansion system. The *SEER* was constant at 9.3 for low-charge high-charge conditions except at -5% charging.

CHAPTER VII

COMPARISON OF MODEL AND EXPERIMENTAL RESULTS

The ORNL heat pump model was improved by replacing the existing heat exchanger model with one which simulated the heat exchangers with tube-by-tube refrigerant flow through the coil. Because the simulated system performance depends upon the choice of a void fraction model, the best void fraction model had to be identified. In this chapter, the criterion for evaluating a void fraction model is discussed and the system results estimated by the void fraction model are compared with the experimental results discussed in the previous chapter.

The refrigerant heat transfer coefficient and pressure drop calculated in the evaporator and condenser depend upon the void fraction model. Therefore, it is important to choose a void fraction model which accurately predicts the system refrigerant charge inventory as well as system performance. Eight choices of void fraction models ranging from simple to complex models are available in the ORNL model. For a given refrigerant charge in the system, the system performance as a function of void fraction model was simulated.

The void fraction is generally represented as a function of mass quality, x, and combinations of various types of properties correlations (viscosity, density,...). Only a few void fraction models (Hughmark, Premoli, and Tandon) have dependences on refrigerant mass flow rate. To determine the effect of void fraction models on the system performance, the ORNL model was run with all eight void fraction models for the capillary tube expansion system at all charging conditions at 82°F outdoor temperature. The system performance is directly related to the refrigerant flow rate, superheat, and subcooling temperatures. These parameters as a function of refrigerant charge for each void fraction model were evaluated and compared with the measured results. The void

fraction models were classified into two categories: (i) mass-flow independent and (ii) mass-flow dependent. The superheat predicted by the mass-flow independent (Homogeneous, Zivi, L-M, Thom, and Baroczy models) was compared to the experimental results in Figure 7.1. Among the models, only the Baroczy prediction was within 10°F of the measured superheat. The predicted superheat reached saturation state (0° superheat) at full charge. The Hughmark model predicted the superheat temperature within 2°F (Figure 7.2). The Tandon and Premoli models underestimated the superheat temperature by 10° to 20°F. These models, like the Zivi and Baroczy models, predicted no superheat at full charge conditions where the experimental superheat was 21°F.

The comparison of subcooling temperature for mass-flow independent and mass-flow dependent void fraction models are shown in Figures 7.3 and 7.4, respectively. The Baroczy, Zivi (Figure 7.3), Tandon, and Premoli (Figure 7.4) models predicted the subcooling within 2°F for -20% charging to full charge conditions. As the charge in the system increased, the experimental subcooling temperature increased linearly where as the predicted ones asymptotically reached a constant of 18.7°F throughout the high-charge conditions. The Hughmark model predicted the subcooling temperature within an average of 6°F of the experimental results. The simulated subcooling reached 18.7°F at +10% charging and remained constant at +15% and +20% charging conditions.

All the models overestimated the refrigerant flow rates at all the charging conditions (Figures 7.5 and 7.6). The refrigerant flow rate predicted by the Homogeneous model was 505 lbm/hr for -20% charging condition. It reached 516 lbm/hr at -15% charging and remained constant for the rest of charging conditions. The refrigerant flow rate predicted by Zivi and Baroczy models was within +13% from -20% charging to full charge conditions. The difference between the predicted and experimental refrigerant flow rate decreased to 3% for +20% charging condition. The refrigerant flow rate was constant at 516 lbm/hr predicted by all the models for full

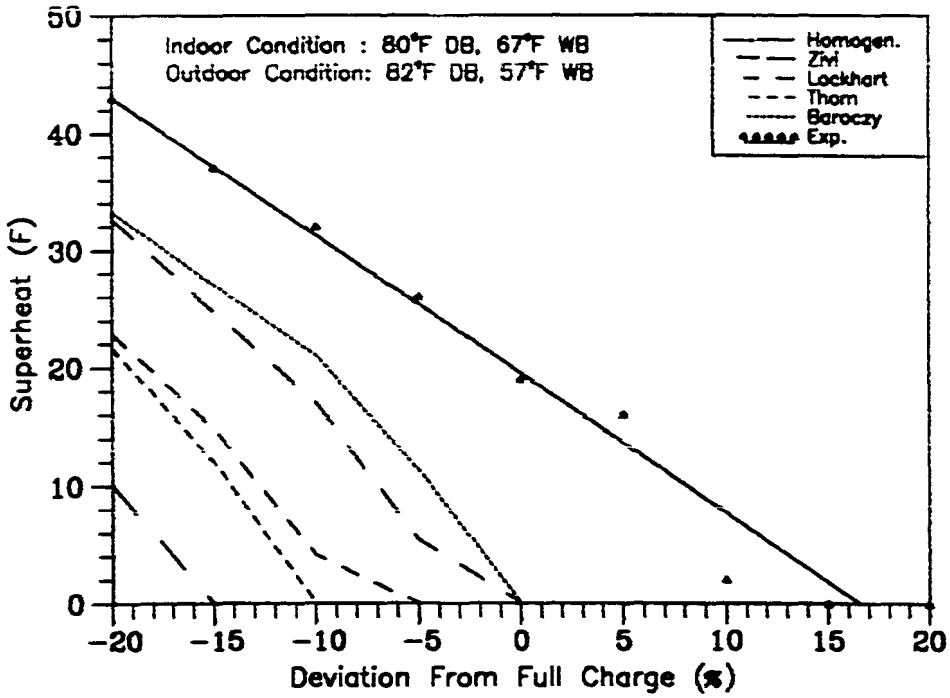

Figure 7.1 - Comparison of Superheat Temperature for the Mass-Flow-Independent Models

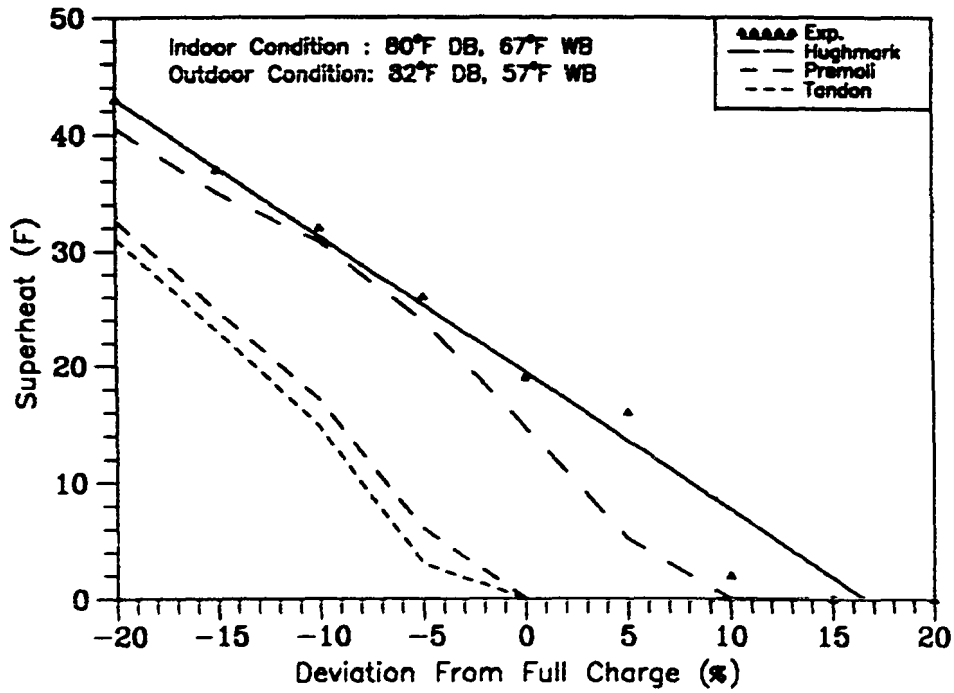

Figure 7.2 - Comparison of Superheat Temperature for the Mass-Flow-Dependent Models

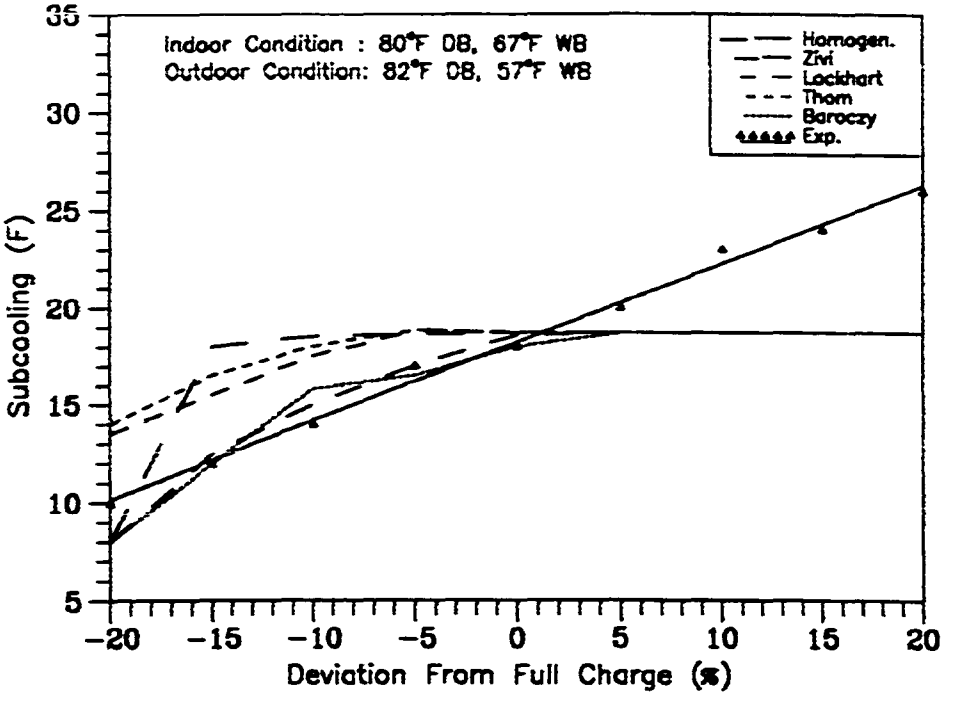

Figure 7.3 - Comparison of Subcooling Temperature for the Mass-Flow-Independent Models

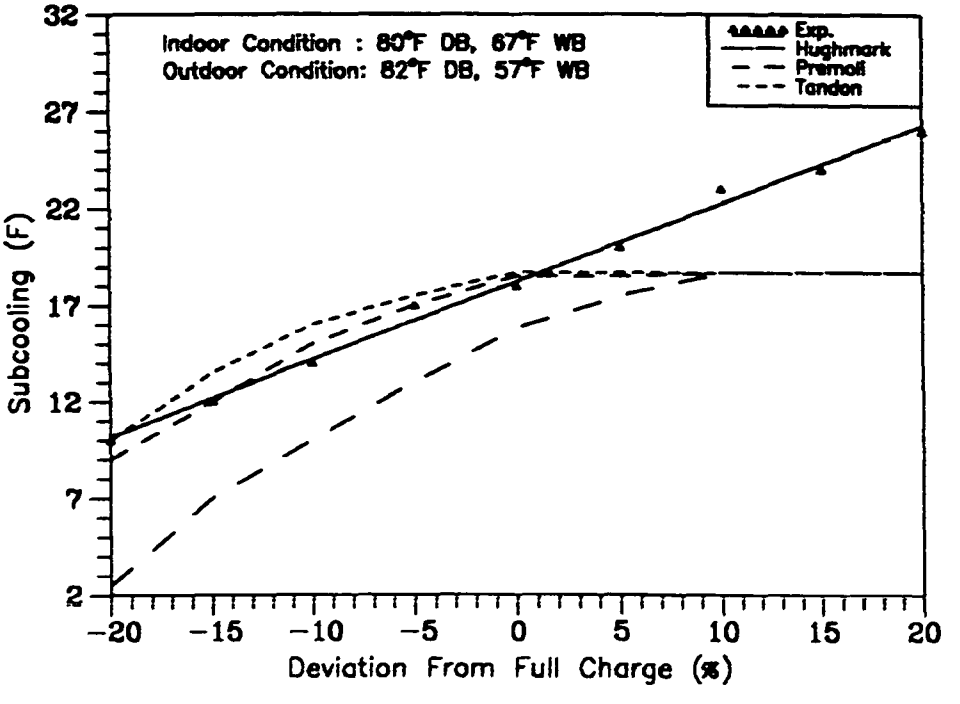

Figure 7.4 - Comparison of Subcooling Temperature for the Mass-Flow-Dependent Models

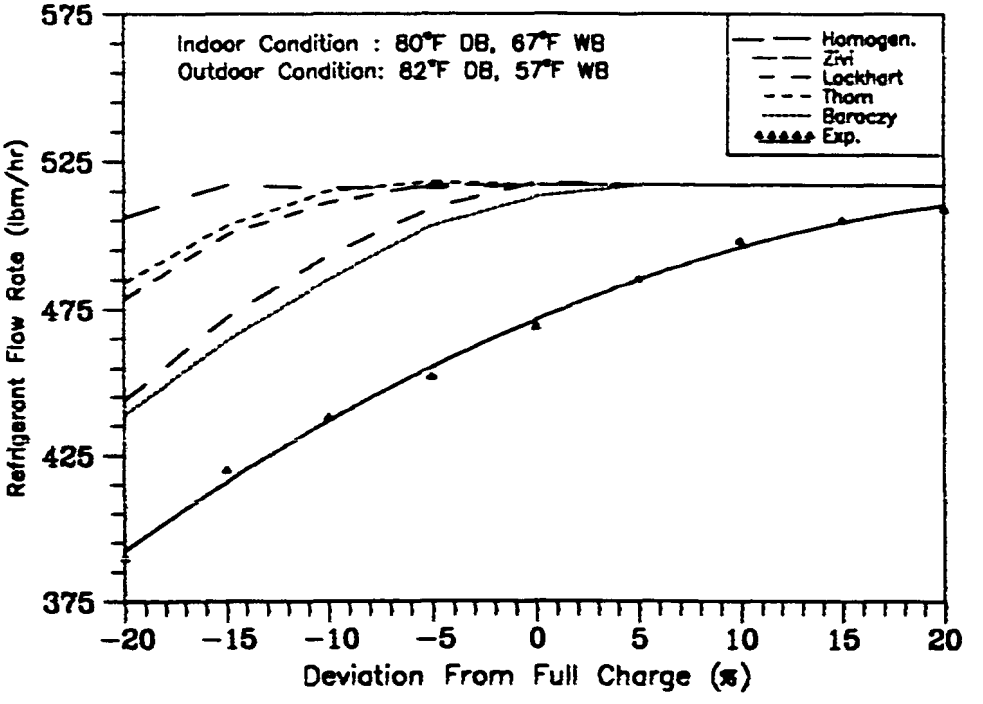

Figure 7.5 - Comparison of Refrigerant Flow Rate for the Mass-Flow-Independent Models

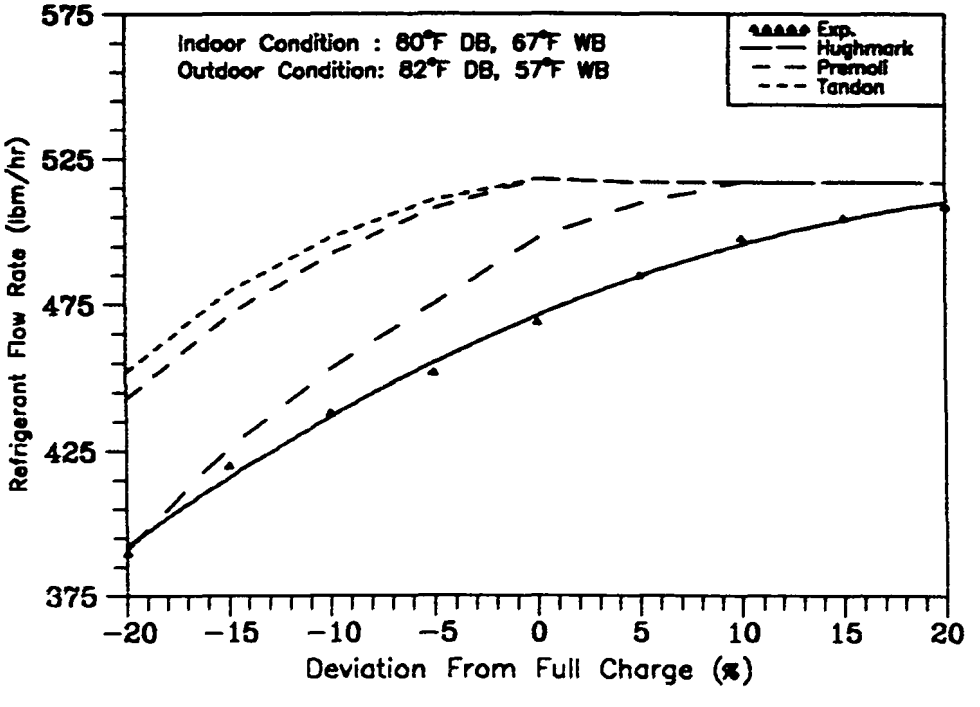

Figure 7.6 - Comparison of Refrigerant Flow Rate for the Mass-Flow-Dependent Models

charge and high-charge conditions except for the Hughmark model. Among all the models, only the Hughmark model predicted the refrigerant flow rate within 2% for +/-20%, +/-15%, and +/-10% charging and 6% from -5% to +5% charging conditions.

The total capacity was simulated for each void fraction model (Figures 7.7 and 7.8) to verify the overall proper void fraction model. For the mass-flow independent models (Figure 7.7), the total capacity predicted by the Lockhart and Thom models were constant at 34 kBtu/hr from -5% to +20% charging conditions. The Zivi and Baroczy models predicted identical total capacity at all the charging conditions. The total capacity by their models peaked at -5% charging. The simulated capacity decreased to 34 kBtu/hr at +5% charging and remained constant for +10%, +15%, and +20% charging conditions. The reason for constant total capacity (from +5% to +20% charging) was the constant subcooling and refrigerant flow rate estimated by the models. All the mass-flow independent models overestimated the capacity at low charging conditions. For instance, the Zivi and Baroczy models overestimated the total capacity by 32% when compared to the measured capacity at -20% charging condition. The difference between the measured and estimated capacity was even higher for the Lockhart and Thom models. Their models overestimated the capacity by 44% and 20% for -20% and -10% charging conditions, respectively. For mass-flow dependent models, the total capacity predicted by the Premoli and Tandon models was identical for all the charging conditions. They predicted the capacity within 3% from full charge to +20% charging conditions. In low-charge conditions, the Premoli and Tandon models overestimated the capacity by 32% and 9% for -20% and -5% charging conditions, respectively. Among all the void fraction models, only the Hughmark prediction of capacity followed the experimental trend. The predicted capacity peaked at full charge was within 3% of the experimental capacity. It followed the measured capacity closely within 1% at +10%,+15%, and +20% charging conditions. The predicted capacity was within 12% and 10% for -20% and -10%

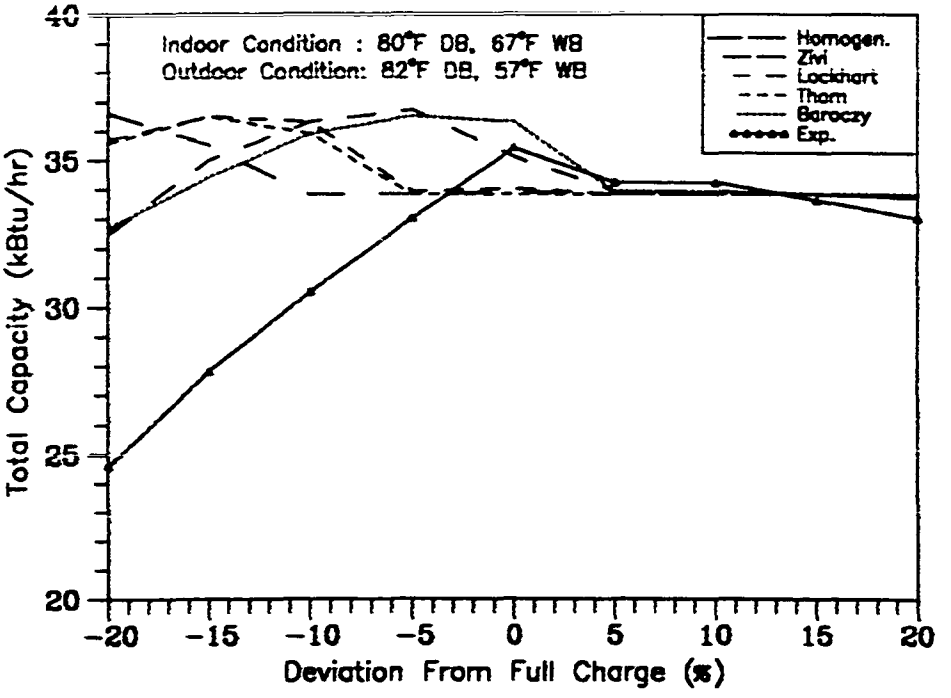

Figure 7.7 - Comparison of Total Capacity for the Mass-Flow-Independent Models

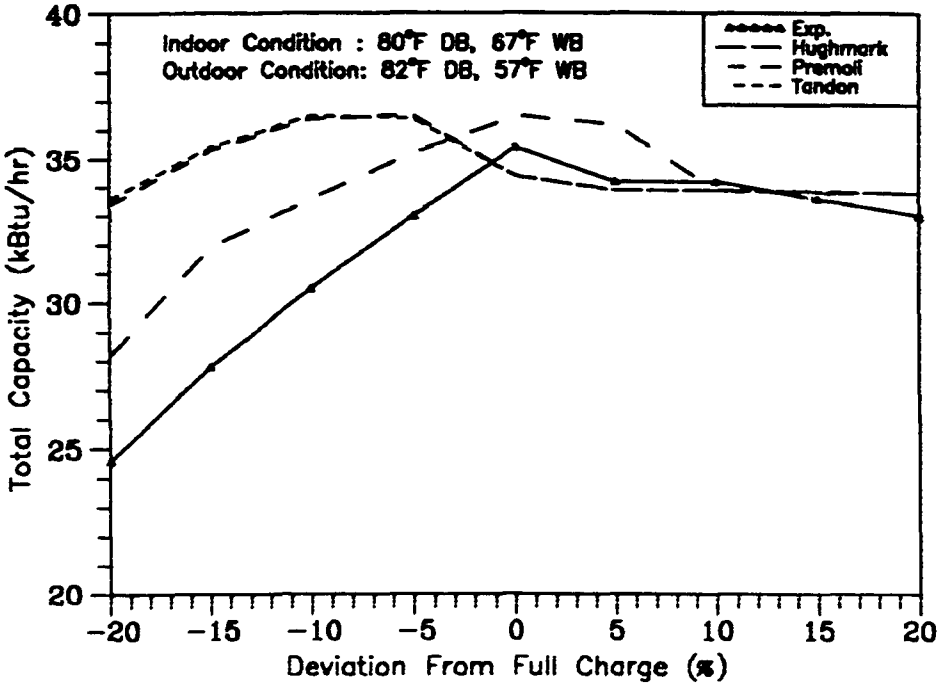

Figure 7.8 - Comparison of Total Capacity for the Mass-Flow-Dependent Models

charging conditions, respectively.

The system capacity, refrigerant flow rate, superheat, and subcooling temperature were compared with the experimental results for each void fraction at all charging conditions. From the above comparisons, the Hughmark void fraction model predicted the system parameters closest to the measured results among the void fraction models. Therefore, the Hughmark void fraction model was used in the present model to compare the simulated with the measured system performance variables.

For steady state wet coil conditions, the new ORNL heat pump model was run for +/-20%, +/-15%, +/-10%, and +/-5% of full charge to cover the full range of off-design charging conditions for all the three expansion devices. All the simulated tests were run at two outdoor temperatures (82°F and 95°F).

STEADY STATE WET COIL TESTS

The effects of charging and the outdoor temperature on the system performance is presented for each expansion device.

Capillary Tube Expansion System

The model predicted the refrigerant superheat temperature an average of 3° lower than the experimental superheat for all the charging conditions at 82°F outdoor temperature (Figure 7.9). As the refrigerant charge in the system increased, the predicted and measured superheat temperatures decreased linearly. No superheat was measured at +15% and +20% charging conditions where the model predicted saturation state for +10%, +15%, and +20% charging conditions. As the outdoor temperature increased from 82°F to 95°F, the predicted and experimental superheat temperatures decreased for a given charging condition. At 95°F outdoor temperature (Figure 7.10), the simulated superheat was an average of 2° higher than experimental superheat from -20% charging to full charge conditions. From +5% to +20% charging conditions, no superheat

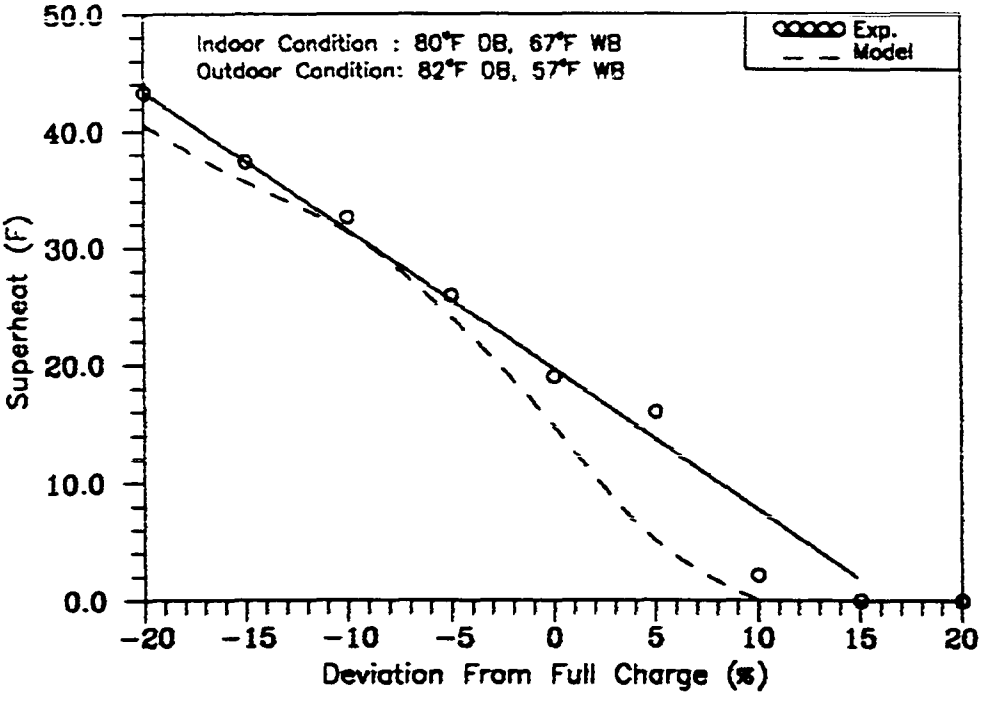

Figure 7.9 - Comparison of Superheat at 82°F Outdoor Temperature for the Capillary Tube System

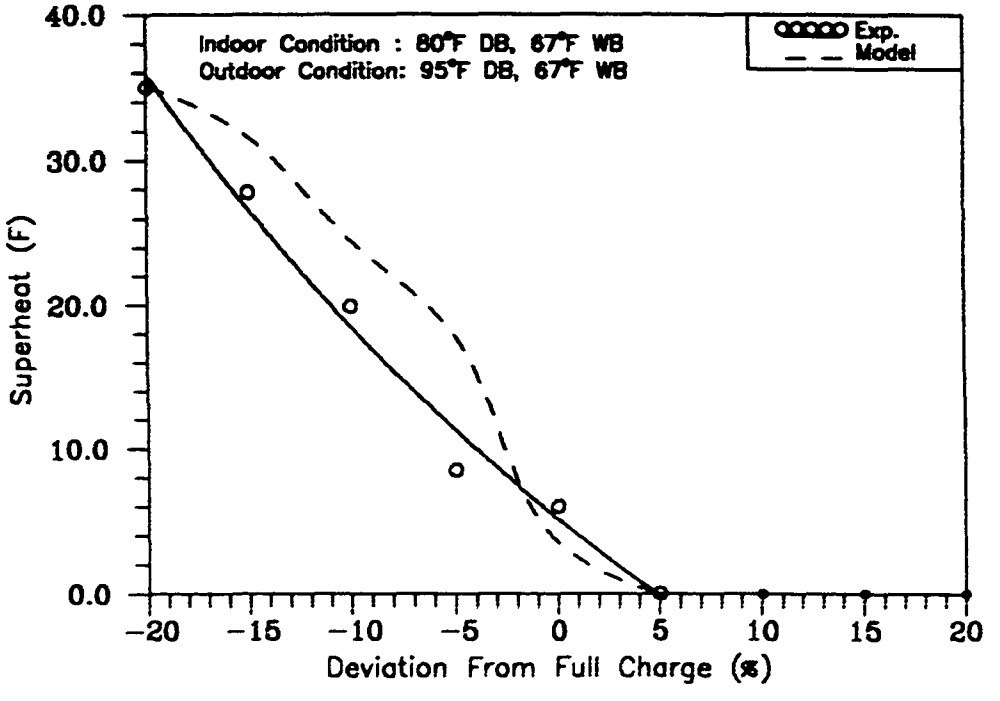

Figure 7.10 - Comparison of Superheat at 95°F Outdoor Temperature for the Capillary Tube System

temperature was predicted by the model which followed exactly the experimental refrigerant superheat condition.

The comparisons of subcooling temperature for 82°F and 95°F outdoor temperatures are shown in Figures 7.11 and 7.12, respectively. As the refrigerant charge in the system increased, the experimental and predicted subcooling temperatures increased linearly for both outdoor temperatures. The model predicted the subcooling temperature 4°F lower than the experimental subcooling at all the charging conditions for 82°F outdoor temperature. As the outdoor temperature increased from 82°F to 95°F, the predicted subcooling was within 8°F of the experimental subcooling temperature at all the charging conditions. The lower predicted subcooling temperature was due to the lower estimated condenser pressure at a given charging condition. For instance, the model predicted the condenser pressure at full charge condition 11% lower than the measured condenser pressure (Figures 7.13 and 7.14). One possible explanation for the higher experimental condenser pressure was the 30 psi pressure drop across the condenser where the model predicted 1 psi.

For the 82°F outdoor temperature condition, the simulated system refrigerant flow rate was 3% higher than the measured refrigerant flow rate for all the charging conditions (Figure 7.15). As the charge in the system increased, the measured and predicted refrigerant flow rates increased linearly. The predicted refrigerant flow rate followed the measured data within 2% for 95°F outdoor temperature (Figure 7.16). As the outdoor temperature increased from 82°F to 95°F, the experimental and predicted refrigerant flow rates increased at any given charging condition. This behavior was due to the decrease in the superheat temperature at higher outdoor temperature. One possible reason that the simulated refrigerant flow rate followed the experimental results closely was the good agreement between the predicted and measured superheat temperature (Figures 7.9 and 7.10).

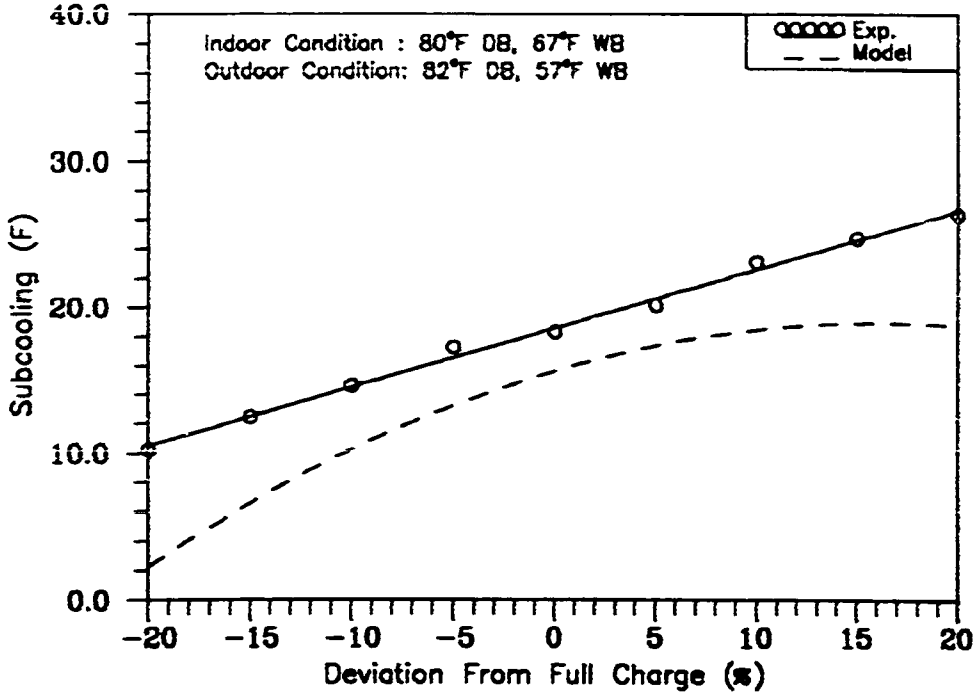

Figure 7.11 - Comparison of Subcooling at 82°F Outdoor Temperature for the Capillary Tube System

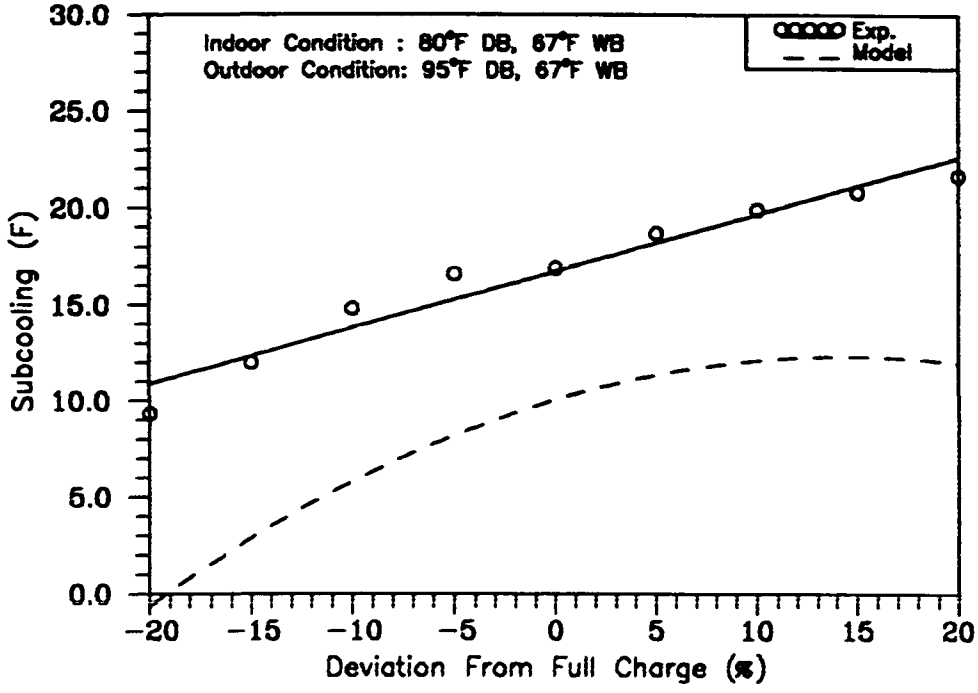

Figure 7.12 - Comparison of Subcooling at 95°F Outdoor Temperature for the Capillary Tube System

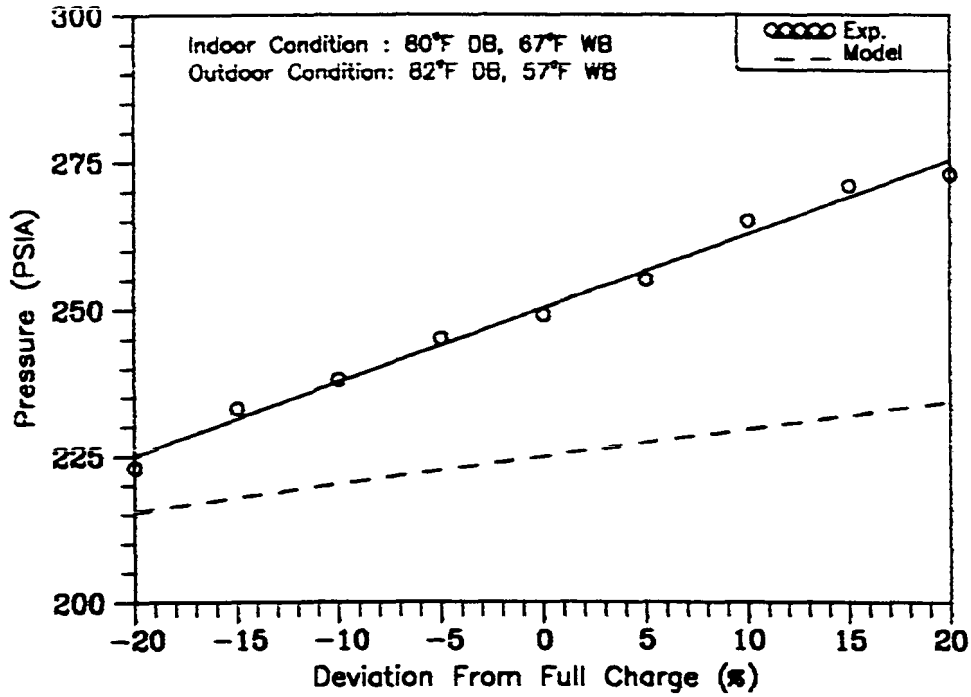

Figure 7.13 - Comparison of Condenser Pressure at 82°F Outdoor Temperature for the Capillary Tube System

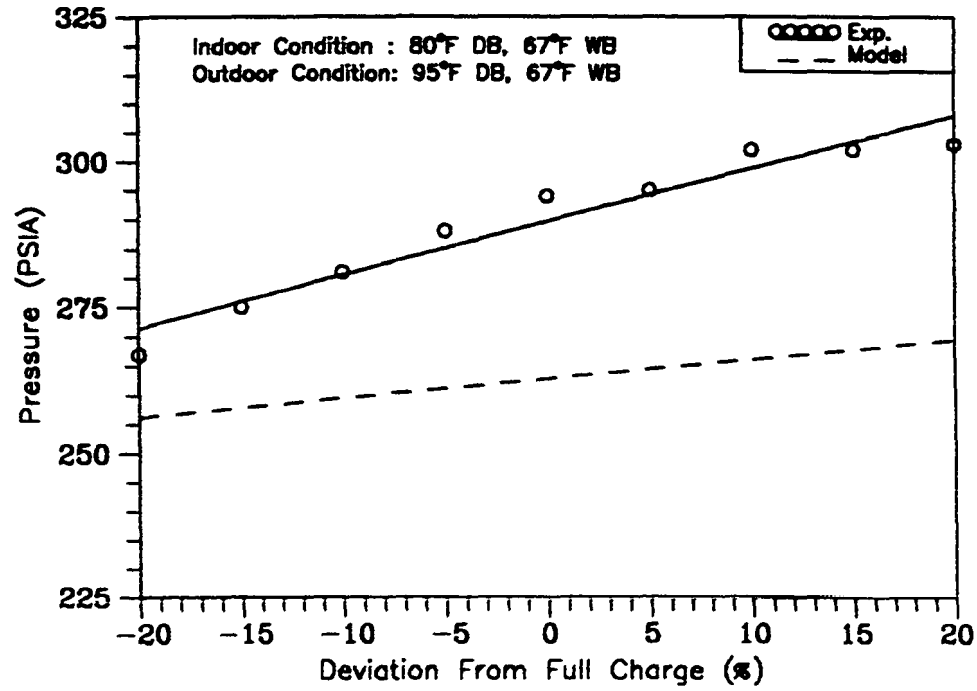

Figure 7.14 - Comparison of Condenser Pressure at 95°F Outdoor Temperature for the Capillary Tube System

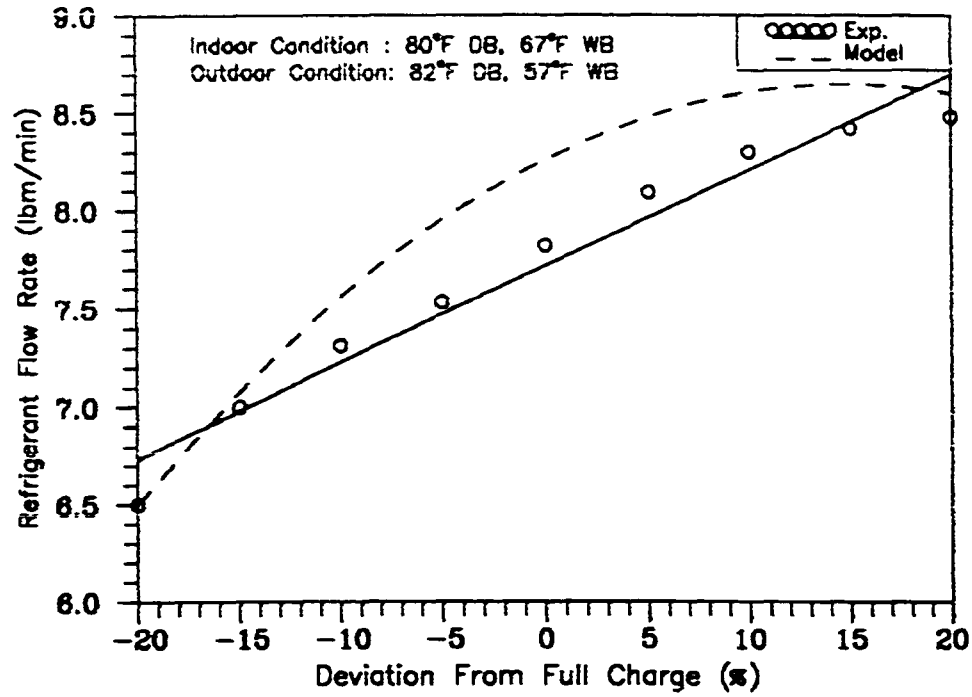

Figure 7.15 - Comparison of Refrigerant Flow Rate at 82°F Outdoor Temperature for the Capillary Tube System

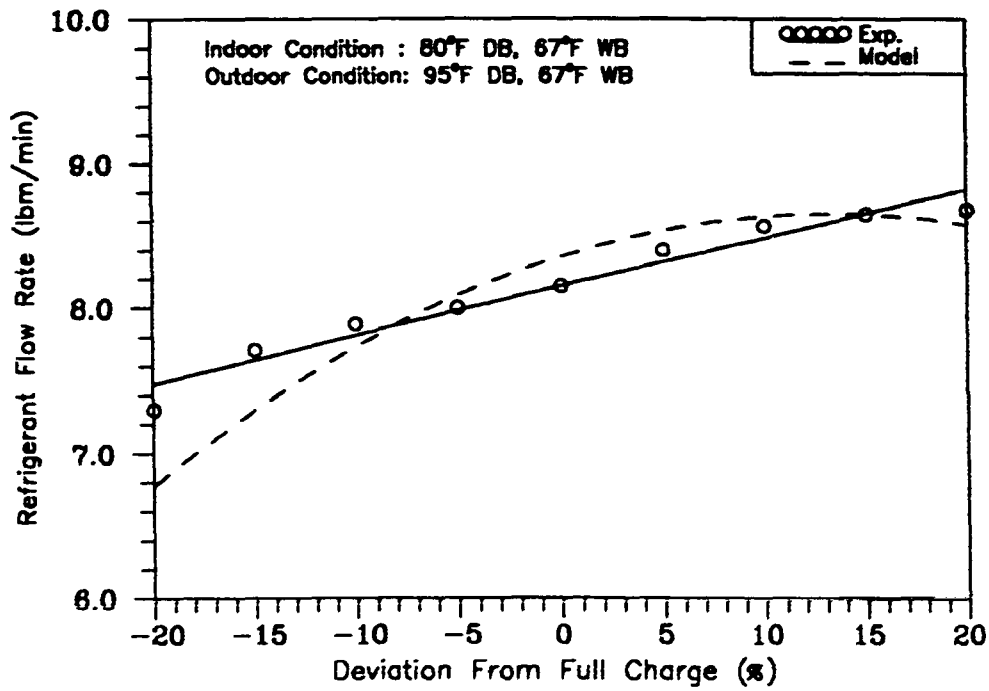

Figure 7.16 - Comparison of Refrigerant Flow Rate at 95°F Outdoor Temperature for the Capillary Tube System

The comparison of simulated total capacity with the experimental results at 82°F and 95°F outdoor temperatures are shown in Figures 7.17 and 7.18, respectively. From -20% to -5% charging conditions, the predicted total capacity was within 10% of the measured capacity at 82°F outdoor temperature. The reason for the higher predicted capacity was the higher predicted refrigerant flow rate (Figure 7.15) and lower simulated subcooling temperature (Figure 7.11). As the refrigerant charge in the system increased, the simulated capacity followed the experimental curve within 3%. As the outdoor temperature increased from 82°F to 95°F, the measured capacity increased for all the low-charge conditions (Figure 6.1). This trend was not predicted by the model at those charging conditions (Figure 7.17). For the same increase in outdoor temperature, the predicted total capacity was lower. For instance, the predicted capacity at 95°F was 3 kBtu/hr lower than the predicated capacity at 82°F outdoor temperature for -10% charging condition. The predicted total capacity followed the experimental within 3% at the 95°F outdoor temperature (Figure 7.18). One reason that the simulated total capacity followed the experimental results closely for the 95°F outdoor temperature condition was the close prediction of refrigerant flow rate (Figure 7.16) and superheat temperature (Figure 7.10).

The trends of *EER* predicted by the model were very similar to the predicted total capacity at 82°F and 95°F outdoor temperatures (Figures 7.19 and 7.20). At 82°F outdoor temperature, the predicted *EER* was within 11% of experimental *EER* at -20, -15, and -10% charging conditions. As the charge in the system increased, the difference between the simulated and experimental *EER* was within 4%. The reason for higher predicted *EER* at low charging conditions was the higher predicted capacity. As the outdoor temperature increased from 82°F to 95°F, the simulated *EER* dropped at all the charging conditions. For instance, the predicted *EER* dropped from 11 to 9.1 Btu/wh at full charge condition. The simulated *EER* followed the experimental results closely

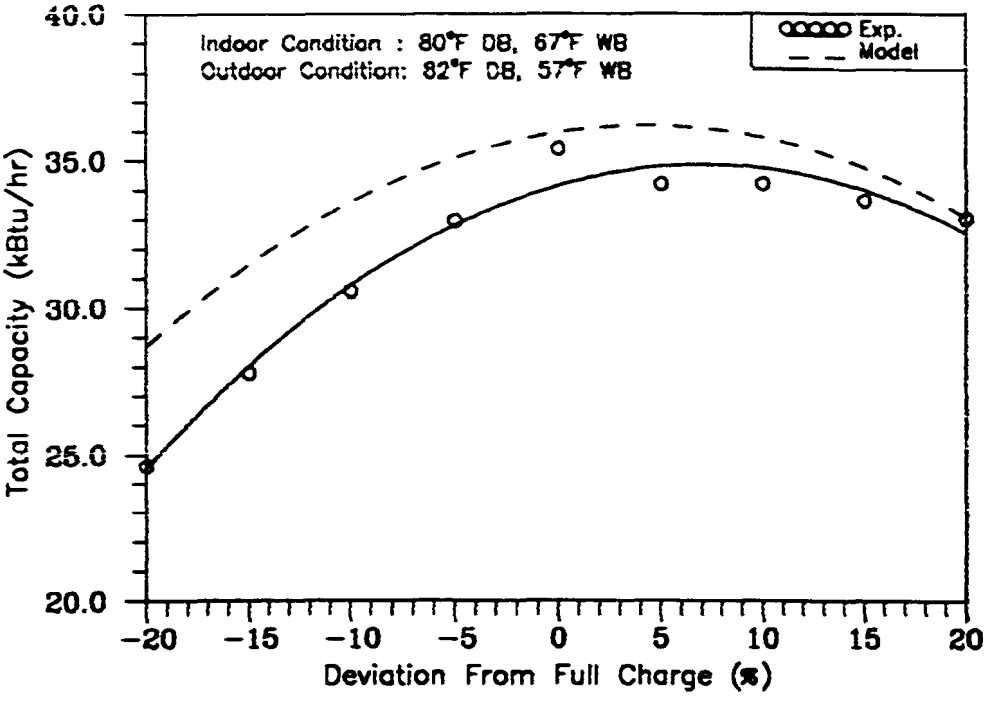

Figure 7.17 - Comparison of Total Capacity at 82°F Outdoor Temperature for the Capillary Tube System

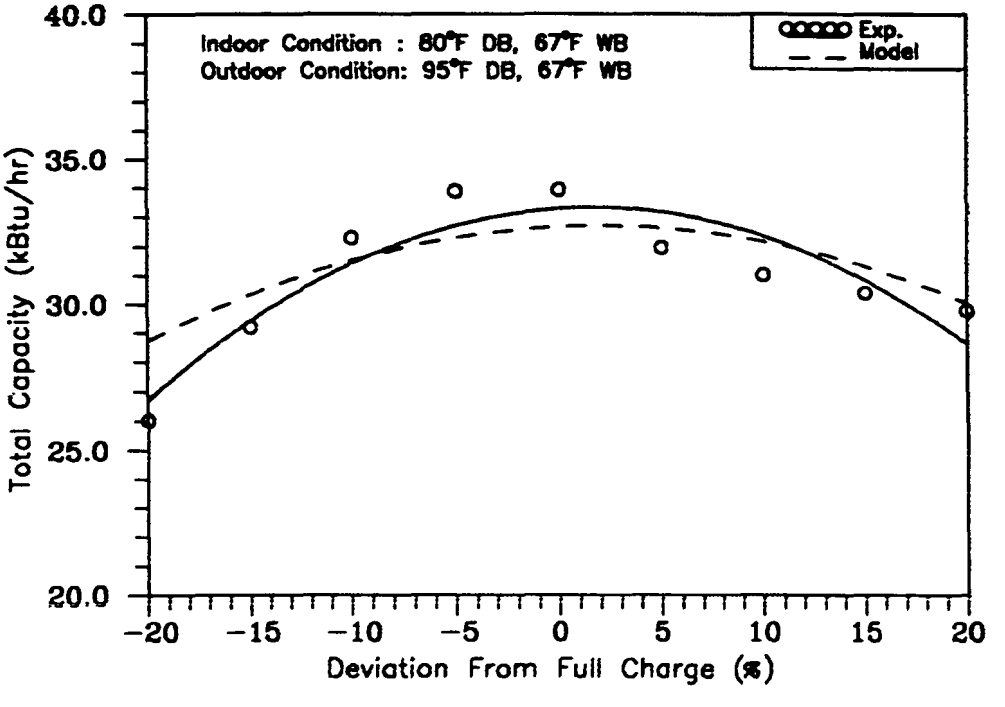

Figure 7.18 - Comparison of Total Capacity at 95°F Outdoor Temperature for the Capillary Tube System

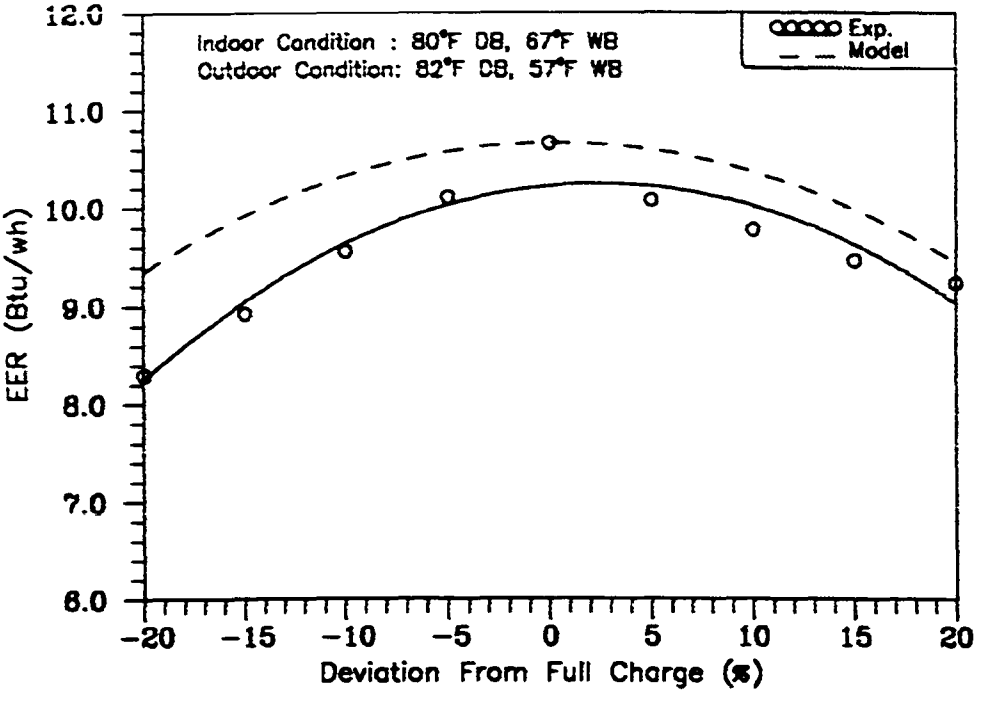

Figure 7.19 - Comparison of *EER* at 82°F Outdoor Temperature for the Capillary Tube System

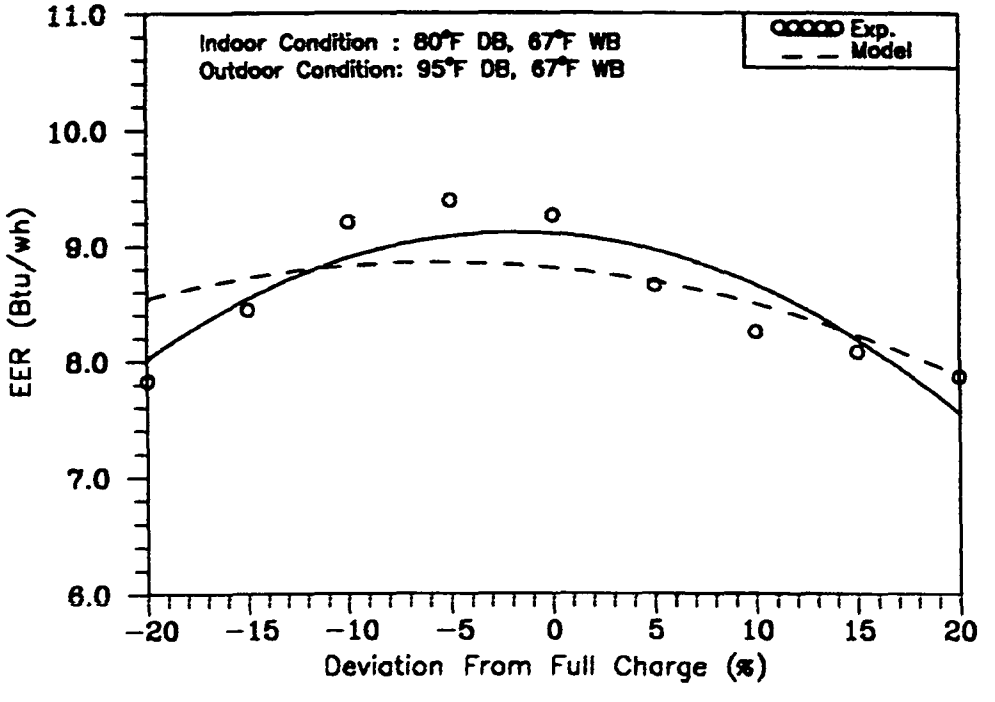

Figure 7.20 - Comparison of *EER* at 95°F Outdoor Temperature for the Capillary Tube System

(within an average of 3%) for all the charging conditions at 95°F outdoor temperature (Figure 7.20).

Thermal Expansion Valve System

One of the options in the ORNL model is to allow the user to specify or design parameters for a TXV. The TXV model requires TXV rated capacity, static superheat, maximum effective superheat and bleed factor. A TXV regulates refrigerant flow rate based on the constant superheat. Therefore, the model predicts the refrigerant flow rate based on the difference between the actual and static superheats. If the actual superheat is lower than static superheat, the TXV model would block the refrigerant flow rate. This condition occurred during the calculation of refrigerant mass inventory in the model. Therefore, the TXV rated capacity was evaluated by trial-and-error using the measured superheat method. The measured superheat was used in the ORNL model to predict the system performance, subcooling temperature and the TXV rated capacity. The measured superheat was 17.5°F and 16°F for all the charging conditions at 82°F and 95°F outdoor temperatures, respectively.

The model predicted the refrigerant subcooling temperature within 3°F for all the high-charge conditions at 82°F outdoor temperature (Figures 7.21). For the case of -20% and -15% charging, the simulated subcooling temperature was within 1°F of the measured subcooling. At 95°F outdoor temperature (Figure 7.22), the estimated refrigerant subcooling temperature was within 2°F of the measured subcooling for all the high-charge conditions. From -20% to -5% charging, the model predicted no subcooling for the high-charge conditions. Lower predicted subcooling was the result of lower predicted condenser pressure for all the charging conditions (Figures 7.23 and 7.24). The predicted condenser pressure was 6% and 8% lower than experimental pressure at 82°F and 95°F outdoor temperatures, respectively. As the outdoor temperature increased from 82°F to 95°F, the predicted condenser pressure increased linearly by an average of 13%

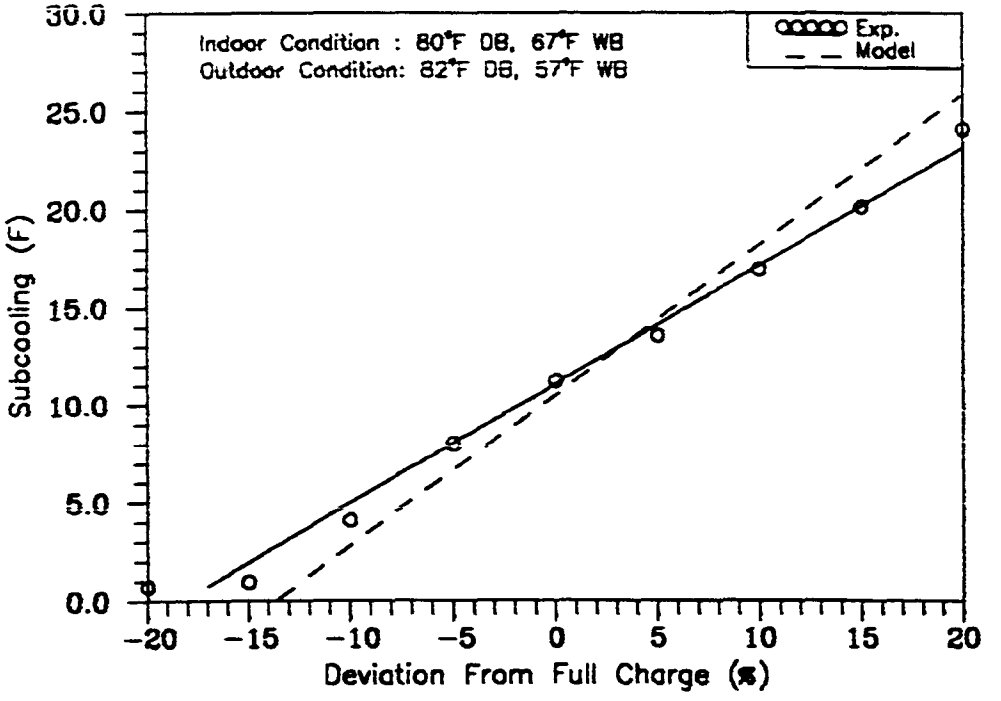

Figure 7.21 - Comparison of Subcooling at 82°F Outdoor Temperature for the TXV System

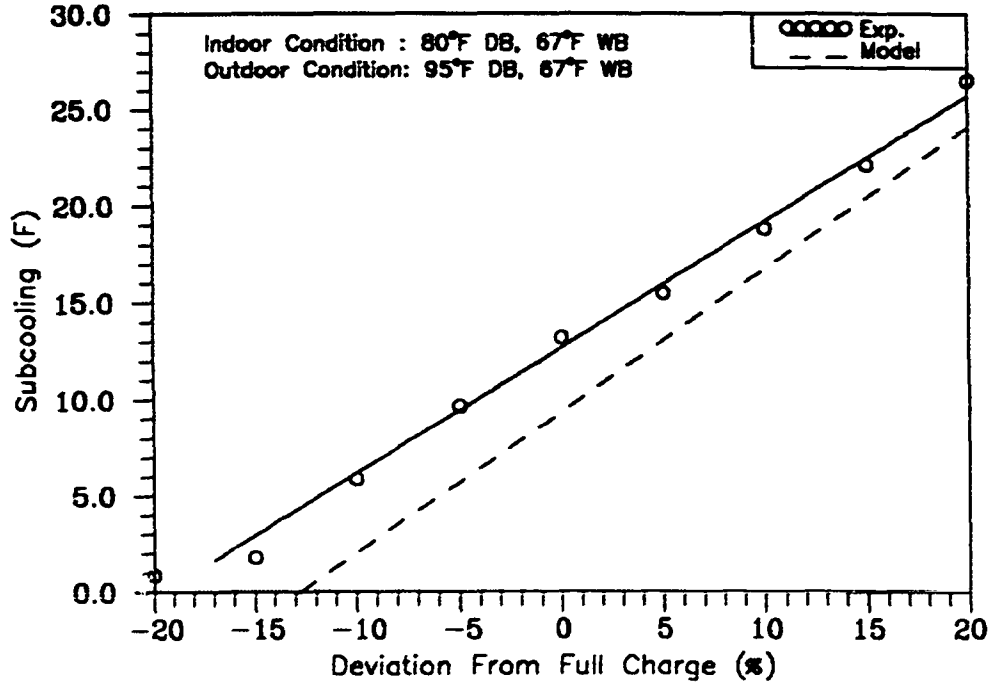

Figure 7.22 - Comparison of Subcooling at 95°F Outdoor Temperature for the TXV System

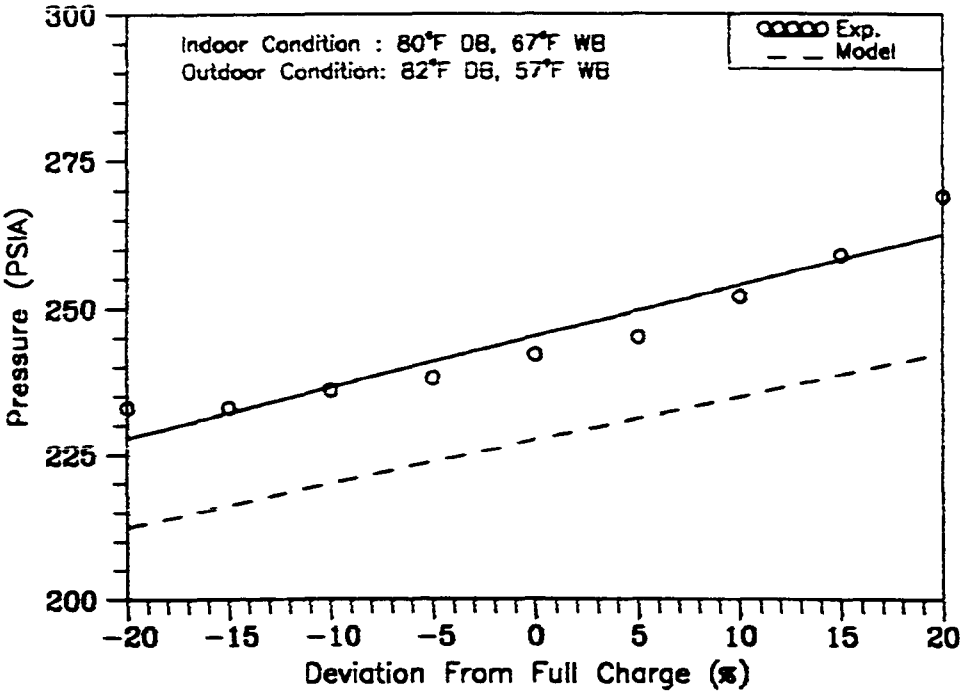

Figure 7.23 - Comparison of Condenser Pressure at 82°F Outdoor Temperature for the TXV System

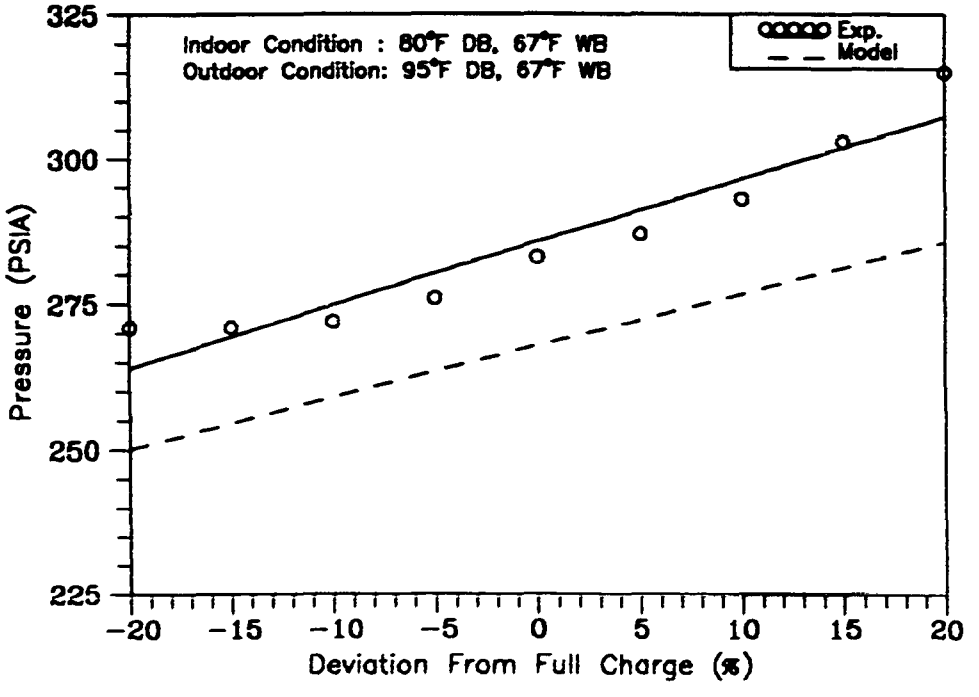

Figure 7.24 - Comparison of Condenser Pressure at 95°F Outdoor Temperature for the TXV System

for all the charging conditions.

The refrigerant flow rate predicted by the model was close to at 8 lbm/min for -20%, -15%, and -10% charging conditions at 82°F outdoor temperature (Figure 7.25). The experimental refrigerant flow rate was close to at 7.7 lbm/min for all the charging conditions. The predicted refrigerant flow rate increased from 8.0 lbm/min at -20% charging to 8.4 lbm/min +20% charging condition. The predicted and experimental refrigerant flow rates at 95°F outdoor temperature showed a similar trend to those at 82°F outdoor temperature (Figure 7.26). The predicted refrigerant flow rate was 4% higher than experimental result at -20% charging condition. As the charge in the system increased, the predicted flow rate increased to 8.4 lbm/min for +20% charging condition while the experimental flow rate was constant at 7.5 lbm/hr. One possible explanation for the increase in the predicted refrigerant flow rate might be related to the input TXV rated capacity. The TXV rated capacity increased slightly as the charge in the system increased. Normally, the superheat temperature is expected to increase as the outdoor temperature increases. To provide a constant superheat, the TXV would provide a smaller valve opening to restrict the refrigerant flow rate. As outdoor temperature increased from 82°F to 95°F, the predicted and experimental refrigerant flow rates decreased slightly (Figures 7.25 and 7.26). This was due to the TXV characteristic for controlling the refrigerant flow based on the constant superheat temperature of the unit.

The comparison of simulated total capacity with the experimental results at 82°F and 95°F outdoor temperatures are shown in Figures 7.27 and 7.28, respectively. The experimental and simulated capacities varied little with charge. The predicted capacities at 82°F and 95°F outdoor temperatures showed similar trends to the measured total capacities. At 82°F outdoor temperate, the predicted total capacity was higher than measured capacity by 4% for -20, -15, and -10% charging conditions. At full charge, the predicted total capacity peaked at 36.2 kBtu/hr and remained constant from +5% to

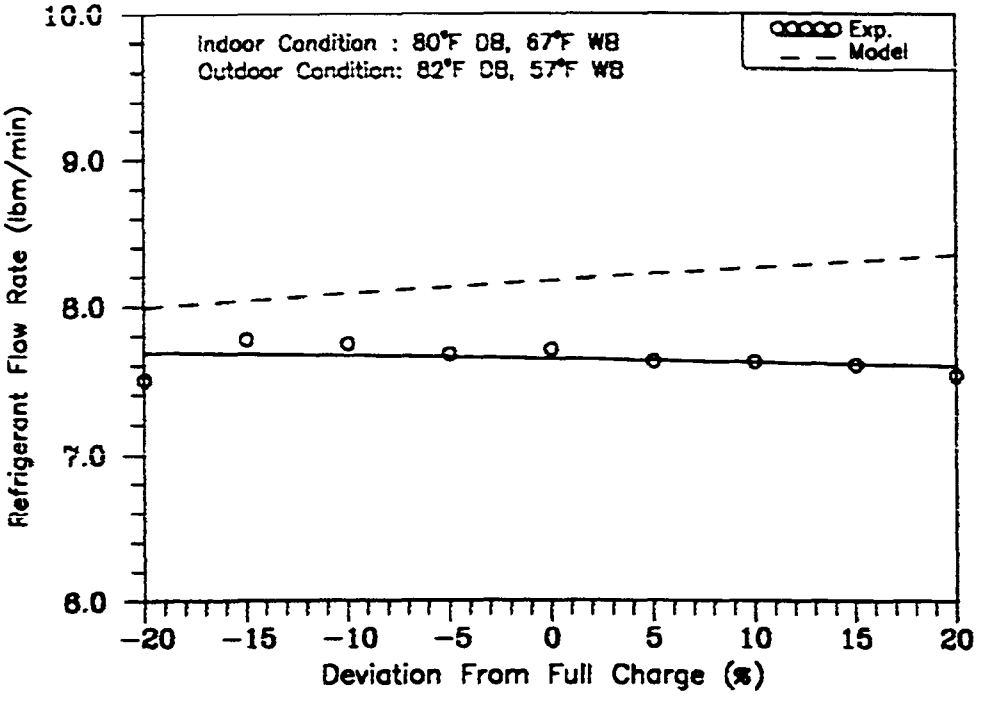

Figure 7.25 - Comparison of Refrigerant Flow Rate at 82°F Outdoor Temperature for the TXV System

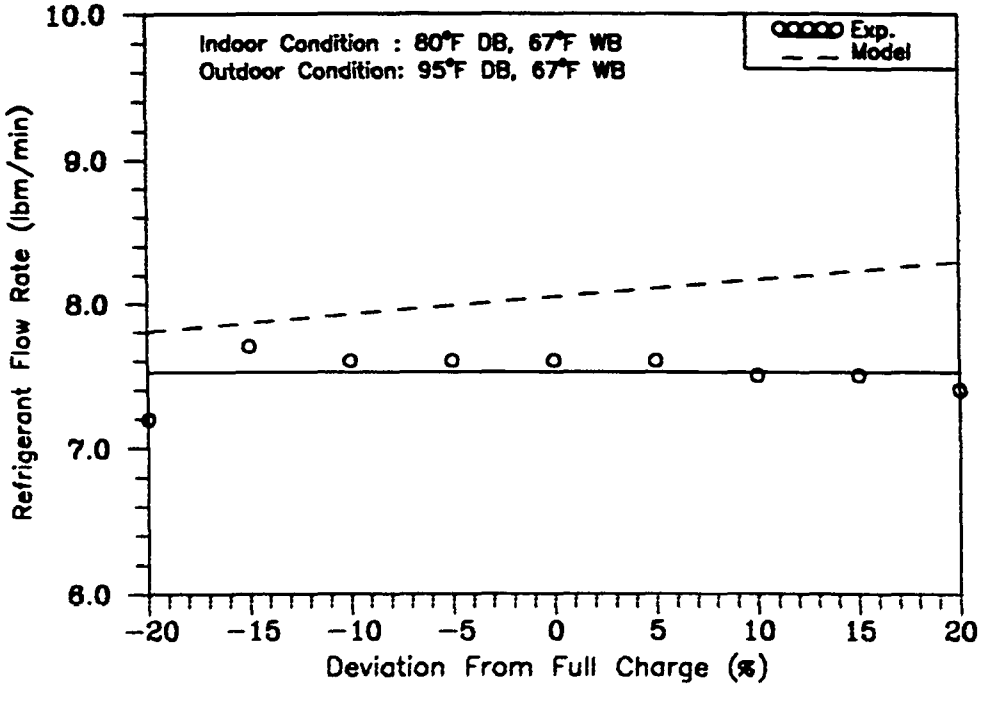

Figure 7.26 - Comparison of Refrigerant Flow Rate at 95°F Outdoor Temperature for the TXV System

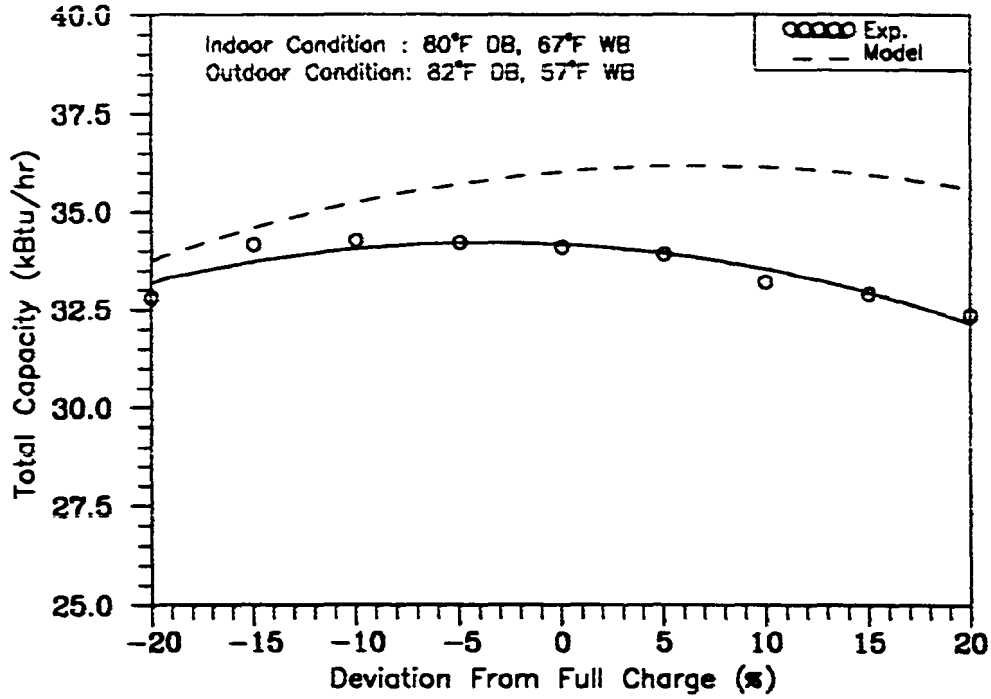

Figure 7.27 - Comparison of Total Capacity at 82°F Outdoor Temperature for the TXV System

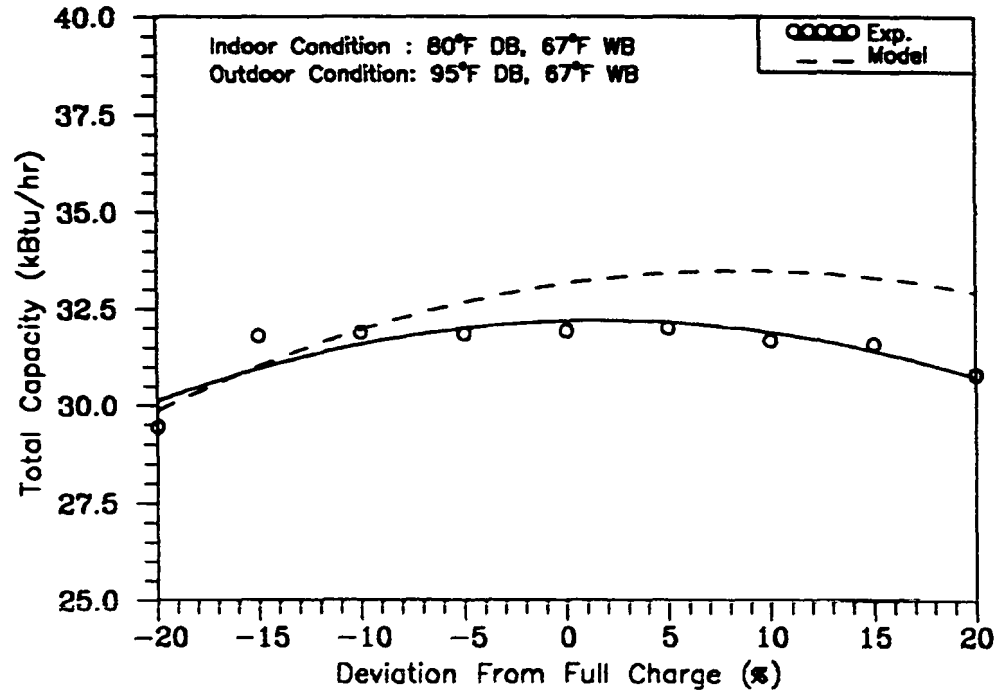

Figure 7.28 - Comparison of Total Capacity at 95°F Outdoor Temperature for the TXV System

+20% charging conditions. The predicted total capacity was within 1% for low-charge conditions at 95°F outdoor temperature (Figure 7.28). As the amount of charge in the system increased, the model predicted the capacity 3% and 6.5% higher than the experimental capacity at full charge and +20% charging conditions, respectively. The reason for the higher predicted capacity at high charging conditions was the high predicted refrigerant flow rates at those charging conditions for both outdoor temperatures.

The comparison of energy efficiency ratio (*EER*) for 82°F and 95°F outdoor temperatures are shown in Figures 7.29 and 7.30, respectively. At 82°F outdoor temperature, the predicted *EER* followed the experimental results very closely within 1% from -20% charging to full charge conditions. At 82°F outdoor temperature, the simulated *EER* peak occurred at full charge condition. As the amount of refrigerant charge in the system increased, predicted *EER* dropped to 10.2 which was within 6.4% of the measured *EER*. For 95°F outdoor temperature, the *EER* was predicted lower than experimental *EER* from -20% to +5% charging conditions. It was predicted 3% higher than experimental *EER* for +15% and +20% charging conditions. This comparison suggested that the predicted unit power consumption from -20% to +5% charging conditions was higher than the experimental power consumption at those charging conditions.

Short-Tube Orifice Expansion System

The comparison of superheat temperature between the simulated and experimental data for 82°F and 95°F outdoor temperatures are shown in Figures 7.31 and 7.32, respectively. At 82°F outdoor temperature, the predicted superheat was within 3°F of experimental superheat at the low-charge conditions. As the refrigerant charge in the system increased, the experimental and predicted superheat dropped linearly. The predicted data followed the experimental superheat very closely (less than 1°F) from full

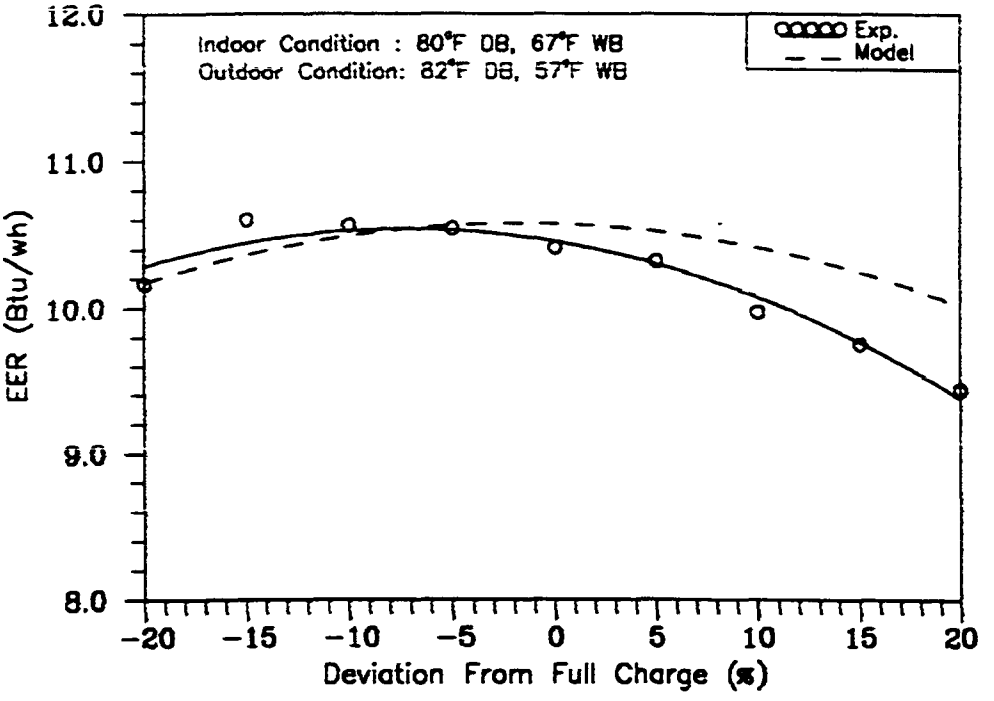

Figure 7.29 - Comparison of *EER* at 82°F Outdoor Temperature for the TXV System

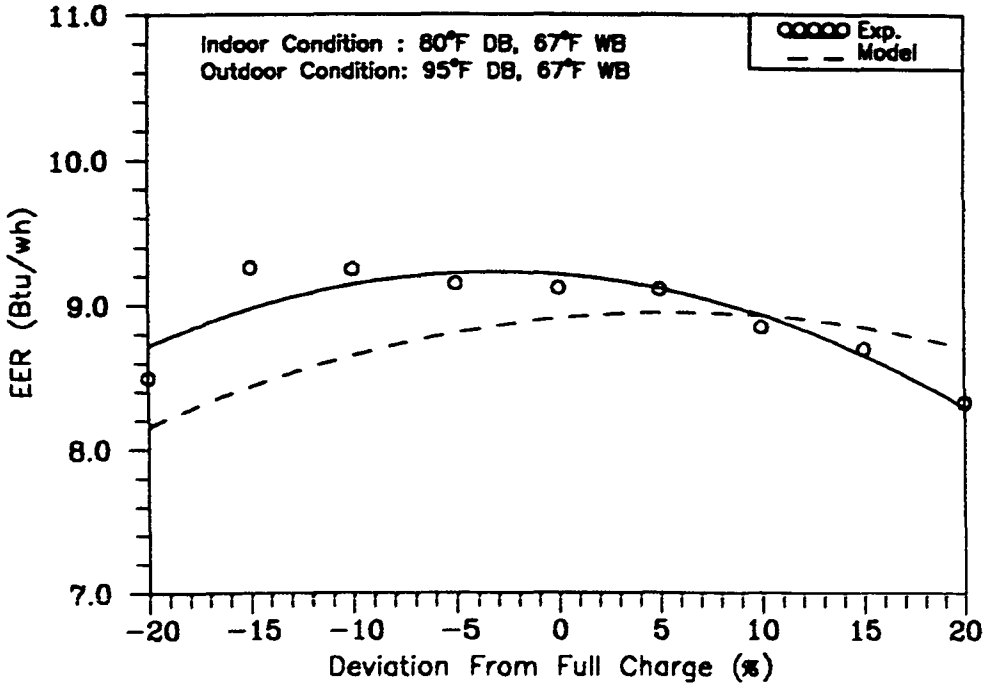

Figure 7.30 - Comparison of *EER* at 95°F Outdoor Temperature for the TXV System

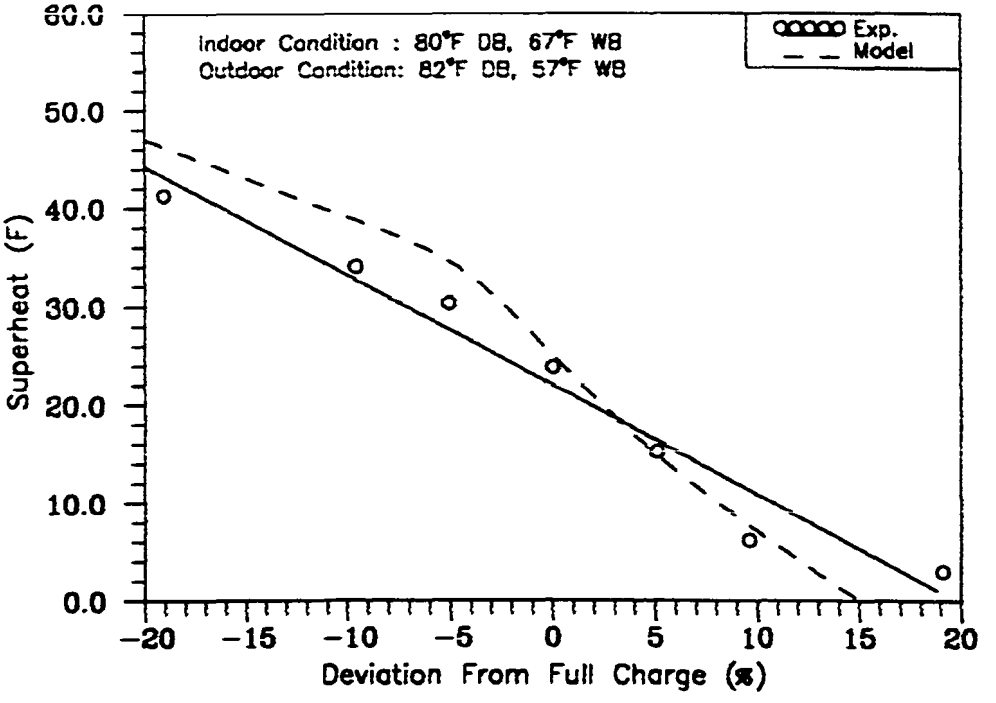

Figure 7.31 - Comparison of Superheat Temperature at 82°F Outdoor Temperature for the Short-Tube Orifice System

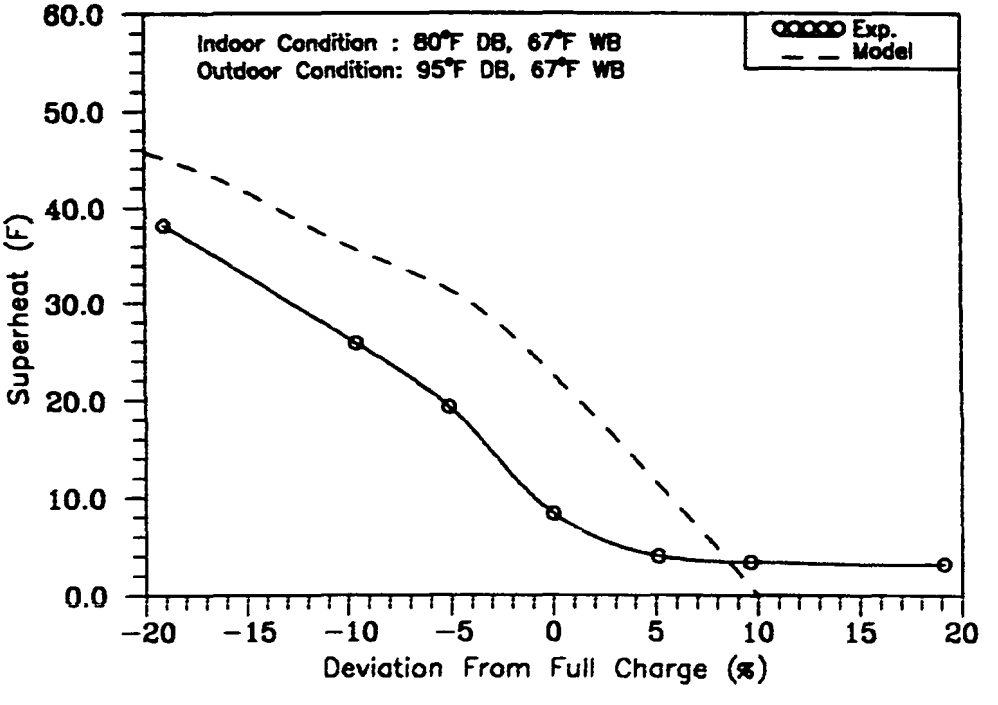

Figure 7.32 - Comparison of Superheat Temperature at 95°F Outdoor Temperature for the Short-Tube Orifice System

charge to +20% charging conditions. At 95°F outdoor temperature, the projected superheat was 10°F higher than the experimental superheat at -20% charging condition. As the refrigerant charge in the system increased, the simulated superheat decreased within 6°F and 4°F of the measured superheat for -5% and +5% charging conditions, respectively (Figure 7.32). The model predicted no superheat for +10, +15, and +20% charging conditions which were within 2°F of experimental results. The reason for the higher predicted superheat was the lower predicted evaporator pressure at 82°F and 95°F outdoor temperatures (Figures 7.33 and 7.34). Form -20% to full charging conditions, the evaporator pressure was predicted lower than measured pressure. As the refrigerant charge in the system increased, the difference between the predicted and measured evaporator pressure decreased from -10 psi at -20% charging to 1 psi at +20% charging conditions (Figure 7.33). At 95°F outdoor temperature, the difference between the predicted and measured evaporator pressure was higher than that at 82°F outdoor temperature.

The comparisons of subcooling temperature between the simulated and experimental data for 82°F and 95°F outdoor temperatures are showing similar trends in Figures 7.35 and 7.36, respectively. The model predicted zero subcooling temperature at -20% charging condition which was within 1°F of experimental subcooling at 82°F outdoor temperature. As the charge in the system increased, the predicted and experimental subcooling temperatures increased. The difference between the predicted and experimental subcooling temperature was 1°F at -20% charging and increased linearly to 7°F at +20% charging conditions. As outdoor temperature increased from 82°F to 95°F, the experimental and predicted subcooling temperatures were decreased at any given charging condition. For 95°F outdoor temperature, no subcooling temperature was predicted at -20% and -15% charging conditions. As the charge in the system increased, the difference between the predicted and experimental subcooling temperature

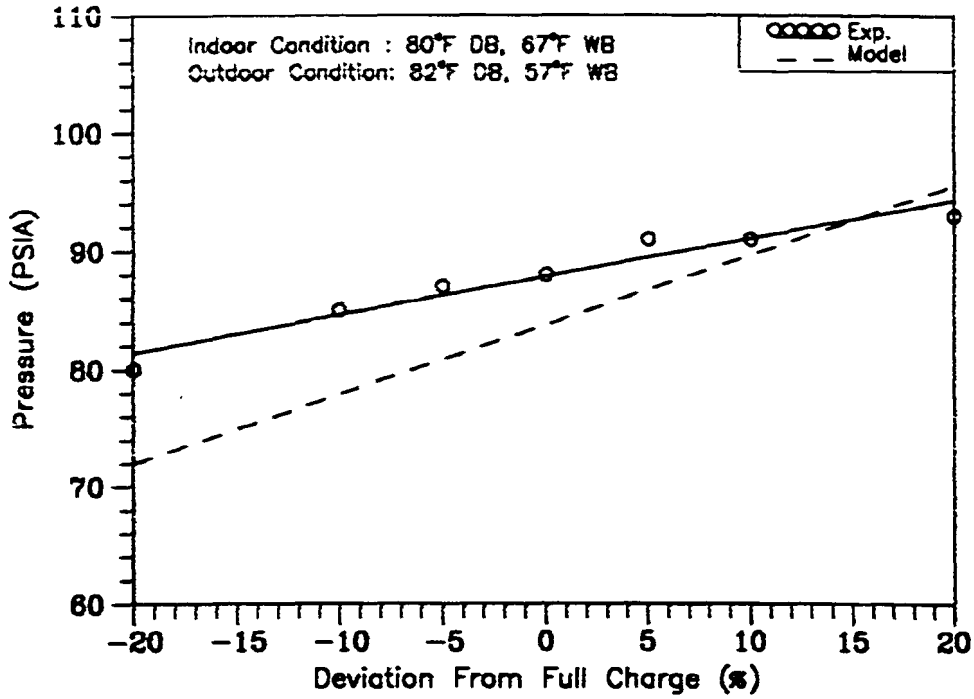

Figure 7.33 - Comparison of Evaporator Pressure at 82°F Outdoor Temperature for the Short-Tube Orifice System

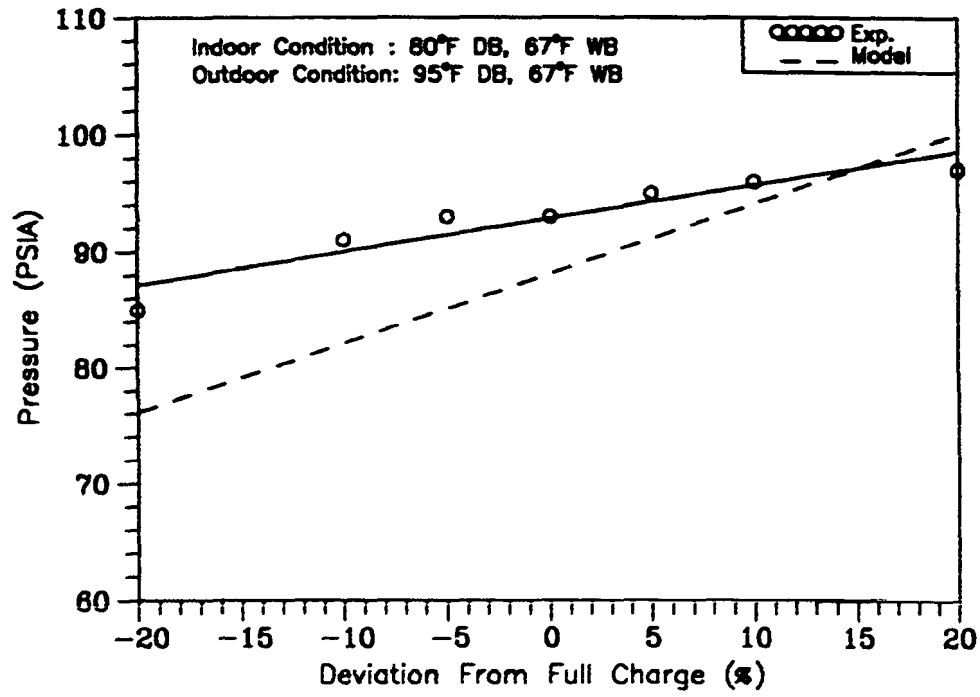

Figure 7.34 - Comparison of Evaporator Pressure at 95°F Outdoor Temperature for the Short-Tube Orifice System

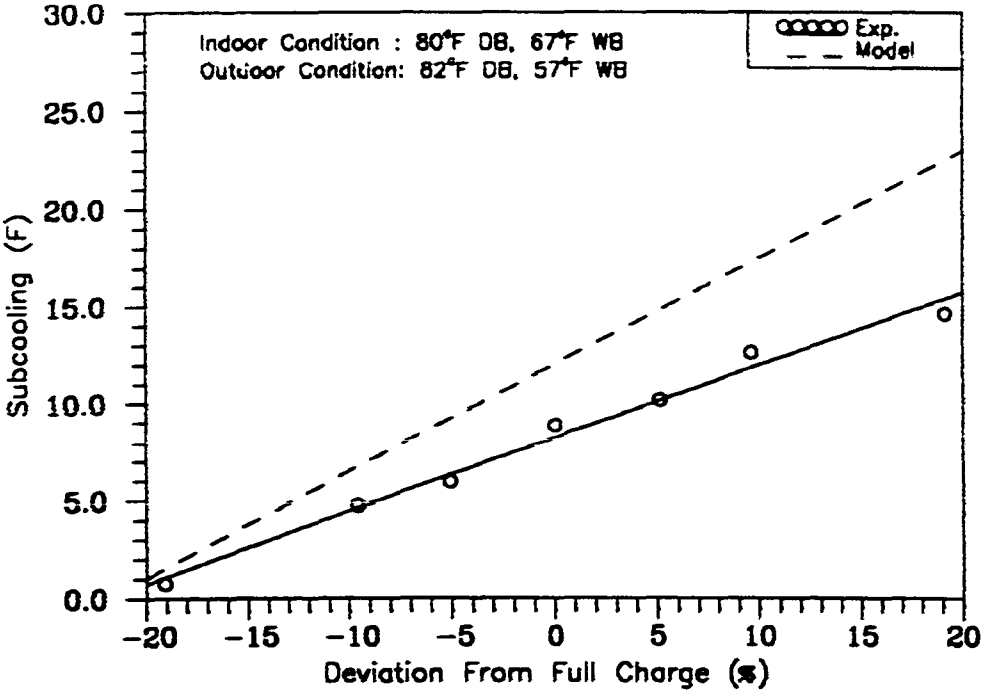

Figure 7.35 - Comparison of Subcooling at 82°F Outdoor Temperature for the Short-Tube Orifice System

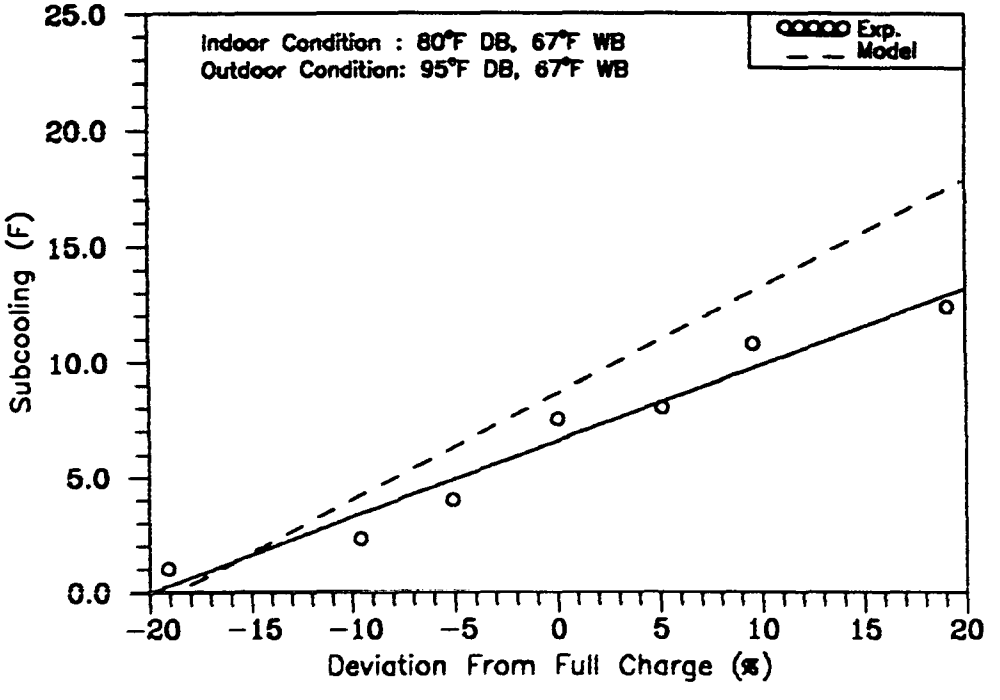

Figure 7.36 - Comparison of Subcooling at 95°F Outdoor Temperature for the Short-Tube Orifice System

was 1°F at -10% charging and increased linearly to 4°F at +20% charging conditions.

At 82°F outdoor temperature, the simulated system refrigerant flow rate followed the experimental data within 2% at +/-20% and +/-15% charging conditions (Figure 7.37). Form -10% to +10% charging conditions, the predicted refrigerant flow rate was within 1% of the measured refrigerant flow rates. As the outdoor temperature increased from 82°F to 95°F, the experimental and predicted refrigerant flow rates increased slightly at any given charge (Figure 7.38). The model predicted the refrigerant flow rate lower than the experimental flow rate by 4% at -20% and -15% charging conditions. As the refrigerant charge in the system increased, the predicted and experimental refrigerant flow rates were within 2%. The reason for the lower predicted refrigerant flow at 95°F outdoor temperature was the high predicted superheat temperature (Figure 7.32).

The comparison of simulated total capacity with the experimental results at 82°F and 95°F outdoor temperatures are shown in Figures 7.39 and 7.40, respectively. For 82°F outdoor temperature, the measured capacity peaked at +15% charging where the predicted capacity peaked between +5% and +10% charging conditions. The predicted and measured capacities were within 3% for -20%, -15%, -10%, and +20% charging conditions. From -5% to +15% charging, the predicted capacity was 5% higher than experimental capacity. At 95°F outdoor temperature, the experimental capacity was 30.5 kBtu/hr at -20% charging and increased to 32.0 kBtu/hr at full charge and remained constant through the rest of charging conditions. The simulated capacity showed a peak at +5% charging and dropped to 28.0 kBtu/hr and 31.0 kBtu/hr for -20% and +20% charging conditions, respectively (Figure 7.40). From -10% to +10% charging, the simulated and experimental capacities were within 1%. The predicted capacity showed a strong dependence on outdoor temperature and refrigerant charge. This behavior was similar to the behavior of the predicted capacity for the capillary tube expansion system (Figures 7.17 and 7.18).

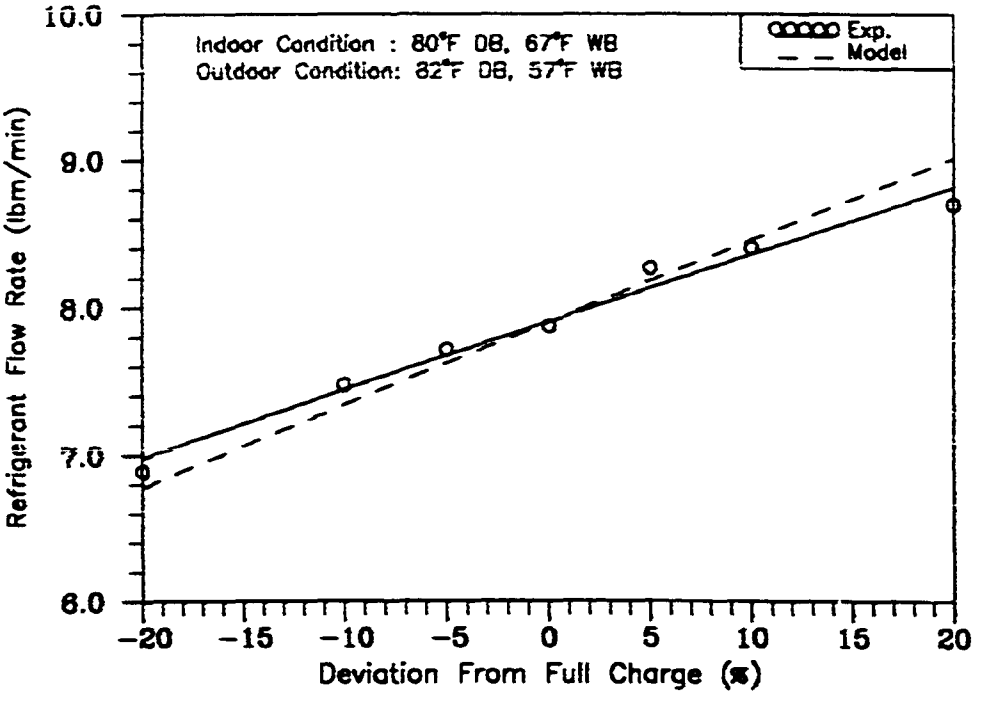

Figure 7.37 - Comparison of Refrigerant Flow Rate at 82°F Outdoor Temperature for the Short-Tube Orifice System

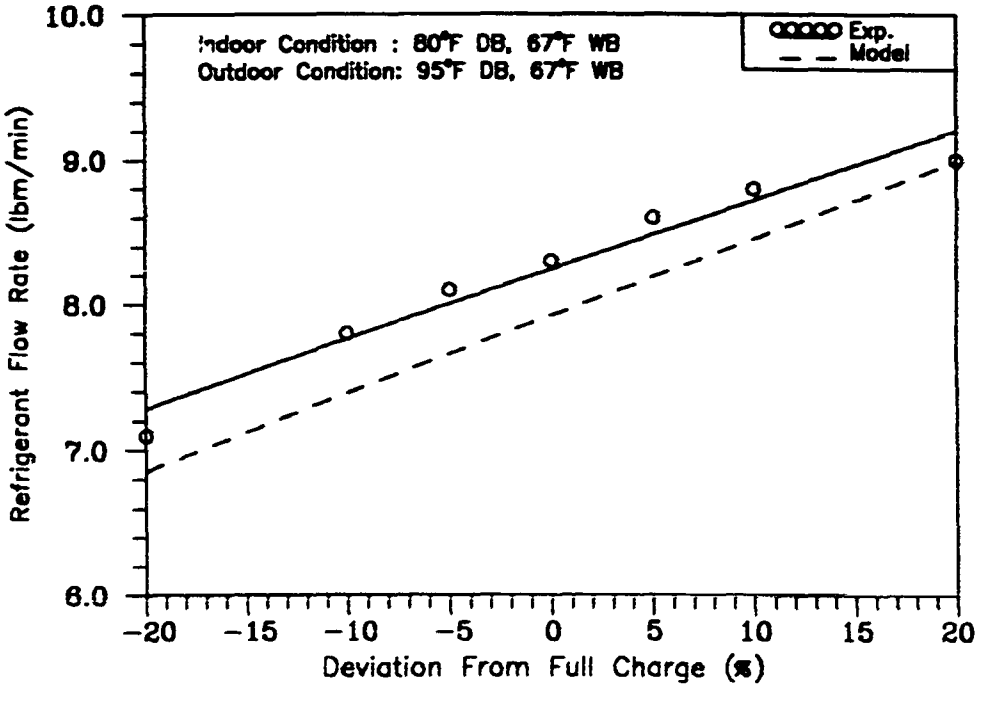

Figure 7.38 - Comparison of Refrigerant Flow Rate at 95°F Outdoor Temperature for the Short-Tube Orifice System

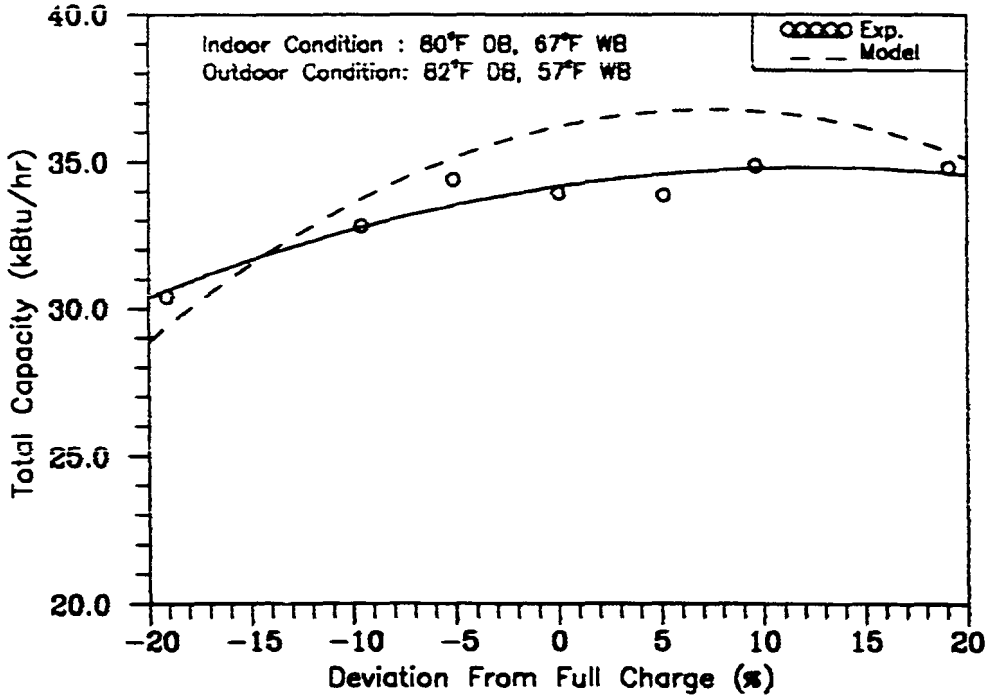

Figure 7.39 - Comparison of Total Capacity at 82°F Outdoor Temperature for the Short-Tube Orifice System

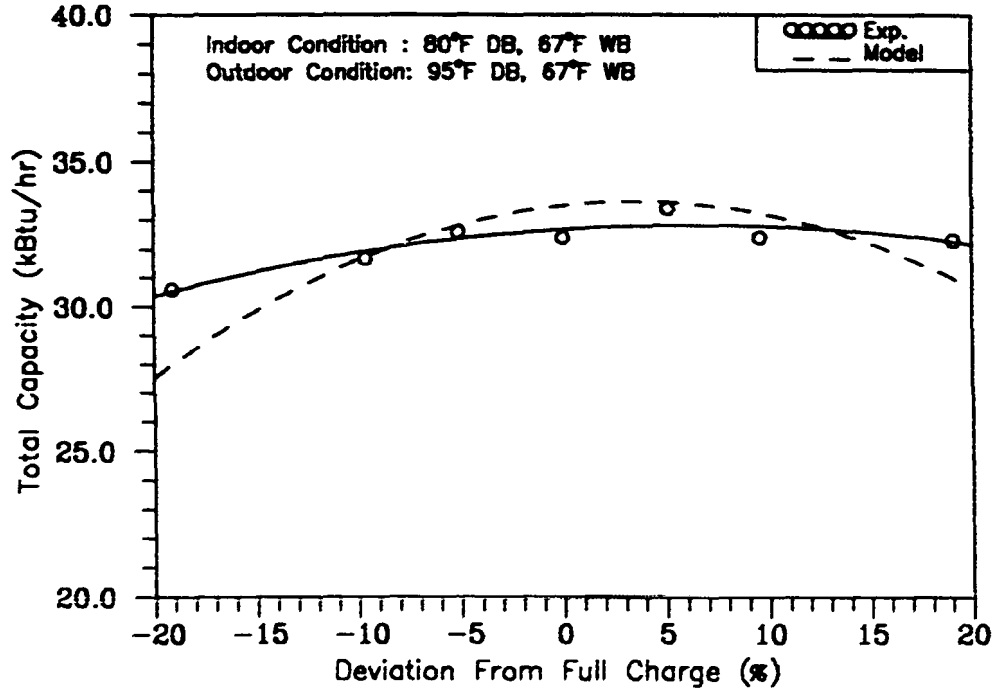

Figure 7.40 - Comparison of Total Capacity at 82°F Outdoor Temperature for the Short-Tube Orifice System

The trend of *EER* predicted by the model was very similar to the predicted total capacity. The comparison of *EER* for 82°F and 95°F outdoor temperatures are shown in Figures 7.41 and 7.42, respectively. At 82°F outdoor temperature, the experimental *EER* varied little with the refrigerant charge. The predicted *EER* peaked between the full charge and +5% charging conditions. The predicted and measured *EER*s were within 1% at -15%, -10%, and +20% charging conditions. At other charging conditions, the predicted *EER* was within 6% of experimental *EER* (Figure 7.41). As the outdoor temperature increased from 82°F to 95°F, the experimental *EER* showed a strong dependence on outdoor temperature but varied little with charge (Figure 7.42). The predicted and experimental *EER*s were within 1% from -10% to +10% charging conditions. The predicted *EER* was lower than experimental *EER* by 5% for -15%, +15%, and +20% charging conditions. The predicted *EER* showed a strong dependence on outdoor temperature and refrigerant charge. This behavior was similar to the behavior of the predicted *EER* for the capillary tube expansion system (Figures 7.19 and 7.20).

STEADY STATE DRY COIL TESTS

For the dry coil test, only steady state tests were simulated by the model. The model was incapable of simulating cyclic tests. The indoor wet bulb temperature was set low enough to insure no condensation would be removed by the evaporator.

For the capillary tube expansion system, the predicted capacity was 10% higher than measured capacity at -20% charging condition (Figure 7.43). As the refrigerant charge in the system increased, the difference between the predicted and measured capacity decreased to 1% at full charge condition. The predicted capacity followed the experimental results within 1% from full charge to +20% charging conditions. The predicted refrigerant flow rate was the possible reason for higher predicted capacity at -20, -15, and -10% charging conditions. The predicted refrigerant flow rate was 6% higher than measured refrigerant flow rate at -20% charging condition (Figure 7.44). As

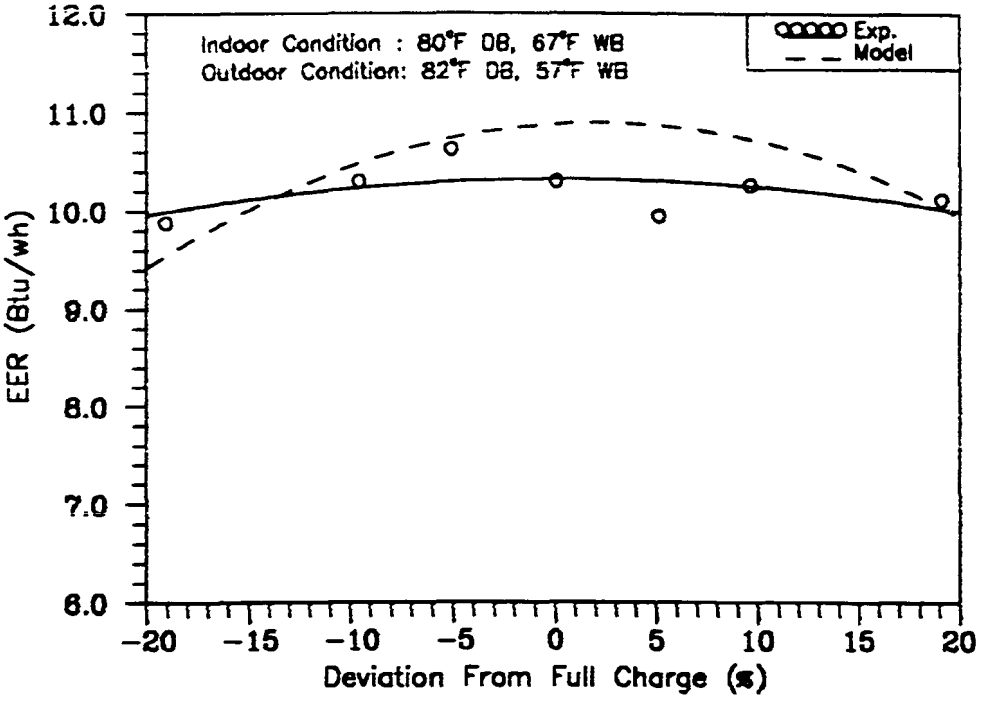

Figure 7.41 - Comparison of *EER* at 82°F Outdoor Temperature for the Short-Tube Orifice System

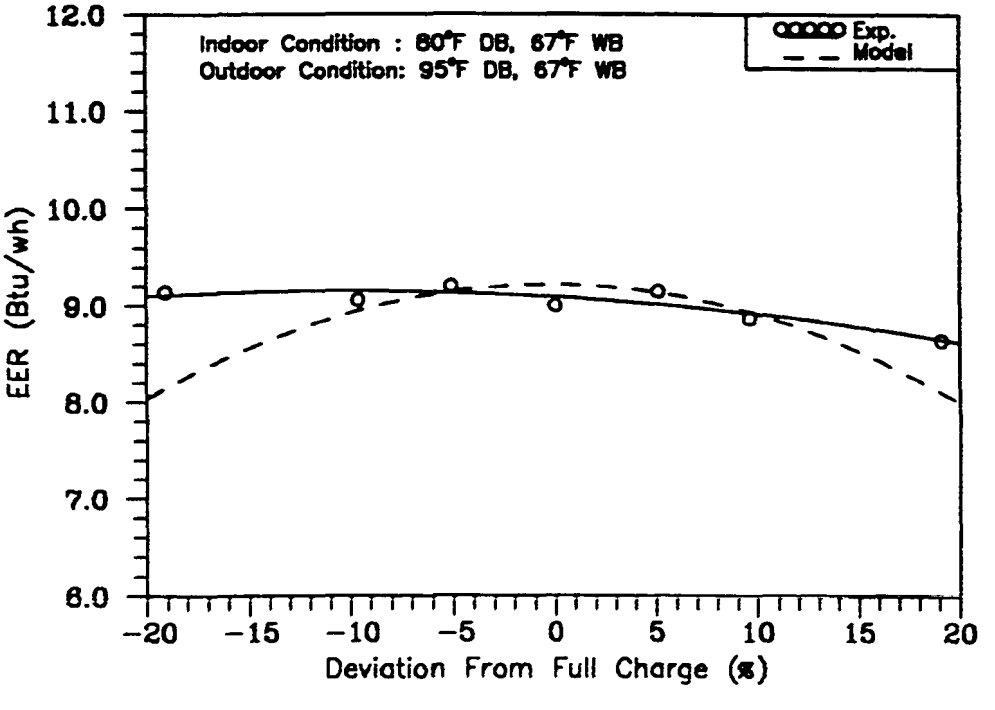

Figure 7.42 - Comparison of *EER* at 95°F Outdoor Temperature for the Short-Tube Orifice System

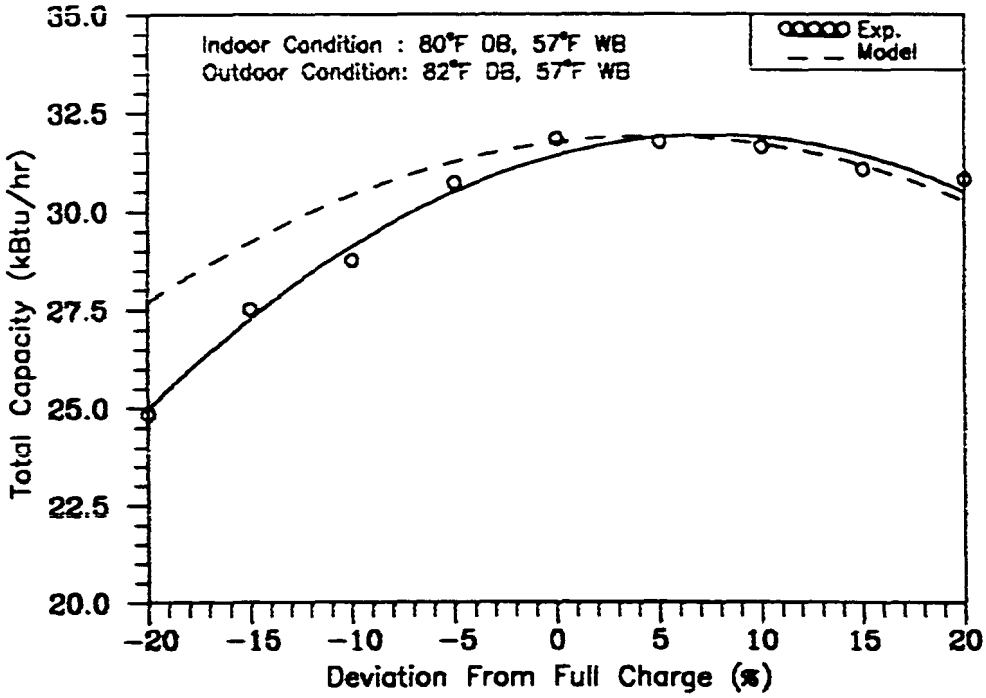

Figure 7.43 - Comparison of Capacity (dry-coil) for the Capillary Tube System

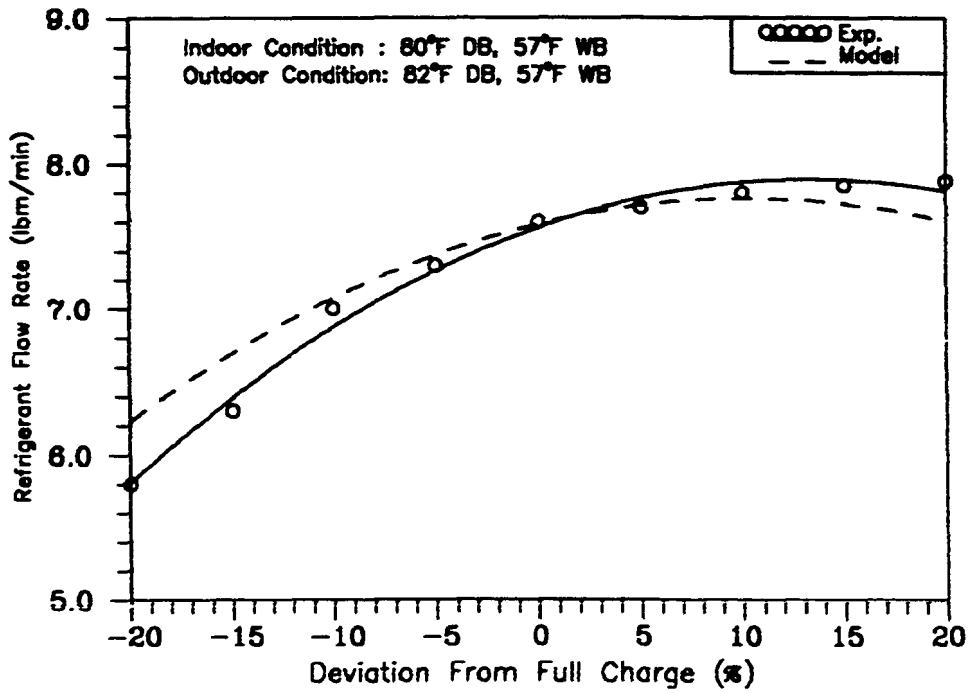

Figure 7.44 - Comparison of Refrigerant Flow Rate (dry-coil) for the Capillary Tube System

the charge in the system increased, the difference between the measured and predicted refrigerant flow rate decreased to less than 1% at full charge condition. The predicted *EER* shown in Figure 7.45 showed a similar trend to the predicted capacity at all the charging conditions. The predicted *EER* was within 8% at -20% charging condition and reached within 1% of the experimental *EER* at full charging condition. The predicted *EER* followed the experimental results within 1% from full charge to +20% charging conditions. The reason for the similar trend between the predicted *EER* and capacity was the precise prediction of the unit power consumption (Figure 7.46). The predicted power input was within less than 1% of measured power input at all the charging conditions.

The comparison of simulated total capacity with the experimental results for the TXV system is shown in Figures 7.47. The experimental and simulated capacity varied little with refrigerant charge. The predicted total capacity was higher than measured capacity by 8% for -20, -15, and -10% charging conditions. From full charge to +20% charging, the predicted capacity peak was within 17% of the measured capacity. The reason for the higher predicted capacity was the higher refrigerant flow rates predicted by the model (Figure 7.48). The simulated refrigerant flow rate was within 14% of the measured refrigerant flow rate at -20, -15, and -10% charging conditions (Figure 7.48). As the charge in the system increased, the predicted flow rate was within 8% of the measured data. From -20% to -5% charging conditions, the predicted *EER* was within 2% of the experimental *EER* (Figure 7.49). As the charge in the system increased, the predicted *EER* was within 6% of the experimental *EER* at +20% charging condition. The percent difference between the simulated and experimental *EER* was less than that of capacity. This was due to the higher predicted power input which was within 5% of the measured power at all the charging conditions (Figure 7.50).

For the short-tube orifice expansion system, the predicted capacity peaked at 32.6 kBtu/hr for the full charge condition and dropped to 28.0 and 31.0 kBtu/hr for -20% and

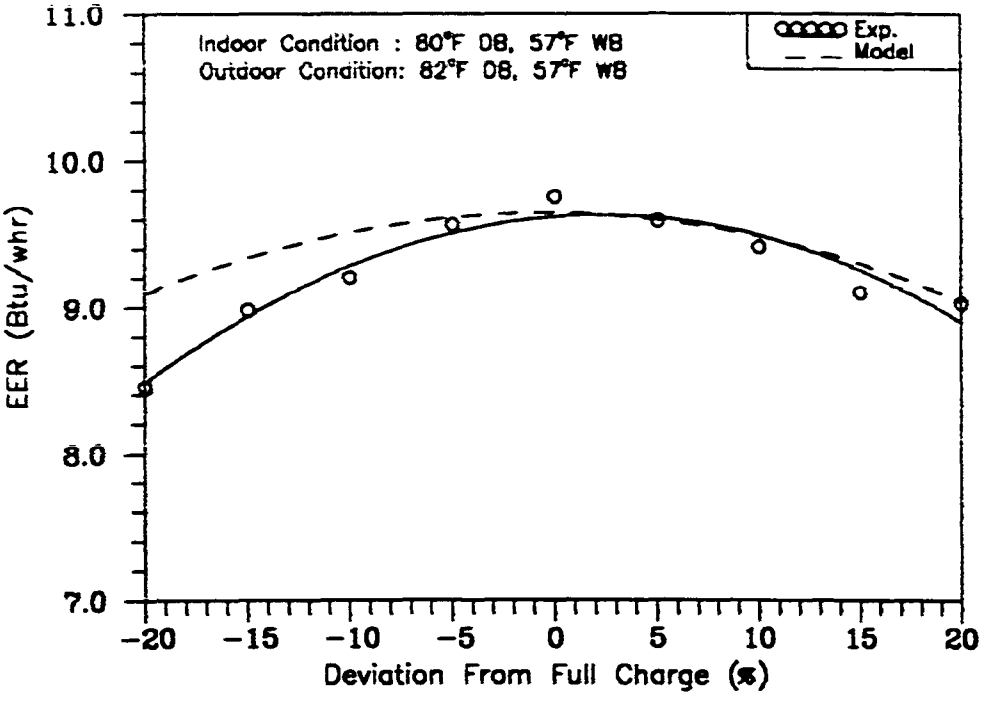

Figure 7.45 - Comparison of *EER* (dry-coil) for the Capillary Tube System

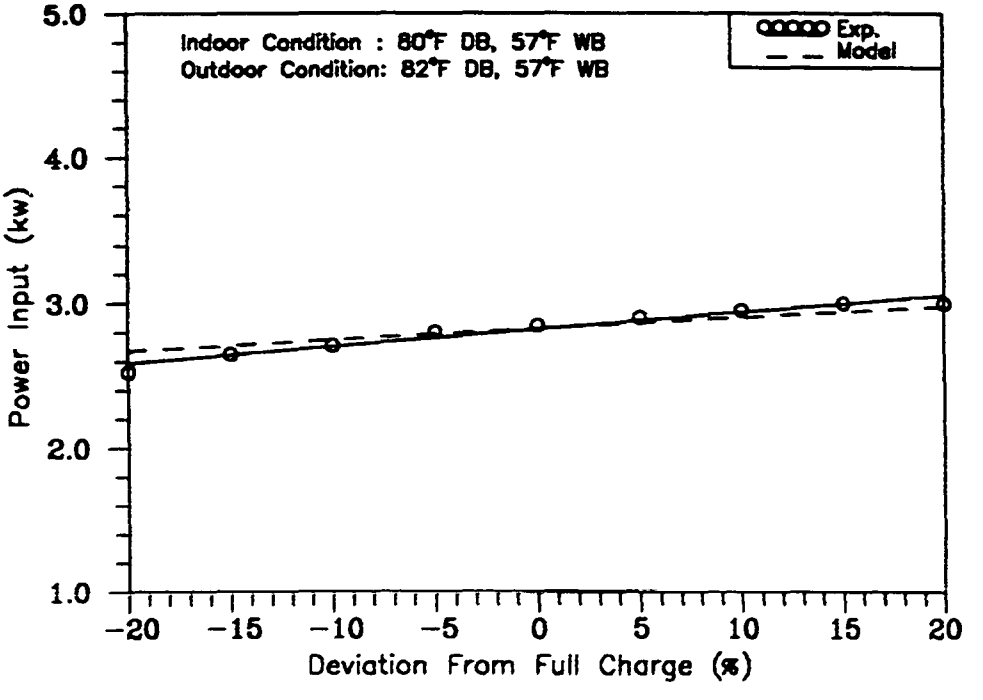

Figure 7.46 - Comparison of Unit Power Consumption (dry-coil) for the Capillary Tube System

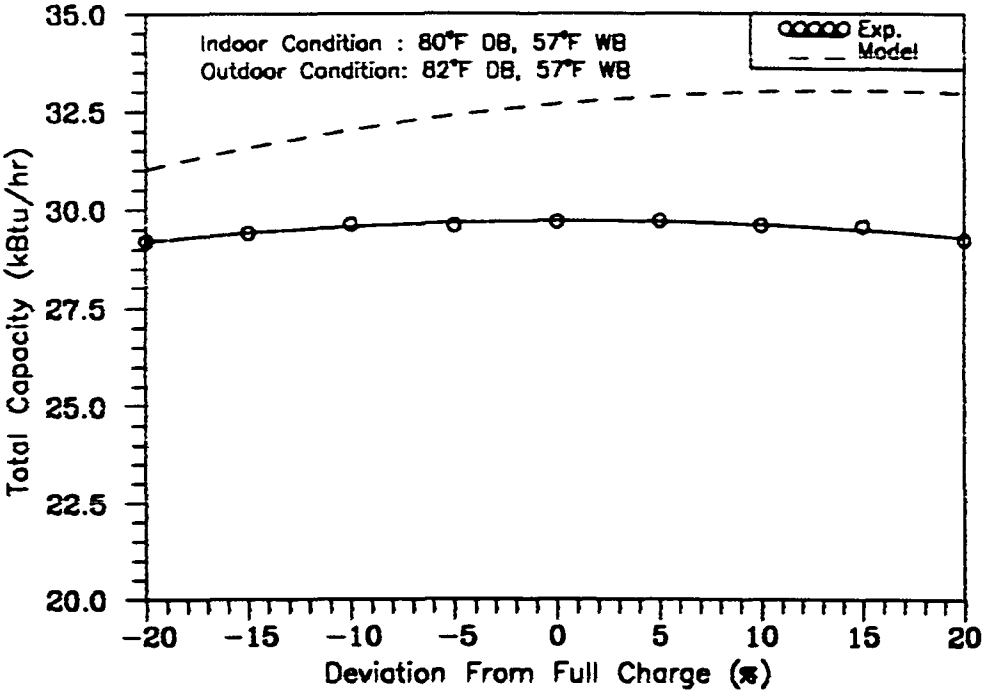

Figure 7.47 - Comparison of Capacity (dry-coil) for the TXV System

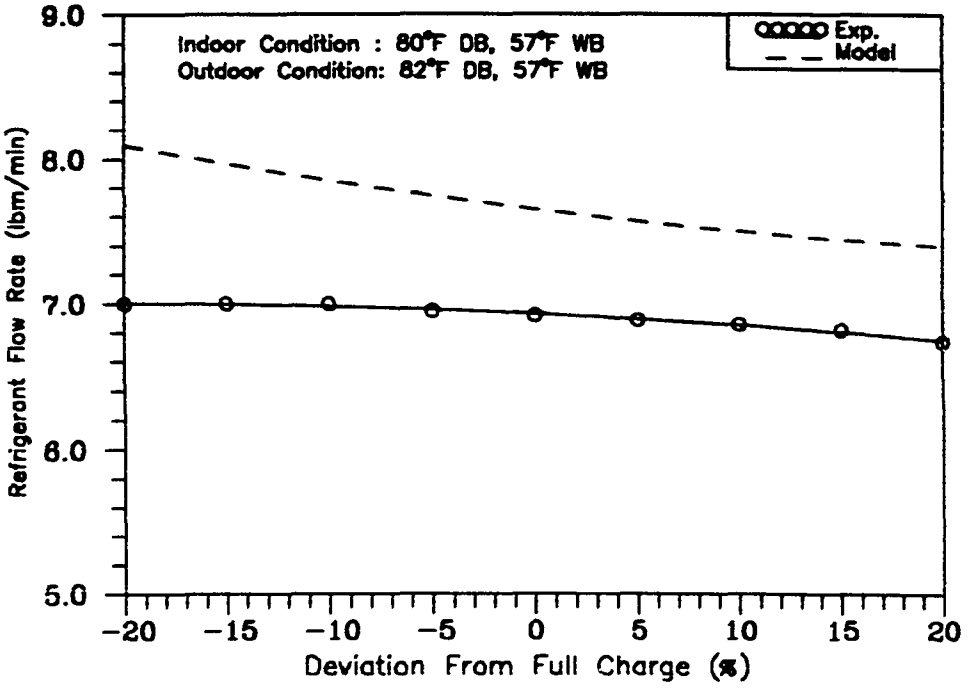

Figure 7.48 - Comparison of Refrigerant Flow Rate (dry-coil) for the TXV System

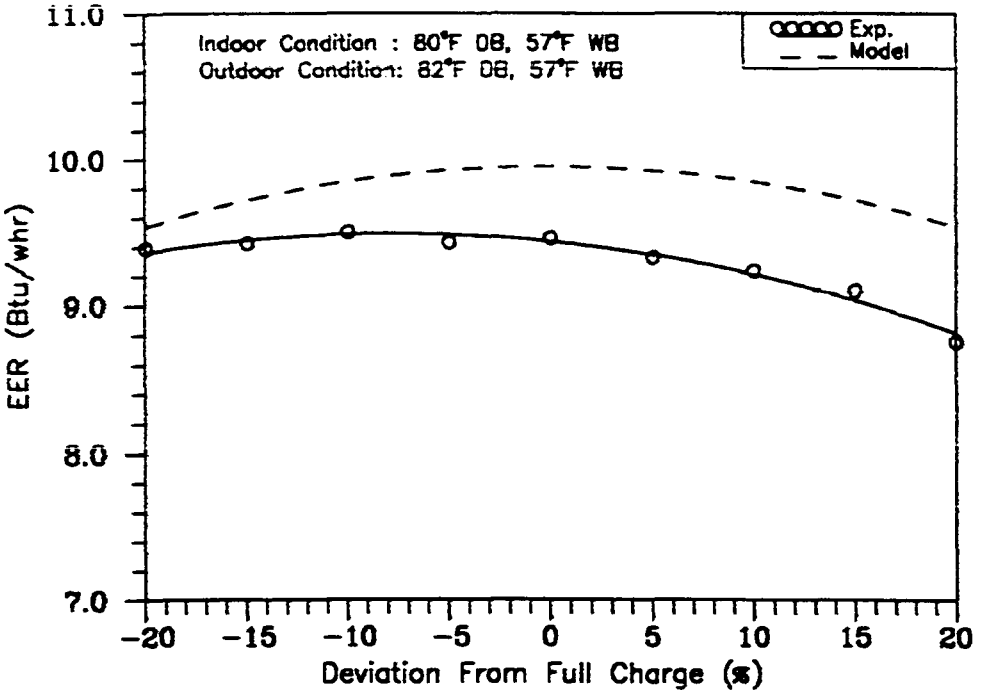

Figure 7.49 - Comparison of *EER* (dry-coil) for the TXV System

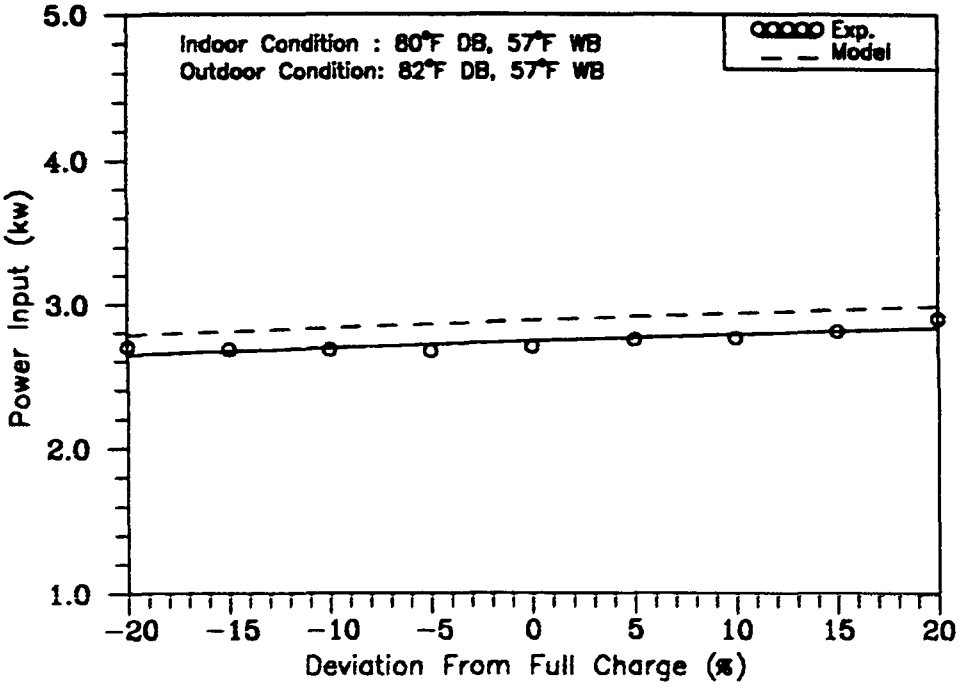

Figure 7.50 - Comparison of Unit Power Consumption (dry-coil) for the TXV System

+20% charging conditions, respectively. The predicted capacity was within 3% of the experimental capacity at +/-20% and +/-15% charging conditions (Figure 7.51). From -10% to +10% charging conditions, the predicted capacity was within 7% of the measured capacity. The possible reason for higher predicted capacity was the predicted superheat by the model. It was 30°F and 12°F higher than the measured superheat at -10% charging and full charge conditions, respectively (Figure 7.52). The predicted *EER* as shown in Figure 7.53 showed a similar trend to the predicted capacity. Like the predicted capacity, the predicted *EER* peaked at 10 Btu/wh for full charge and dropped to 9.2 Btu/wh for -20% and +20% charging conditions. The predicted *EER* was within 2% of the experimental *EER* at +/-20% and +/-15% charging conditions. From -10% to +10% charging conditions, the model predicted the *EER* within 9% of measured *EER*. The percent difference between the simulated and experimental *EER* and capacity was approximately the same. This was due to the close prediction of power input which was within 1% of the measured power at all the charging conditions (Figure 7.54).

Seasonal Energy Efficiency Ratio (*SEER*)

An important variable in the calculation of the *SEER* is the coefficient of degradation (C_D). This coefficient is a measure of the efficiency loss due to on/off cyclic of the system. The test procedures for central air conditioners and heat pumps [1979] prescribed two options for estimating the C_D: (i) from the cyclic dry coil test (D test) or (ii) assuming 0.25 for C_D. The ORNL model is a steady state simulation model and incapable of simulating the transient response (D test). Therefor, the C_D was assumed to be 0.25 for all the simulated runs. According to the test procedure, *SEER* is determined from the following:

$$PLF = 1 - 0.5\,(C_D) \tag{7.1}$$

$$SEER = PLF \cdot EER_B \tag{7.2}$$

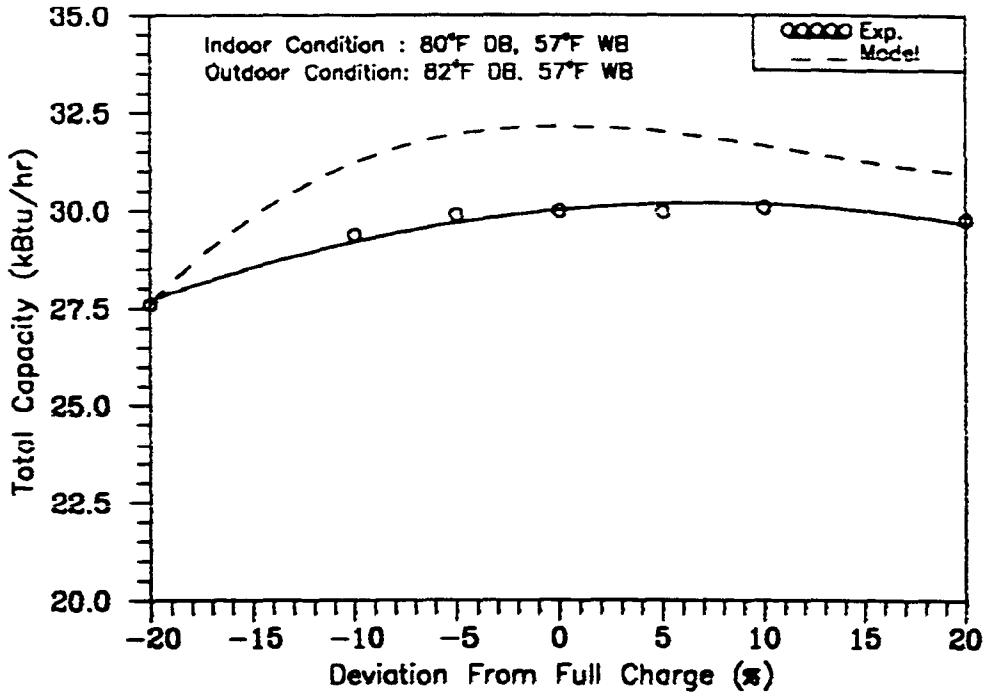

Figure 7.51 - Comparison of Capacity (dry-coil) for the Short-Tube Orifice System

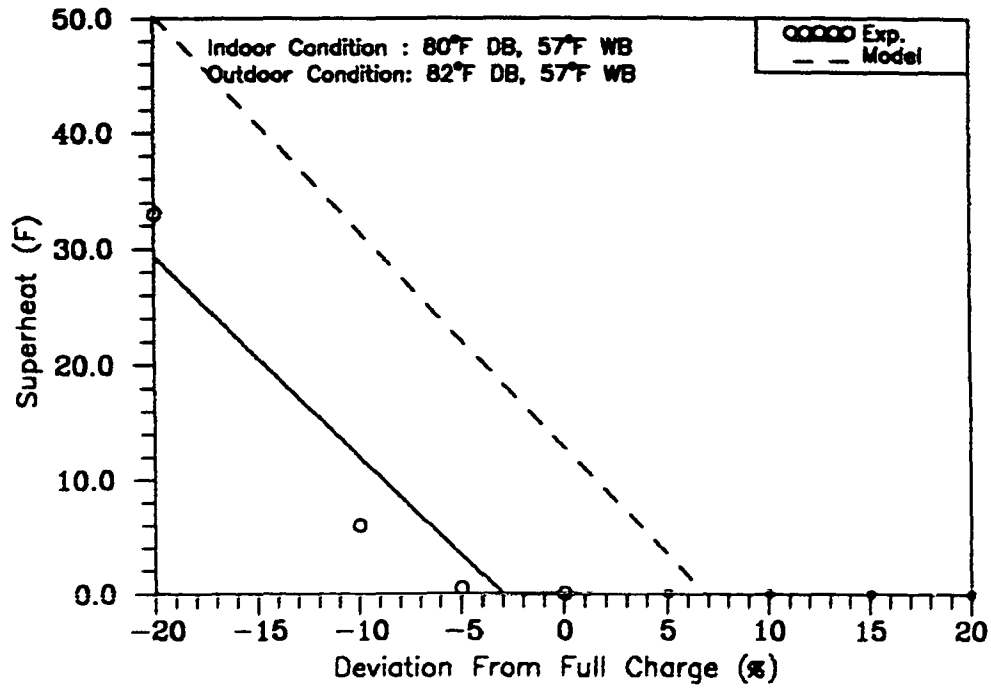

Figure 7.52 - Comparison of Superheat Temperature (dry-coil) for the Short-Tube Orifice System

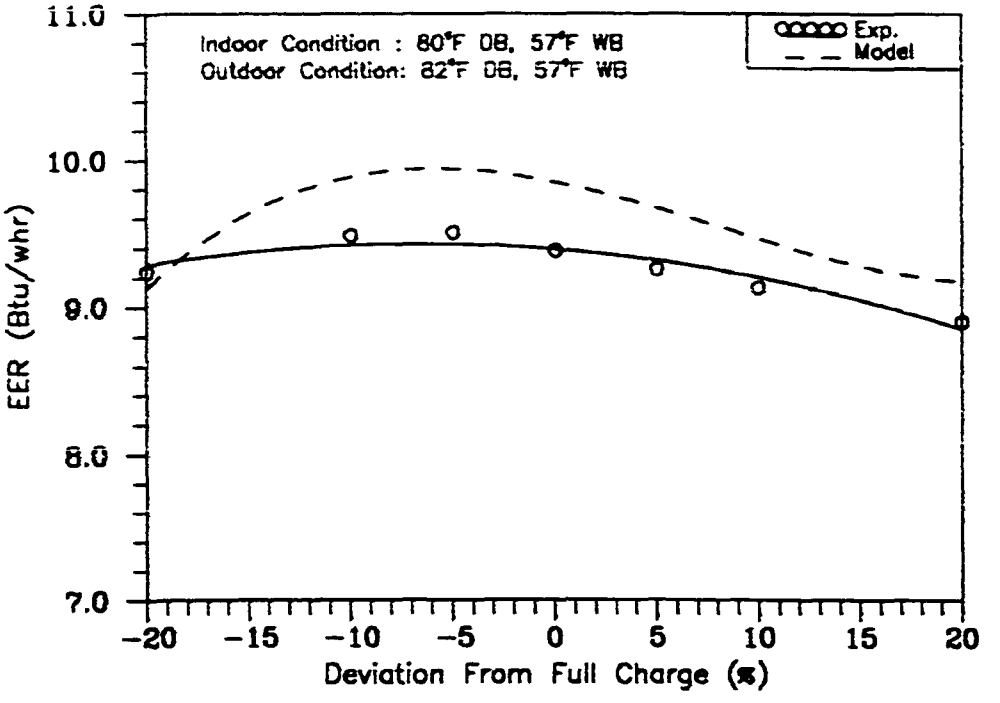

Figure 7.53 - Comparison of *EER* (dry-coil) for the Short-Tube Orifice System

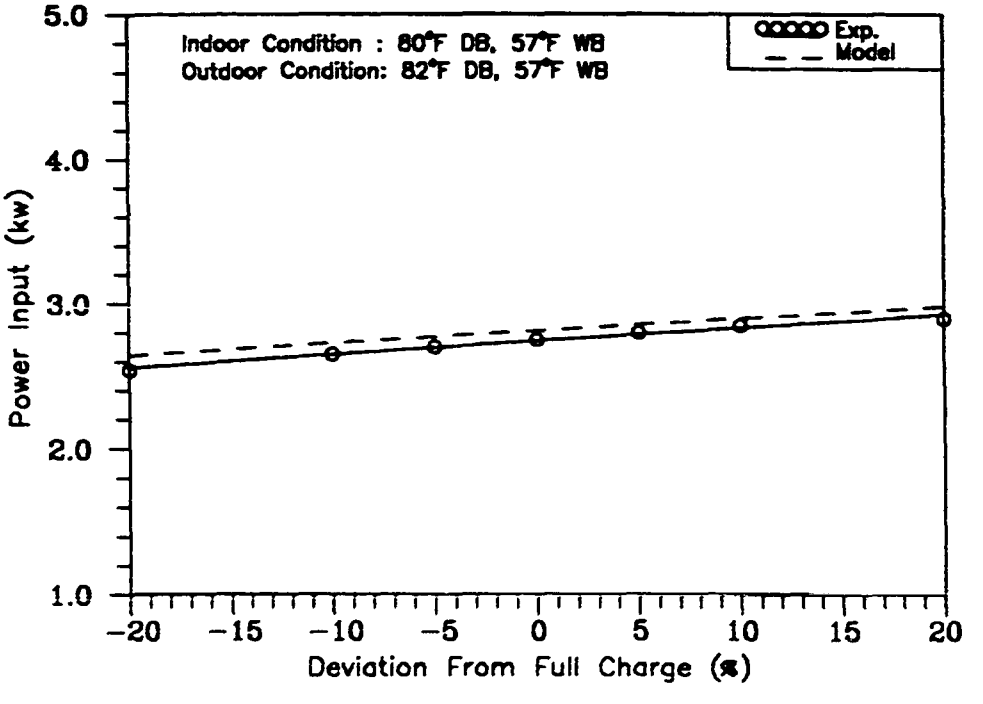

Figure 7.54 - Comparison of Unit Power Consumption (dry-coil) for the Short-Tube Orifice System

EER_B is the energy efficiency ratio for the steady state wet coil test at 82°F outdoor temperature.

The comparison of simulated *SEER* with the experimental results is shown in Figure 7.55 for the capillary tube expansion system. The predicted *SEER* showed a peak at full charge of 9.45. It dropped to 8.2 and 8.6 at -20% and +20% charging conditions, respectively. The simulated *SEER* was within 10% and 2% of experimental *SEER* at -20% charging and full charge conditions, respectively. As the charge in the system increased, the predicted *SEER* followed the experimental results within less than of 1%. The reason for the difference in predicted and experimental *SEER* was the coefficient of degradation (C_D). The experimental C_D varied from 0.255 to 0.175 with the refrigerant charge while the predicted C_D was assumed constant.

The simulated *SEER* showed little change with refrigerant charge for the TXV system (Figure 7.56). The predicted *SEER* was 6% lower than experimental *SEER* at -20% charging condition. As the charge in the system increased, the difference between the predicted and experimental *SEER* decreased to 3% and 1% at full charge and +20% charging conditions, respectively. The experimental C_D was fairly constant at 0.125 while the predicted C_D was assumed 0.25. This was a reason for the lower predicted *SEER*.

The comparison of simulated *SEER* with the experimental results is shown in Figure 7.57 for the short-tube orifice expansion system. The experimental *SEER* was constant at 9.4 for all the charging conditions except at -5% charging condition where it peaked to 9.9. The maximum predicted *SEER* occurred at +5% charging. It dropped to 8.2 and 8.5 at -20% and +20% charging conditions, respectively. This trend would suggest that the predicted *SEER* showed a strong dependence on refrigerant charge. From full charge to +10% charging condition, the predicted *SEER* was within 1% of the

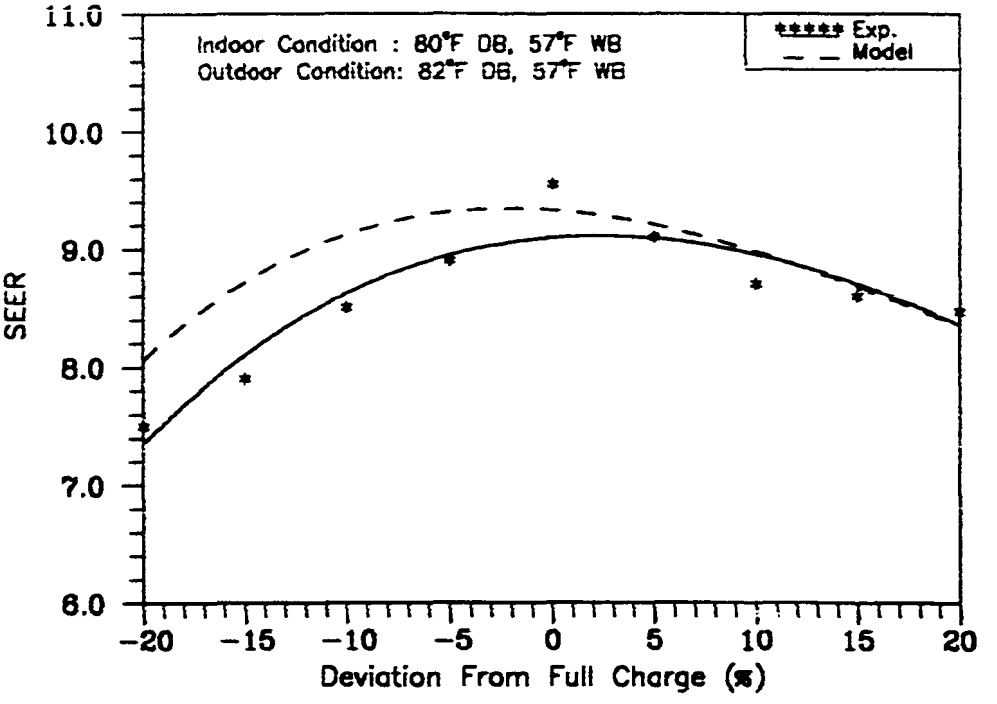

Figure 7.55 - Comparison of *SEER* for the Capillary Tube System

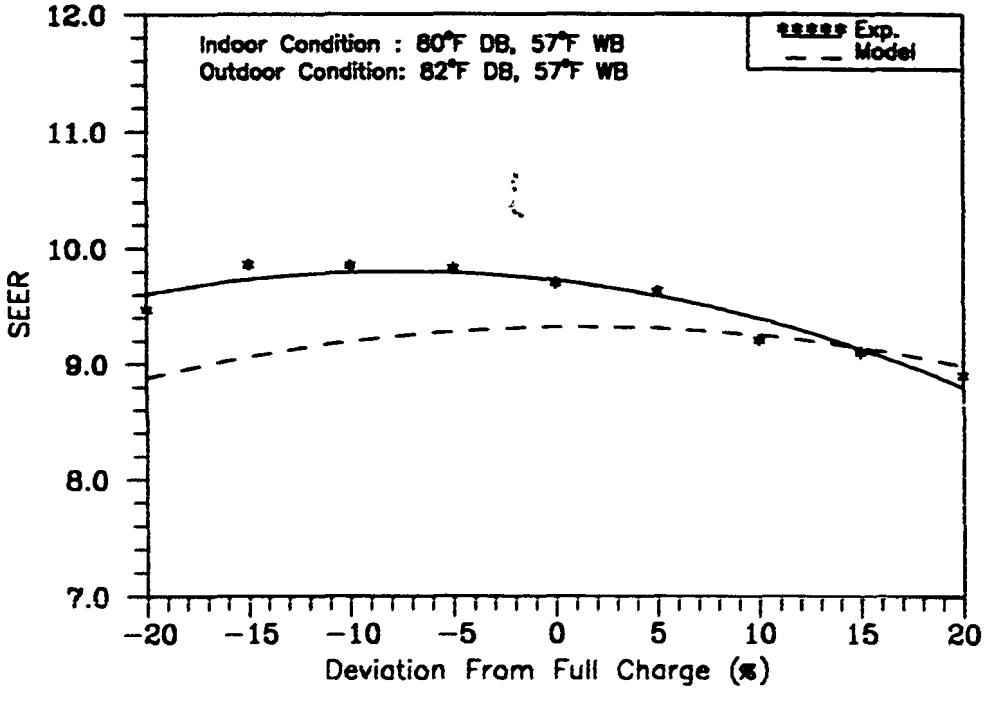

Figure 7.56 - Comparison of *SEER* for the TXV System

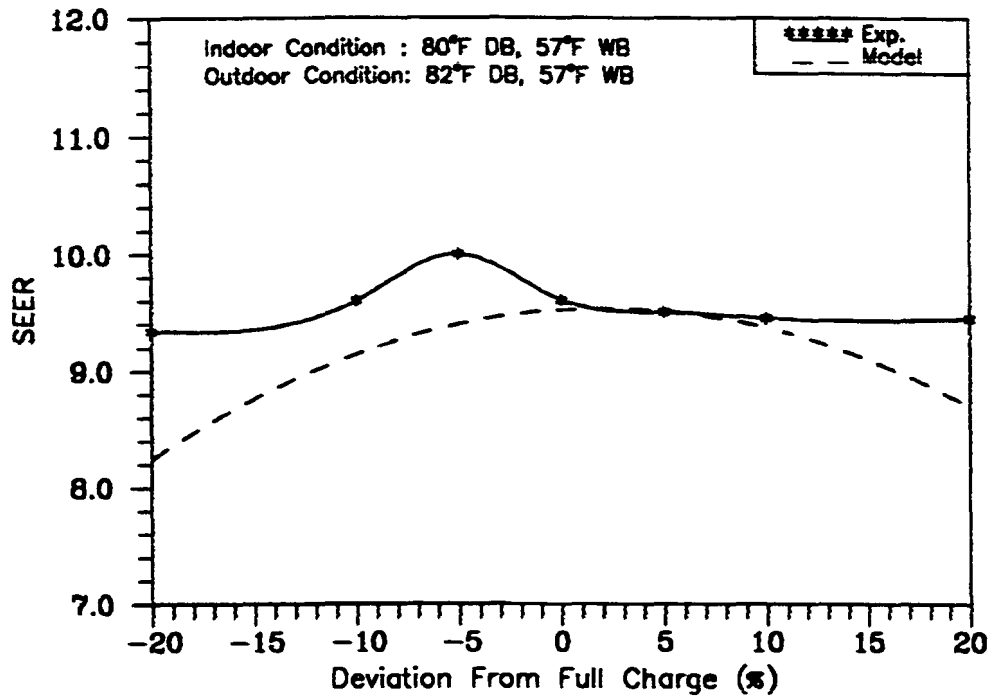

Figure 7.57 - Comparison of *SEER* for the Short-Tube Orifice System

experimental *SEER*. The simulated *SEER* was within 12% and 10% of experimental *SEER* at -20% and +20% charging conditions, respectively. A possible explanation for the lower predicted *SEER* was the higher assumed C_D where the experimental C_D was fairly constant at 0.115.

SUMMARY OF COMPARISON OF SIMULATED AND MEASURED RESULTS

The system capacity, refrigerant flow rate, superheat, and subcooling temperatures of capillary tube expansion system were compared with the experimental results for each void fraction at all charging conditions. The Hughmark void fraction model predicted the system parameters closest to the measured results among the void fraction models. Therefore, the Hughmark void fraction model was used in the present model to compare the simulated with the measured system performance variables.

The steady state simulation results from the present model, which was a modified version of the ORNL , were compared with the laboratory results at two outdoor temperatures. From -10% to +10% charging conditions, it was found that the predicted capacity and EER were within 2 to 5% of the laboratory results for the capillary tube expansion system. The model predicted the system performance up to 10% higher than measured results at +/-20% and +/-15% charging conditions. From -20% charging to full charge conditions, the predicted capacity and *EER* were within 2% of experimental results for the TXV system. As the charge in the system increased, the simulated capacity and *EER* were higher than measured results by 6%. For the short-tube orifice expansion system, the experimental capacity and *EER* varied little with charge, but showed a strong dependence on outdoor temperature. The predicted capacity and *EER* showed strong dependence on refrigerant charge and outdoor temperature.

The difference between the predicted and measured performance varied as much as 10% at some charging conditions. The reason for this difference was due to the

system energy balance between the refrigerant and air sides. The predicted performance variables were obtained from the refrigerant-enthalpy calculation where the experimental capacity and *EER* were based on the air-enthalpy calculation. From -10% to +10 charging conditions, the difference between the air side and refrigerant side capacity was within 3%. For the extreme off-design charging (+/-20% and +/-15%) conditions. the difference was approximately 7%.

CHAPTER VIII

CONCLUSIONS AND RECOMMENDATIONS

To characterize the effects of refrigerant charge on the performance of air conditioners, an experimental and analytical investigation was performed. The amount of refrigerant charge in the system was varied from -20% of full charge to +20% of full charge. For each charge, the air conditioner was subjected to a range of outdoor temperature (82° to 100°F) and three expansion devices (capillary tube, TXV, and short-tube orifice). Finally, the ORNL heat pump model was improved by replacing the existing heat exchanger model with one heat exchanger which simulated heat exchangers with tube-by-tube refrigerant flow through the coil. The steady state simulation results from the present model were compared with the laboratory results at two outdoor temperatures (82° and 95°F).

SUMMARY

This study illuminated several trends required to characterize the influence of charging and expansion devices on the system performance (Capacity, Power, *EER*, and *SEER*) of the test air conditioner. In the following sections, the effects of refrigerant charging on the system performance . re presented for each expansion device.

Capillary Tube Expansion System

The results of the experimentation showed that the capacity and *EER* decreased with increasing outdoor temperature for the full charge condition. The predicted capacity and *EER* were within 2% of the experimental results. One surprising result was the increase of the measured capacity for the low-charge conditions as compared to the full or high-charge conditions. For the low-charge tests, the experimental total capacity increased as the outdoor temperature increased. One possible explanation was in the changes of the refrigerant flow rate by the capillary tube for different charging

conditions. However, this behavior was not predicted by the model. As the outdoor temperature increased, the predicted capacity decreased too for low-charge conditions. From -10% to +10% charging, it was found that the predicted capacity and *EER* were within 2 to 5% of the laboratory results. The model predicted the system performance up to 10% higher than measured results at +/-20% and +/-15% charging conditions.

As the outdoor temperature increased, the predicted and measured superheats decreased. The simulated superheat was within 3°F of measured superheat. The model predicted a saturation state at the outlet of the evaporator for +15% and 20% charging conditions where it was validated by the experimental results. The predicted and measured refrigerant flow rates showed strong dependence on the refrigerant charge and outdoor temperature. As the charge and outdoor temperature increased, the predicted and measured refrigerant flow rates increased. The predicted refrigerant flow rate followed the measured data within 2% for 95°F outdoor temperature.

In general, the degradation of performance was larger for low-charge than that for high-charge conditions. The measured *SEER* dropped 21% and 11% as compared to the full charge test for -20% and +20% charging conditions, respectively. The experimental results suggested that a capillary expansion device would be extremely sensitive to changes in refrigerant charge and outdoor temperature. The simulated *SEER* was within 10% and 2% of experimental *SEER* at -20% charging and full charge conditions, respectively. As the charge in the system increased, the predicted *SEER* followed the experimental results within less than of 1%.

Thermal Expansion Valve System

The experimental capacity and *EER* decreased as the outdoor temperature increased. They were approximately constant over a wide range of charging (-15% to +10%) for a given outdoor temperature. The degradation of performance was larger for

the extreme off-design charging (-40% and -30%) than other charging conditions. The predicted capacity and *EER* were within 1% to 3% of the experimental capacity and *EER* at the low-charge conditions. As the charge in the system increased, the model predicted the capacity and *EER* 6.5% and 3% higher than experimental results, respectively.

The TXV maintained a relatively constant superheat by regulating the refrigerant flow rate in the system. The measured refrigerant flow rate was constant at 7.7 lbm/min for all the charging conditions where the predicted flow rate increased from 8 lbm/min at -20% charging to 8.4 lbm/min at +20% charging conditions for 82°F outdoor temperature. The relatively constant refrigerant flow rate would explain why the capacity remained relatively constant from -15% to 10% charging conditions. The predicted and experimental refrigerant flow rates at 95°F temperature showed a similar trend to those at 82°F outdoor temperature.

The measure of seasonal performance, *SEER*, peaked between -10% and -5% charging rather than manufacturer suggestion (full charge). The experimental *SEER* dropped only 3% from 9.7 at full charge for -20% charging while dropping 8% for +20% charging condition. The simulated *SEER* showed little change with the refrigerant charge and it was within 6% of the experimental *SEER* at -20% charging condition. As the charge in the system increased, the difference between the predicted and experimental *SEER* decreased to 3% and 1% at full charge and +20% charging conditions, respectively.

Short-Tube Orifice Expansion System

The effect of outdoor temperature was much noticeable on the measured capacity and *EER* at high-charge than low-charge conditions. The measured capacity and *EER* showed strong dependence on outdoor temperature, but varied little with charge. For 82°F outdoor temperature, the measured capacity and *EER* peaked at +15% charging

where the predicted capacity and *EER* peaked between +5% and +10% charging conditions. From -10% to +10% charging, the simulated capacity and *EER* were within 1% of measured capacity and *EER* at 95°F outdoor temperature. The predicted capacity and *EER* were lower than measured results by 5% for -15% and +20% charging and 10% for -20% charging conditions. This comparison would suggest that the predicted capacity and *EER* showed strong dependence on outdoor temperature and refrigerant charge. This behavior was similar to the behavior of the predicted capacity and *EER* for the capillary tube expansion system. However, the experimental capacity and *EER* showed little dependence on refrigerant charge which contrasts quite dramatically with the behavior of the capillary tube expansion system.

The short-tube orifice expansion system superheat followed the measured results closely. The predicted superheat was within 3°F of measured superheat at the low-charge conditions for 82°F outdoor temperature. From full charge to +20% charging, the predicted data followed the experimental superheat very closely (less than 1°F). The simulated system refrigerant flow rate followed the experimental data within 1 to 2% from -20% to +20% charging conditions.

The experimental *SEER* peaked at 9.9 for -5% charging below the manufacturer's suggestion (full charge). It decreased to 9.3 for both +20% and -20% charging conditions. This trend suggested that the effect of refrigerant charge on the *SEER* was not as dramatic as the capillary tube expansion system. The maximum predicted *SEER* occurred at 9.45 of +5% charging. It dropped to 8.2 and 8.5 at -20% and +20 charging conditions, respectively. This behavior would suggest that the predicted *SEER* was similar to that of the system with capillary tube.

CONCLUSIONS

The capillary tube expansion system is extremely sensitive to changes in

refrigerant charge and outdoor temperature. In general, the degradation of performance is larger for low-charge than high-charge conditions.

Because the TXV maintains a relatively constant superheat and refrigerant flow rate, the total capacity, *EER*, and *SEER* show a small variation with the refrigerant charge. However, the performance variables show a strong dependence on the outdoor temperature. The results from the study on the capillary tube expansion system suggested that a fixed expansion device would be extremely sensitive to changes in refrigerant charge. For instance, a 10% reduction in charge would result in 11.5% reduction in the *SEER* for the system with capillary tube. However, the same condition would lead to 1.5% increase in the *SEER* for the TXV system.

The total capacity and *EER* for the short-tube orifice expansion system show little dependence on the refrigerant charge which contrasts quite dramatically with the behavior of the capillary tube expansion system. However, like the capillary tube expansion system, the total capacity and *EER* show a strong dependence on the outdoor temperature. In general, the degradation of performance is much smaller for the short-tube orifice expansion system than the capillary tube expansion system. For instance, a 10% reduction in charge would result in 11.5% reduction in the *SEER* for the system with capillary tube. However, the same condition would lead to no change in the *SEER* for the short-tube orifice expansion system.

One of the major contribution of this study was the investigation of a choosing a best void fraction model. The system capacity, refrigerant flow rate, superheat, and subcooling temperatures of a unit with capillary tube expansion were compared with the experimental results for each void fraction at all charging conditions. The Hughmark void fraction model predicted the system parameters closest to the measured results among the void fraction models. Therefore, the Hughmark void fraction model was used

in the model to compare the simulated with the measured system performance variables.

RECOMMENDATIONS

The central air conditioner and heat pump test procedures adopted in 1979 called for seasonal rating which would account for the cyclic losses during the part load operation of the conditioning units. The definition of the seasonal rating based on several variables, one of which was the C_D. This coefficient is a measure of the efficiency loss due to on/off cyclic of the system. The test procedures prescribed two options for estimating the C_D: (i) from the cyclic dry coil test (D test) or (ii) assuming 0.25 for C_D. In reality, as evident from the present study, the C_D was not constant in the case of the capillary tube expansion system. However, for the TXV and short-tube orifice expansion systems, C_D varied little with charge, but it was measured much lower than 0.25 prescribed by the test procedures. The lack of simulating the transient response (Test D) by the ORNL model was the reason for choosing the prescribed 0.25 for C_D to evaluate the simulated *SEER*. Therefore, a detailed simulation of the transient characteristics is recommended. Such an analysis and simulation may lead to an evaluation of C_D.

The ORNL model predicts the refrigerant flow rate based on the difference between the actual and static superheats for the system with a TXV. If the actual superheat is lower than static superheat, the TXV model would block the refrigerant flow rate. This condition occurred during the refrigerant mass inventory iterating loop in the air conditioner simulation. The measured superheat was used to evaluate the TXV rated capacity. This problem was encountered when the refrigerant charge inventory was requested. It is recommended that a logic be developed which could be used to adjust the simulated and static superheats for more accurate estimation of refrigerant flow rate regulated by the TXV model.

One surprising result from short-tube orifice study is the small variation of EER

and SEER to refrigerant charge. The results from earlier studies on capillary tube suggested that a fixed expansion device would be extremely sensitive to changes in refrigerant charge. This result would seem to have important implications for the service technician in the field and the manufacturers. It is recommended to the manufacturers that short-tube orifice be used instead of capillary tube in the residential air conditioner systems.

An important issue not addressed here is what fraction of units in the field have appreciable leaks or are not charged according to the manufacturer's suggestion. One recommendation would be to study the different charging techniques used in the field and evaluate how effective each is in establishing an acceptable charge. Another related recommendation would be to evaluate the charge on a larger random sample of units in the field. A large enough sample should provide a good indication of how extensive a problem off-design charging is in residential sized units.

The variation of refrigerant quality in the heat exchangers is a function of geometric variables, refrigerant conditions entering the heat exchangers, and the air-side heat transfer. Many investigators have attempted to develop models of the two-phase behavior in the condensers and evaporators. recently, investigators have reported efforts to weigh the refrigerant charge in various individual components under steady state and dynamic conditions. A more detailed experimental study is recommended to evaluate the more accurate void fraction model.

Finally, the model developed to simulate the performance of air conditioners and heat pumps needs several refinements. The recommended refinements include: (i) removing the old ORNL evaporator and condenser models from the present ORNL model to improve computational efficiency, (ii) capability to model transient performance to estimate a more realistic value for C_D and (iii) verification of the model

in the heating mode.

REFERENCES

AMCA/ANSI Standard 210-85, "Laboratory of Testing Fans for Rating," 30 West University Dr., Arlington Heights, IL. 1985.

ASHRAE, ASHRAE Equipment Handbook: HVAC Systems and Applications, Atlanta, Georgia, 1983.

ASHRAE Standard 41.1-74, "Standard Measurement Guide: Section on Temperature Measurements," Atlanta, 1974.

ASHRAE Standard 116-1983, "Methods of Testing Seasonal Efficiency of Unitary Air-Conditioners and Heat Pumps," Atlanta, 1983.

Briggs, D.E., and Young, C.B.B., "Convection Heat Transfer and Pressure Drop of Air Flowing Across Triangular Pitch Banks of Finned Tubes," 5th AICHE/ASME National Heat Transfer Conference, Houston, Texas, 1962.

Carrier, W.H., and Anderson, S.W., "The Resistance to Heat Flow Through Finned Tubing," ASHRAE Transactions, Vol. 50, 1944

Dabiri, A.E., and Rice, C.K., "A Compressor Simulation Method with Corrections for the Level of Suction Gas Superheat," ASHRAE Transactions, vol. 87, Part II, 1981.

Daniels, T.C., and Davies, A., "The Relationship between the Refrigerant Charge and the Performance of a vapor-Compression Refrigeration System," ASHRAE Transactions, Vol. 81, pt. 1, 1975, pp 212-234.

Dhar, M., and Soedel, W., "Transient Analysis of a Vapor Compression Refrigeration System: Part I-the Mathematical Model," XV International Congress of Refrigeration, Venice, Italy, Sep. 1979.

Domanski, P., and Diden, D., "Computer Modeling of the Vapor Compression Cycle with Constant Flow Area Expansion Device," NIST Building Science Series 155, May 1983.

Domingorena, A.A., "Performance Evaluation of a Low-First-Cost Three-Ton Air-to-Air Heat Pump in the Heating Mode," ORNL/CON-18, January, 1980.

Domingorena, A.A., and Ball, S.J., "Performance Evaluation of a Selected Low-First-Cost Three-Ton Air-to-Air Heat Pump in the Heating Mode," ORNL/CON-34, January, 1980.

Fisher, S.K., and Rice, C.K., "A Steady-State Computer Design Model for Air-to-air Heat Pumps," ORNL/CON-80/R1, August 1983.

Flower, J.E., "Analytical Modeling of Heat Pump Units as a Design Aid and for Performance Prediction," Lawrence Livermore Laboratory Report, UCRL-52618, 1978.

Hiller, C.C., and Glicksman, L.R., "Improving Heat Pump Performance via Compressor Capacity Control-Analysis and Tests," Vols. I and II, MIT Energy Laboratory Report No. MIT-EL 76-001, 1976

Houcek, J., and Thedford, M., "A Research Into a New Method of refrigeration Charging and the Effects of Improper Charging," Proceedings of the First Annual Symposium on Efficient Utilization of Energy in Residential and Commercial Buildings, Texas A & M University, August 14-15, 1984.

Lockhart, R.W., and Martinelli, R.C., "Proposed Correlation data for isothermal two-phase two-component flow in pipes," Chemical Engineering Progress, Vol. 45, No. 1, 1949, pp. 39-48.

Karsounes, G.T., and Erth, R.A., "Computer Calculation of the Thermodynamic Properties of Refrigerants 12, 22, and 502," ASHRAE Transactions, Vol. 77, Part II, 1971.

Kusuda, T., "NBSLD, the Computer Program for Heating and Cooling Loads in Buildings," NBS Building Science Series 69, July 1976.

McQuiston, F.C., "Correlation of Heat, Mass, and Momentum Transport Coefficients for Plate-Fin-Tube Heat Transfer Surfaces with Staggered Tubes," ASHRAE Transactions, Vol. 84, Part I, 1978.

Mei, V.C., "Short-Tube Refrigerant Flow Restrictors," ASHRAE Transactions, Vol. 88, Part 2, 1982.

Neal, L., and Conlin, F., "Residential Air Conditioning Field Performance Status and Future Priorities," Proceedings of the ACEEE Summer Study on Energy Efficiency in Buildings, American Council For an Energy-Efficient Economy, Washington, D.C., 1988.

NIST Model: (NBS BUILDING SCIENCE SERIES 155), "Computer Modeling of the Vapor Compression Cycle with Constant Flow Area Expansion Device," U.S. Department of Commerce, National Bureau of Standards, Washington DC, May 1983.

O'Neal, D.L., Boecker, C.L., Murphy, W.E., and Notman, J.R., "An Analysis of Efficiency Improvements in Residential Sized Heat Pumps," ESL/85-24, May 1986.

ORNL Model: (ORNL/CON-80), "A Steady-State Computer Design Model for Air-To-Air Heat Pumps," Energy Division, ORNL, Oak Ridge, TN, December 1981.

Penson, S.B., "Development of a Room Air Conditioner Design Model," Master Thesis, Texas A&M University, Feb. 1988.

Pierre, B., "Flow Resistance with Boiling Refrigerants," ASHRAE Transactions, Sep. Vol. 70, 1964. pp 58-77.

Rice, C.K., "The Effect of Void Fraction Correlation and Heat Flux Assumption on Refrigerant Charge Inventory Prediction," ASHRAE Transactions, Vol. 93, pt. 1, 1987, pp 341-367.

Stoecker, W.F., and Smith,III L.D., and Emde, B.N., "Influence of the Expansion Device on the Seasonal Energy Requirements of a Residential Air Conditioner," ASHRAE Transactions, Vol. 87, pt. 1, 1981, pp 349-360.

Tandon, T.N., Varma, H.K., and Gupta, C. P., "A Void Fraction Model for Annular Two-phase Flow," International Journal of Heat and Mass Transfer, Vol. 28, 1985, pp 191-198.

Thom, J.R.S., "Prediction off Pressure Drop During Forced Circulation Boiling of Water," International Journal of Heat and Mass Transfer, Vol. 7, pp. 709-724.

Trane Co., "Cooling Performance Testing on a Common Eight Year Old Residential Air Conditioning Unit," LaCross, WI, May 24, 1976.

Travis, D.P., and Rohensow, W.M., "The Influence of Return Bends on Downstream Pressure Drop and Condensation Heat Transfer in Tubes," Heat Transfer Laboratory, Massachusetts Institute of Technology, Cambridge, Massachusetts, 1971.

Wallis, G.B., One-Dimensional Two-Phase Flow, McGraw-Hill, New York, 1969.

APPENDIX A

HEAT PUMP SYSTEM PARAMETERS

ORNL Model Inputs

Accumulator Data

Height of accumulator	= 15	in.
Internal diameter of accumulator	= 5	in.

Flow Control Device Data

Rated capacity of the TXV	= 3	tons
Static superheat setting for the TXV	= 6	F
TXV superheat setting at rating conditions	= 11	F
Max. effective operating superheat	= 18	F
TXV bypass or bleed factor	= 1.15	
Capillary tube flow factor	= 4.3	
Number of capillary tube in paralliel	= 1	
Diameter of the short-tube orifice	= 0.071	in.

General Compressor Data

Internal void space volume of compressor	= 2000	$in.^3$
Total specified compressor piston displacement	= 3.486	$in.^3$
Compressor operating frequency	= 60	Hz
Synchronous compressor motor speed	= 3600	rpm
Rated compressor motor speed	= 3450	rpm
Compressor shell heat loss rate	= 0	Btu/h
Bas compressor displacement for compressor map	= 3.486	$in.^3$

Indoor Unit Data

Operating indoor blower frequency	= 60	Hz

Nominal air flow rate	= 1100	cfm
Frontal area of the FLAT coil	= 3.33	$ft.^2$
Frontal area of the A-SHAPE coil	= 3.75	$ft.^2$
Number of refrigerant tube rows in the direction of the air flow (FLAT)	= 4	
Number of refrigerant tube rows in the direction of the air flow (A-SHAPE)	= 3	
Number of equivalent, parallel refrigerant circuits in the heat exchanger (FLAT)	= 4	
Number of equivalent, parallel refrigerant circuits in the heat exchanger (A-SHAPE)	= 6	
Spacing of the refrigerant tubes in the direction of the air flow	= 0.75	in.
Spacing of the refrigerant tube passes perpendicular to the direction of air flow	= 1.0	in.
Total number of return bends (FLAT coil)	= 120	
Total number of return bends (A-SHAPE coil)	= 108	
Fin pitch (FLAT coil)	= 12	fins/in
Fin pitch (A-SHAPE coil)	= 13	fins/in
Fin thickness (FLAT coil)	= 0.0048	in.
Fin thickness (A-SHAPE coil)	= 0.0048	in.
Outside diameter of the refrigerant tubes	= 0.375	in.
Inside diameter of the refrigerant tubes	= 0.347	in.
Thermal conductivity of the fins	= 125.3	Btu/hr-F-ft
Thermal conductivity of the tubes	= 225	Btu/hr-F-ft

Outdoor Unit Data

Operating outdoor blower frequency	= 60	Hz
Nominal air flow rate	= 2700	cfm
Frontal area of the coil	= 20.94	$ft.^2$

Number of refrigerant tube rows in the direction of the air flow	= 1	
Number of equivalent, parallel refrigerant circuits in the heat exchanger	= 5	
Spacing of the refrigerant tubes in the direction of the air flow	= 1.0	in.
Spacing of the refrigerant tube passes perpendicular to the direction of air flow	= 1.0	in.
Total number of return bends	= 0	
Fin pitch	= 20	fins/in
Fin thickness	= 0.006	in.
Outside diameter of the refrigerant tubes	= 0.375	in.
Inside diameter of the refrigerant tubes	= 0.317	in.
Thermal conductivity of the fins	= 125.3	Btu/hr-F-ft
Thermal conductivity of the tubes	= 225	Btu/hr-F-ft

APPENDIX B

UNCERTAINTY ANALYSIS

Capacity of the test air conditioner was calculated during steady state tests using the enthalpy change of air flowing across the indoor coil and the flow rate of that air. An uncertainty analysis for a representative capacity calculation is given in the following paragraphs. The uncertainty analysis provided a measure of the maximum uncertainty expected in the calculated value of capacity. Data used in the analysis was taken from scan data collected during a full charge steady state wet coil test. Run-time values used in the calculation of instantaneous capacity were:

DB Temperature of air entering indoor coil ($T_{DB,i}$)	80.0°F
DB Temperature of air exiting the indoor coil ($T_{DB,o}$)	58.0°F
Flow chamber pressure drop (ΔP)	1.15 in H_2o
DB Temperature of air entering indoor coil ($T_{DB,i}$)	60.0°F
DB Temperature of air exiting the indoor coil ($T_{DB,o}$)	55.4°F

These data values were used as inputs to a psychrometric property and nozzle flow rate program to obtain the followings calculated values:

Air flow rate (Q)	1134.5 ft^3/min
Entering air enthalpy (h_i)	31.4 *Btu/lbma*
Exiting air enthalpy (h_o)	24.1 *Btu/lbma*
Specific volume of air (v)	13.82 $ft^3/lbma$

Air side capacity is calculated from the following equation:

$$AC = \frac{60 \cdot Q \cdot (h_o - h_i)}{12000 \cdot v} \qquad \text{(B.1)}$$

where:

AC = air-side capacity (tons)

The air-side capacity for the sample data was 2.996 tons.

The data taken from a given scan during air conditioner testing constituted a single sample measure. The method of Kline and McClinktock may be used to estimate the uncertainty in a value such as instantaneous air-side capacity calculated from single sample experimental data. According to the method, the uncertainty in the calculated value of a quantity, R, which is a function of n independent variables, $x_1, x_2, \ldots x_n$, is given by:

$$\omega_R = \left[\left(\frac{\partial R}{\partial x_1} \omega_{x_1} \right)^2 + \left(\frac{\partial R}{\partial x_2} \omega_{x_2} \right)^2 + \cdots + \left(\frac{\partial R}{\partial x_n} \omega_{x_n} \right)^2 \right]^{\frac{1}{2}} \tag{B.2}$$

where:

ω_R = uncertainty in the calculated value of R
ω_{x1} = uncertainty in the value of x_1
ω_{x2} = uncertainty in the value of x_2
.
.
.
ω_{xn} = uncertainty in the value of x_n

Therefore, if the uncertainties in the variables $x_1, x_2, \ldots x_n$, are known, than the uncertainty in the calculated value of R can be obtained. Equation B.2 can be used with Equation B.1 to write an expression for the per-unit uncertainty in air-side capacity. This expression is of the form:

$$\frac{\omega_{AC}}{AC} = \left[\left(\frac{\omega_Q}{Q} \right)^2 + \left(\frac{\omega_{h_i}}{h_o - h_i} \right)^2 + \left(\frac{\omega_{h_o}}{h_o - h_i} \right)^2 + \left(\frac{\omega_v}{v} \right)^2 \right]^{\frac{1}{2}} \tag{B.3}$$

where:

ω_{AC} = uncertainty in calculated capacity
ω_Q = uncertainty in air flow rate
ω_{hi} = uncertainty in entering air enthalpy
ω_{ho} = uncertainty in exiting air enthalpy
ω_v = uncertainty in specific volume of air

Now, the problem is reduced to one of finding uncertainties in Q, h_i, h_o, and v. Air flow rate, Q, is measured in a nozzle flow chamber which meets ANSI/ASHRAE 51-1985 (ANSI/AMC 210-85) Standard specifications. Following recommendations of this standard, the per-unit uncertainty in air flow rate is found to be 1.4% of the calculated flow rate value.

As previously stated, the values of enthalpy and air specific volume were obtained with a computer program which utilized curve fits of psychrometric data in addition to the ideal gas laws. The computer routines were set up in a series of data reduction steps to calculate the required values given dry bulb and dew point temperatures. Thus, the Kline and McClintock equation can be used to find the uncertainties in h_i, h_o, and v. The uncertainties in the input data are taken to be half the smallest scale division of the measurement instruments and have the following values:

$\omega_{DBT} = 0.05^{\circ}F$
$\omega_{DPT} = 0.05^{\circ}F$

Because of the complexity of the steps used to calculate h_i, h_o, and v from the input data, the partial derivatives required in the uncertainty calculation are difficult to obtain. However, a procedure suggested by Holman may be used to find the necessary partial derivatives. This procedure numerically approximates the derivative dependence of a value computed by several complicated data reduction steps on the input values

required by those steps. Using this procedure for h_i, h_o, and v, the following uncertainties were found:

$$\omega h_i = 0.30 \ Btu/lbma$$
$$\omega h_o = 0.31 \ Btu/lbma$$
$$\omega v = 0.028 \ ft^3/lbma$$

These uncertainties are corrected by 0.7% to account for uncertainty associated with the ideal gas approximation. This 0.7% uncertainty is additively combined with each of those listed above to obtain:

$$\omega h_i = 0.37 \ Btu/lbma$$
$$\omega h_o = 0.38 \ Btu/lbma$$
$$\omega v = 0.10 \ ft^3/lbma$$

These uncertainties, along with that of the air flow rate (1.4% of 1134 cfm) can be used in Equation B.3 to obtain the uncertainty in calculated air-side capacity of 10 percent, or:

$$AC = 2.99 \text{ +/- } 0.3 \ tons$$

The calculated uncertainty in air-side capacity represents the maximum amount by which the capacity could be expected to be in error. Instantaneous cooling capacity calculated from refrigerant-side data at the indoor coil was 3.12 tons. Ideally, the air and refrigerant-side capacities should math (energy balance). The discrepancy of 4.35% between these capacities is within ASHRAE test standard requirements and suggests a smaller probable error than 10% obtained in the uncertainty analysis. All the experimental test data values retained were observed to have a discrepancy between calculated air and refrigerant-side capacities of less than 6%.

VITA

Mr. Mohsen Farzad was born on January 06, 1956 in Ahwaz, Khozestan, Iran to Abdol-Kareem and Fatemeh Farzad. Mr. Mohsen Farzad graduated from Kareem Fatemi's High School in 1974 then joined the Iranian armed forces to serve his country. Having served in the army for two years, he traveled to the U.S. for higher education. Mr. Farzad enrolled at a private English school in Los Angeles, CA. studying English for nearly one year. In spring of 1978, he enrolled at Blinn College then transferred to Texas A&M university in the fall of 1980. Mr. Mohsen Farzad received two B.S. degrees in Electrical and Mechanical Engineering at Texas A&M University in December, 1982 and December of 1984, respectively. He enrolled at Texas A&M University in spring of 1985 for the Master of Science program in Mechanical Engineering. He graduated with a Master of Science in December of 1986. He then joined the Doctoral program in spring of 1987 in Mechanical Engineering. His area of specialization was thermal science and energy management. Mr. Mohsen Farzad permanent address is, 367 Ghafari and Khaghoni St., Ahwaz, Iran.